NTNU
Norwegian University of
Science and Technology

Spectroscopic Ellipsometry of MoO_{3-x}

Magnus Langøien
Waalekalv

Master of Science in Physics and Mathematics
Submission date: June 2016
Supervisor: Turid Worren Reenaas, IFY
Co-supervisor: Morten Kildemo, IFY
Thomas Brakstad, IFY

Norwegian University of Science and Technology
Department of Physics

Preface

This master thesis (TFY4900) is the end of the Master in Science in Physics and Mathematics at Norwegian University of Science and Technology (NTNU). It was written during the winter and spring, 2016. The experimental work during the thesis was performed at the Department of Physics.

I would like to thank my supervisor Turid Worren Reenaas for giving me an interesting and relevant project for my master thesis. I would also like to thank her for answering my questions during the meetings, including me in her research group and for valuable inputs and comments during the thesis. I also want to thank my co-supervisors Thomas Brakstad and Morten Kildemo for their help with learning me the use of the spectroscopic ellipsometer and for the help they gave me when I had questions about the modeling of the dielectric function. I also would like to thank Mohammadreza Nematollahi and Katherine Inzani for supplying the samples and for answering the questions that I had about the samples. At last, all of my friends deserves a thanks for all the fun time we had during our master work and my family for supporting me through the studies.

Trondheim, June 2016

Magnus Langøien Waalekalv

Abstract

Intermediate band solar cells (IBSC) has a great potential to increase the efficiency of solar cells and reduce the costs of the generated electricity. To realize IBSC that contain one or more sub-band gap in the main band gap of the semiconductor needs to be developed. In this master thesis, non-destructive spectroscopic ellipsometry (SE) measurements are used to determine the dielectric function (DF) of the samples. The measurements are performed on different series of reduced molybdenum oxides, MoO_{3-x}, thin films. The samples had been fabricated by either pulsed laser deposition (PLD) or spin coating (SC) before the thesis work started.

To determine the DF, an optical model for the samples had to be developed. A model developed previously for another potential IB material (chromium doped ZnS) was used as a staring point, but turned out not to be suitable for the MoO_{3-x} samples. Initially, information about the thickness and roughness was used to develop the model, and later also information about composition and resistivity, available for some of the samples, was used. Information from cross-sectional scanning electron microscopy and atomic force microscopy images were used to develop the layer structure of the model.

For the PLD samples, the final model consisted of three layers and it was assumed to consist of the same material, but with varying amount of void, on top of a substrate. The bottom layer had no void, the uppermost layer (surface roughness) had 50 % void, and in the middle layer the amount of void was used as a fitting parameter between 0 and 50 %. The SC samples were more dense than the PLD samples, and thus the middle layer was not included. A single oscillator layer was developed for the material in both the PLD and SC samples. This oscillator layer accounts for contributions from band to band transitions across the band gap, as well as sub-band gap transitions caused by intermediate, or sub-stoichiometric, phases of MoO_{3-x} and contributions from free electron excitations.

The final model was used to obtain the DF for most of the samples, but not for the PLD samples grown at the highest temperatures: for these samples it is likely that the three layers consist of different material, and thus the developed model, assuming the same material in each layer, failed. For the low growth temperature series from PLD and the SC samples, reasonable dielectric functions were obtained, that matched the information about the samples obtained from other characterization techniques, and also matched DFs reported for MoO_{3-x} found in literature. Using the finale model, fitted values for the band gap and other material properties could be obtained. Based on this, we can conclude that the low growth temperature series from PLD consist of mainly MoO_3 for the the films made with high oxygen partial pressure in the vacuum chamber during deposition, with very little sub-band gap absorption, meaning that intermediate band states are most likely not present in these samples. In contrast, the low growth temperature series deposited with a low oxygen partial pressure, consist of MoO_2 (i.e. highly reduced MoO_3), but also of intermediate phases such as Mo_4O_{11}, leading to significant sub-band gap absorption.

The samples made by SC had been annealed in a hydrogen atmosphere to form oxygen vacancies, because it was known from literature that this could result in an intermediate band. From the fitted values of the band gap and the other parameters we could confirm earlier findings that for the thickest films, only the highest annealing temperatures lead

to formation of significant amounts of sub-band gap states. In contrast, for the thinnest films, that also were found to consist of MoO_3, an increasing amount of sub-band gap absorption was seen with increasing annealing temperature. The sub-band gap absorption was related to intermediate phases (for instance Mo_4O_{11}) and MoO_2 for the highest annealing temperature.

Suggestions for further development of the model are also included in this thesis work, as well as a discussion on what deposition technique seems to be more suitable to make an IB material based on MoO_{3-x}.

Sammendrag

Mellombånd solceller (IBSC) har et stort potensiale for å øke effektiviteten til solceller og redusere kostnadene på den genererte elektrisiteten. For å kunne realisere IBSC må halvledere som består av sub-båndgap utvikles. I denne masteroppgaven er spektroskopisk ellipsometri brukt til å finne dielektrisk funksjonen (DF) til prøvene. Målingene er utført på forskjellige serier av tynne filmer bestående av redusert molybden oksid, MoO_{3-x}. Prøvene var allerede fabrikkert, enten med pulset laser deponering (PLD) eller våt kjemisk deponering (SC), da masteroppgaven ble påbegynt.

For å finne DFen, måtte en optisk modell for prøvene bli utviklet. En modell utviklet for et annet mulig mellombånd materiale (kromdopet ZnS) ble brukt som et utgangspunkt, men det ble tidlig slått fast at denne modellen ikke passet for tynne filmer av MoO_{3-x}. I begynnelsen var tykkelsene og ruhetene til prøvene eneste informasjonen som ble brukt, for utvikling av modellen. Senere ble også annen informasjon om innhold og resistivitet, som var tilgjengelig for noen prøver, brukt. Informasjon fra sveipeelektronmikroskop (SEM) og atomkraftmikroskop (AFM) ble brukt til å utvikle strukturen til de forskjellige lagene i modellen.

For PLD prøvene, bestod den ferdige modellen av tre lag, og det ble antatt at lagene bestod av samme materiale, men med varierende mengder tomrom, på toppen av substratet. Bunnlaget hadde ikke noe tomrom, øverste laget (overflate ruheten) hadde 50 % tomrom, og i det midterste laget var mengden tomrom en av parameterne som kunne tilpasses til en verdi mellom 0 % og 50 %. Siden SC prøvene var mere tettpakket enn PLD prøvene, ble det midterste laget droppet for SC prøvene. Et eget oscillatorlag ble utviklet og ble brukt på både PLD og SC prøvene. Oscillatorlaget beskriver bidragene fra bånd til bånd overgangene over hele båndgapet og sub-båndgap overgangene på grunn av mellomfaser av MoO_{3-x} og frie elektroner eksitasjoner.

Den ferdige modellen ble brukt til å finne DFen for de fleste av prøvene, men ikke for PLD prøvene grodd ved høye temperaturer: for disse prøvene er det mest sannsynlig at de tre lagene består av forskjellige materialer, og dermed vil den utviklede modellen, som antar at det er samme materiale i alle lagene, feile. For PLD prøvene grodd ved lave temperaturer og SC prøvene ble DFen funnet som var i god overenstemmelse med informasjon om prøvene fra andre karakteristikk teknikker, og som var i god overensstemmelse med DF for MoO_{3-x} funnet i litteraturen. Ved å bruke modellen, kunne verdier for båndgapet og andre material egenskaper bli funnet. Basert på disse kunne vi konkludere med at PLD prøver grodd ved lave temperaturer består hovedsakelig av MoO_3 for de prøvene laget ved høye oksygen trykk i vakuumkammeret i løpet av deponeringen, med veldig lite sub-båndgap absorbsjon, som betyr at mellombånd tilstander er mest sannsynlig ikke til stede i disse prøvene. I kontrast, PLD prøver deponert ved lave oksygen trykk består av MoO_2 (veldig redusert MoO_3), men også av mellomfaser, som Mo_4O_{11}. Dette fører til signifikant sub-båndgap absorbsjon.

Prøver laget med SC hadde blitt varmet opp i en hydrogen atmosfære for å lage oksygen vakanser, siden det var kjent fra litteraturen at dette kunne resultere i mellombånd. Fra de tilpassede verdiene av båndgapet og de andre parameterne kunne vi bekrefte tidligere funn for de tykkeste prøvene at bare de prøvene som hadde blitt varmet med høyest temperatur førte til signifikant sub-båndgap tilstander. I kontrast, for de tynnere filmene,

som også ble funnet til å bestå av MoO_3, en økende mengde av sub-båndgap absorbsjon ble observert ved økende temperatur i prosessen. Sub-båndgap absorbsjonen var relatert til mellomfasene av molybden oksidene (for eksempel Mo_4O_{11}) og MoO_2 for de høyeste temperaturene.

Forslag for videre utvikling av modellen er også inkludert i masteroppgaven, i tillegg til diskusjon om hvilke deponeringsteknikker som ser ut til å være mere egnet for å lage mellombånd materialer basert på MoO_{3-x}.

Contents

List of Figures

List of Tables

Chapter 1

Introduction

1.1 Background

The consumption of energy has increased significantly over the last decades, but in 2014 the growth was 0.9 %, which is the slowest rate of growth since 1998, except for the decline after the financial crisis in 2008 [1]. A graph over the the world primary energy consumption year for year since 1998 to 2014 in million tonnes of oil equivalent (mtoe) is shown in Figure 1.1. As seen from the figure, the main consumption comes from energy resources such as oil, coal and natural gas ($\approx$ 85 %), while only 2.5 % of the consumption comes from renewables (geothermal, solar, biomass and waste). A huge growth in the renewable sector is necessary to lower the pollutant energy consumption of oil and coal, which are limited on short time scale. Therefore, in the last years renewable energy sources have been investigated in a large scale, including solar energy.

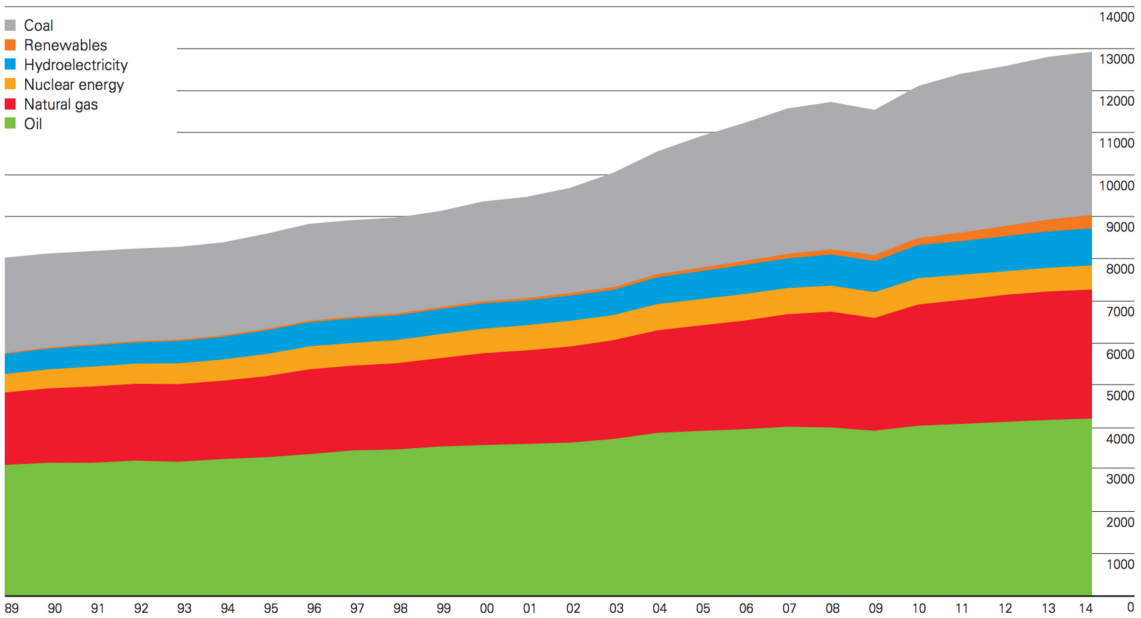

Figure 1.1: Graph overview of the world primary energy consumption year for year since 1998 to 2014 in million tonnes of oil equivalent (mtoe). The growth in 2014 was 0.9 %, which is the slowest rate of growth since 1998, except for the decline after the financial crisis in 2008. Taken from Ref. [1].

Solar energy has a huge potential to meet the energy demand. Figure 1.2 illustrates the annual incident solar radiation to the earth, with boxes of each of the available energy resources inside, including the annual energy consumption in 2011. The available solar energy is much larger than the global annual energy consumption in 2011. In 2014, 40 GW solar cell capacity power was installed globally which resulted in a total of 178 GW of solar power installed in the world. The prices of the solar cells have declined about 75 % the last ten years [2]. The three top countries in the market are China, Japan and USA, while in Europe Italy, Germany and Greece are the leading countries in utilizing solar cells. It is expected that the solar power market in Europe could grow by 80 % by 2019 [2], i.e. the market is growing quickly. On a world basis, the number could be over 200 GW more installed over the next three years, depending on the political will to invest in green energy and solar cells [2, 3].

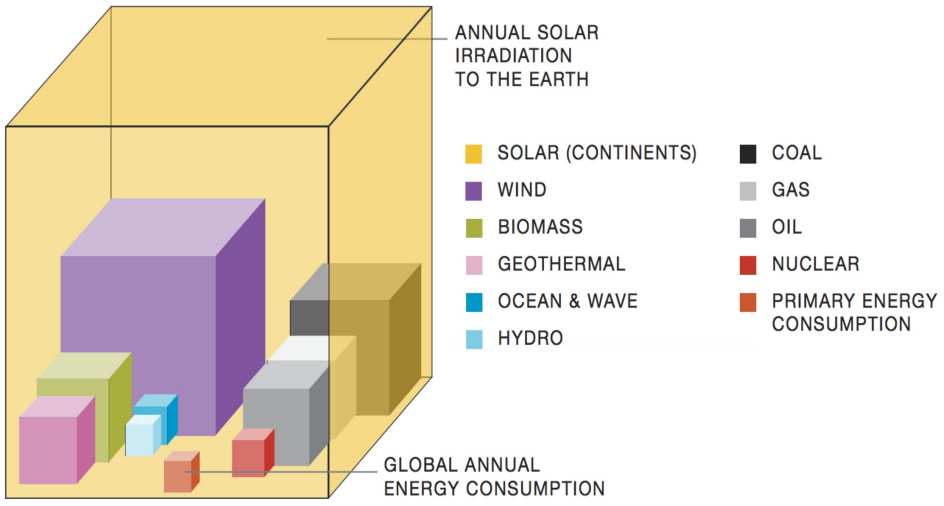

Figure 1.2: Annual solar irradiation to the Earth, with boxes of the available energy resources, including the global annual energy consumption in 2011. Taken from Ref. [3].

There are two common methods to generate electric power. The first method was discovered by Michael Faraday in 1821 and required a relative movement of a magnetic field and a conductor. The second method use the photovoltaic generation by using solar cells, also called photovoltaics cells. The latter method was demonstrated first in 1954 by Chapin, Fuller and Pearson [4] with a doped silicon semiconductor with an efficiency of 6 %. A solar cell utilizes the incident solar radiation and converts photovoltage into electricity when an electron is excited from the valence band to the conduction band due to absorption of the radiation. The process occurs normally in semiconductors under illumination from a light source. An advantage with use of solar cells is the possibility to use them everywhere from the rooftops on cabins in the mountains to satellites in space. The electricity is produced close to the consumer and hence lower the costs for energy transportation. One disadvantage for solar cells are their rather low efficiency. One of the largest losses is due to the energies in the radiation are too small to excite an electron from the valence band to the conduction band. Figure 1.3 shows the sun spectrum at the top of the atmosphere (yellow), radiation at sea level (red) and a blackbody spectrum at 5250 °C (black). Due to absorption bands in greenhouse gases, the spectrum is reduced at the sea level compared to the top of the atmosphere.

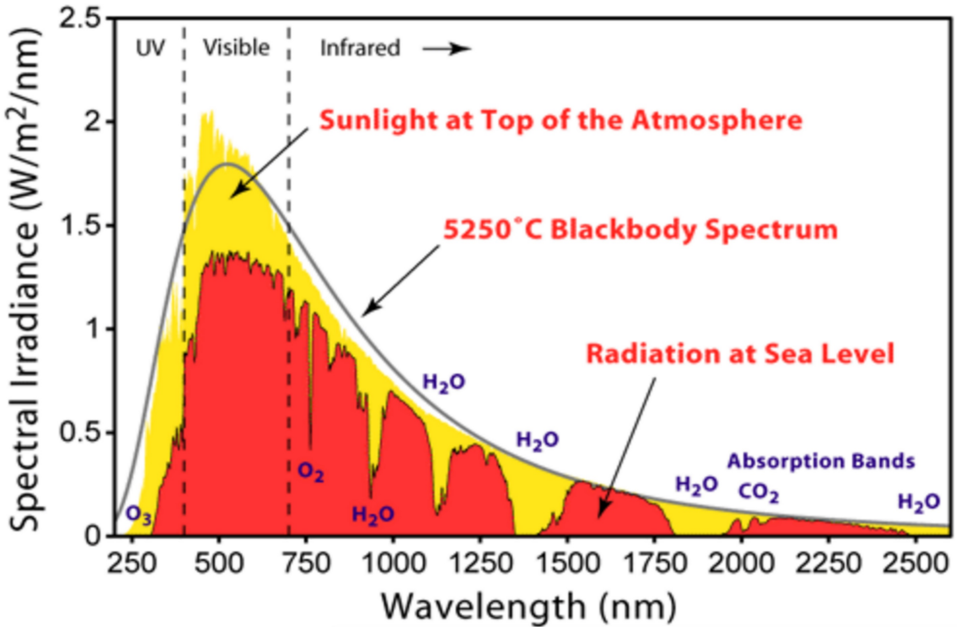

Figure 1.3: The sun spectrum at top of the atmosphere (yellow), radiation at sea level (red) and a blackbody spectrum at 5250 °C (black). Taken from Ref. [5].

The important thing for solar energy to be a leading energy source is to reduce costs in the production process and increase the overall efficiency to convert the incident radiation to electricity. Silicon (Si) wafers is the most common material for solar cells with a band gap energy $E_g = 1.1$ eV, which corresponds to wavelengths of approximately 1100 nm. Such cell is normally 100 cm^2 in area and produces a DC photovoltage between 0.5 - 1 V. To obtain higher voltage, multiple solar cells are connected in series and constitutes a module producing 15 V [6]. As one can see from Figure 1.3 of the sun's spectrum, much of the photon energy in the sun spectrum is too low to excite the electrons, or too large which creates heat and reduces the band gap energy. As a result the efficiency will decrease. The record for a single junction of crystalline Si-wafer solar cell is 25.6 ± 0.6 % [7] under illumination from the global AM1.5 spectrum (1000W/m^2). The efficiency is restricted by physical principles and to increase the overall efficiency, new methods and designs needs to be developed. As a result, the absorption from the sun spectrum will increase and the efficiency may be up to 70% depending on the construction and number of layers and band gaps. Different methods have been suggested where one method is to capture the electron which is excited high up in the conduction band before thermalization. Another method is to create multiple carrier pair per incident photon or create one carrier pair with use of multiple photons. The last method is to make solar cells with more than one band gap, either by stacking multiple materials above each other (tandem cells), or using materials with an intermediate band [8]. The record for a multiple band gap module is 38.8 ± 1.2 % [7]. All these methods have the same objective; to increase the overall efficiency of the cell, and at the same time to have as low production costs as possible. To develop new materials that possible have an intermediate band, optical properties of the new materials needs to be studied. In this thesis, materials to increase the number of band gaps are studied for realization for the so called intermediate band solar cells.

1.2 Objective

This master thesis is motivated by an earlier master thesis written by Benjamin Roaldssønn Hope [9] in 2015. He used spectroscopic ellipsometry data to model the dielectric function for ZnS and chromium doped ZnS, ZnS:Cr. He used the dielectric function to evaluate whether it is a useful material for intermediate band solar cells. In this thesis, another potential intermediate band material is studied: reduced molybdenum oxide, MoO_{3-x}. MoO_3 is an interesting material that are used in several applications such as smart windows and display devices [10, 11]. The first objective is to learn about intermediate band solar cells, spectroscopic ellipsometry measurements and data analysis of the experimental data. The next objective is to use the data obtained from the measurements to model the dielectric function for different samples of reduced MoO_{3-x}. It is important to note that the samples have been made by Katherine Inzani and Mohammadreza Nematollahi by two different techniques: wet chemistry (spin coating) and pulsed laser depostion. The fabrication processes of the samples were not a part of this thesis. One another objective is to see how the optical properties changes with fabrication method and with variations in the fabrication details and parameters. The final objective of the thesis is to evaluate whether MoO_{3-x} is a promising intermediate band material and to suggest further work.

1.3 Structure of the Thesis

The thesis is structured in chapters where basic solar cell physics is presented first in Chapter 2. Intermediate band solar cells and the state of art are presented briefly in Chapter 3. In Chapter 4, the experimental methods and details are presented together with sample preparation details and other information from experiments performed elsewhere. Chapter 5 will present the dielectric function (DF) and the different types of oscillators to model the DF are presented. In Chapter 6, the results are presented and discussed before the thesis is completed with a conclusion and suggestions for further work in Chapter 7.

Chapter 2

Solar Cells

In this chapter, basic solar cell physics is presented, which includes the basic principles, the p-n junction and the depletion zone, diffusion length and recombination, $I-V$ characteristic of the solar cells and loss mechanisms. Thereafter, the solar cell generations are presented with emphasis on the third generation solar cells and the intermediate band solar cells (IBSC). The theory is found in Refs. [6], [12] and [13] if not another is specified.

2.1 Basic Solar Cell Physics

2.1.1 Basic Principle of a Solar Cell

Solar cells converts energy from radiation into electrical energy by absorbing photons from the solar irradiance. A typically solar cell consists of a semiconductor material with different doping, shown in Figure 2.1. The n-type materials have an excess of conduction electrons, while the p-type materials have an absence of free electrons. In the latter case, the absence of electrons are called holes. In addition, metal contacts are made at the front and back to allow the electrons to be extracted through an circuit with a load. An antireflecting layer is placed at the top of the semiconductor to minimize the reflections.

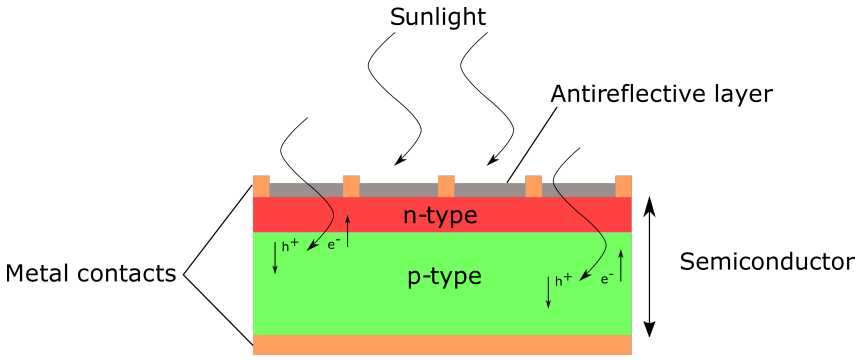

Figure 2.1: A schematic illustration of a typically solar cell where electron-hole pairs are created by sunlight.

The energy E of a photon incident to a solar cell can be determined by

$$E = \frac{hc}{\lambda} = h\nu, \tag{2.1.1}$$

where h is the Planck's constant, c is the speed of light in vacuum, λ is the wavelength and ν is the frequency of the photon. As the material absorbs the radiation from the sun, an electron-hole pair is created if the photon energy is large enough, i.e. $E \geq E_g$ where E_g is the band gap of the material used in the solar cell. The electron is excited up to the conduction band (CB) while the hole is exited in the valence band (VB). This is illustrated in Figure 2.2 (a). After the excitation of an electron from the VB to the CB, the electron-hole pair can recombine. If the recombination takes place, a photon with energy equal E_g is emitted as Figure 2.2 (b) shows. To prevent this from happening, the p-n junction is introduced.

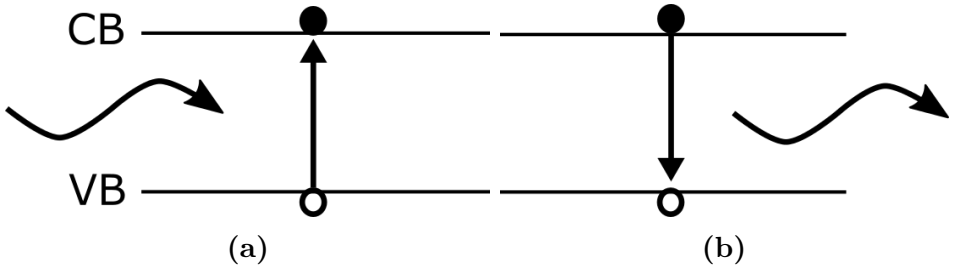

Figure 2.2: (a) Illustrates an absorption of a photon with energy $E \geq E_g$ and creates an electron-hole pair where the electron is excited to the conduction band. (b) Illustrates how a photon is sent out when the electron-hole pairs recombine in the valence band when the electron de-excite back to the valence band.

2.1.2 The p-n Junction and the Depletion Zone

When a n-type and a p-type material is placed side by side, electrons from the n-type material diffuse over to the p-type material and holes diffuses over to the n-type material as Figure 2.3 (a) illustrates. As a result, an internal electrical field due to the fixed space charge of the materials on each side of the junction. This balance the diffusive forces that arises from the different concentrations of free electrons and holes. During this process, the Fermi level is constant.

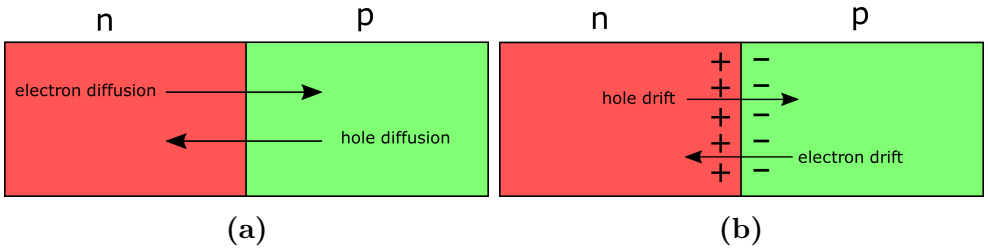

Figure 2.3: (a) Illustrates how electrons from the n-type material diffuse over to the p-type material and holes diffuse over to the n-type material. (b) Illustrates how the internal electric field in the depletion zone affect the drifting of holes and electrons in the junction.

The p-n junction represents the depletion zone, or region, where the electron-hole pairs are created when the solar radiation are absorbed. Due to the internal electric field in the zone, the hole will drift towards the p-type and the electrons towards the n-type as Figure 2.3 (b) shows. A voltage drop builds up between the sides of the semiconductor that can be used to extract power through an external circuit with a load. It is important to note that absorption process occurs in the whole semiconductor depending on photon energies and absorption coefficient, but only the electron-holes pair close to the p-n junction are affected by the internal field.

2.1.3 Diffusion Length and Recombination

After a relaxation time τ, the electron-hole pairs will recombines after moving a diffusion length L. In a typically doped material, the relaxation time is in the range 10^{-2} to 10^{-8} seconds and combining this with the diffusion constant D, the diffusion length is given by $L = (D\tau)^{1/2}$. The length is typically much larger than the width of the junction. As a result, electron-hole pairs created outside of the depletion zone could drift to the opposite side of the semiconductor and build up a voltage.

The recombination can take place in three different ways shown in Figure 2.4 [12]. Number one is the Shockley-Read-Hall (SRH) recombination where the process is due to defects and impurities in the semiconductor. It is a two-step process where the first step is an electron which is trapped in the band gap, and the second step is that a hole is trapped in the same level. A property of the result is that the electron-hole recombines and the recombination rate depends strongly of the localized energy levels. For instance, a level close to the mid band gap will increase the recombination significantly compared to a level near either the VB or CB.

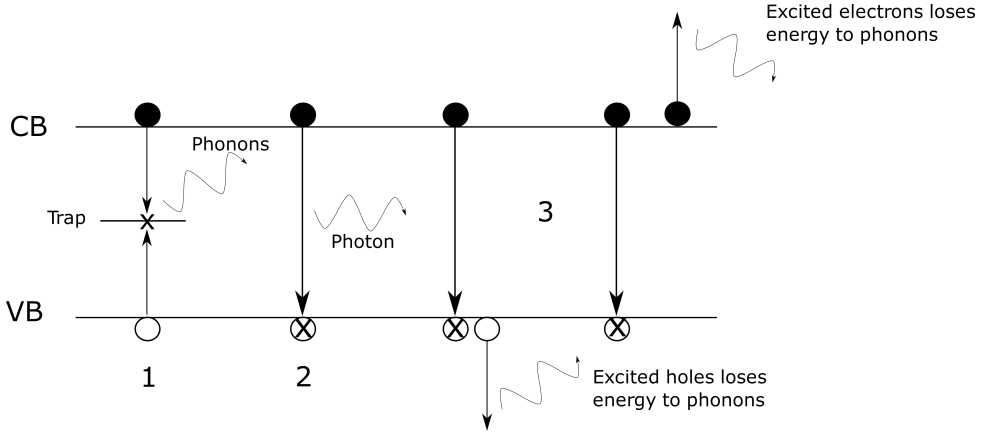

Figure 2.4: Illustrates the three recombination that takes place in a solar cell: 1) Shockley-Read-Hall (SRH). 2) Radiative recombination. 3) Auger recombination. Figure adapted from Ref. [12] with modification in Inkscape.

The second type of recombination is the radiative recombination. This is the most dominant recombination process of all three in direct band gap semiconductors. The process involves that an electron in the CB de-excite back to the VB and release a photon with same energy as the difference between the initial and final state, typically close to the band gap energy. In semiconductors with indirect band gap, an additional phonon is

required and the lifetime is longer for the electron-hole pair, i.e. other recombination processes are more likely to occur.

The third recombination is the Auger recombination and involves three carriers. The point here is that an electron-hole pair recombines, but instead of sending out a photon, the energy is given to a third carrier. The third carrier can either be an electron in the CB or a hole in the VB and receive the energy as kinetic energy which rapidly thermalize and the energy releases as phonons. All recombination processes may take place at the same time.

2.1.4 Current-Voltage Characteristic of Solar Cells

To understand the Current-Voltage ($I - V$) characteristic of the solar cells, it requires a couple of definitions. The first definition is the open circuit voltage V_{oc} which is the voltage when the terminals are isolated from each other. This can be seen as a load with infinite resistance. The short circuit current I_{sc} is the current when the terminals are connected together. For an intermediate load with resistance R_L, the solar cell develops a voltage drop between zero and V_{oc} with the current I such that $V = IR_L$. It is possible to connect a battery to a solar cell while it is in the dark and two cases arises. The first is the forward bias where the positive conventional circuit, i.e. opposite to electron current direction, passes from the p-type to the n-type and increase the current. This reduces the band potential difference V_B, as Figure 2.5 (b) illustrates. Comparing with the isolated junction with zero bias in Figure 2.5 (a), it is seen V_B'' is smaller than V_B. The second case is the reverse bias case where the battery opposes the internal potential difference and the current is reduced as Figure 2.5 (c) illustrates. V_B' is here larger than V_B.

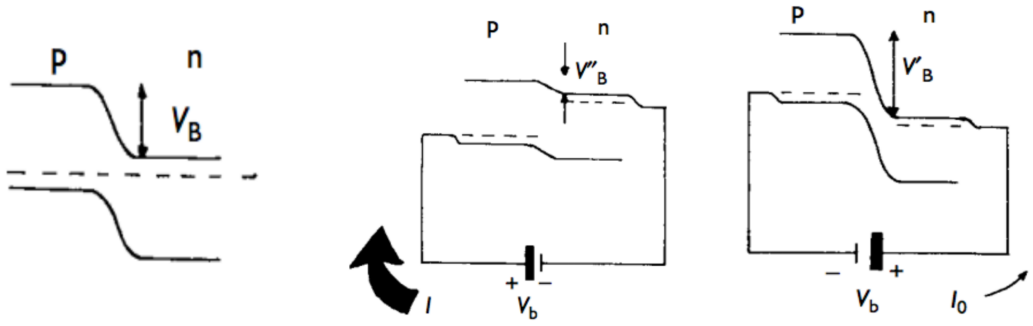

Figure 2.5: (a) Isolated junction with zero bias. (b) Forward bias where $V_B'' < V_B$. (c) Reverse bias where $V_B' > V_B$. Figure is taken from Ref. [6].

When a solar cell is not illuminated by a light source, it behaves like a diode with the respective $I - V$ characterization with the forward and reverse bias as described above. When there is no illumination, the recombination and generated current is equal while no external bias is connected. If a load is connected between the two terminals, a voltage drop is introduced and the potential generates a current. The net current reduces from the I_{sc} value and is called dark current with an analogy to the dark current $I_D(V)$ for diodes, where an applied voltage, or bias, is connected to the device in the dark. An equivalent circuit of an ideal solar cell is shown in Figure 2.6 where the dark current is

given by the Shockley equation stated as

$$I_D(V) = I_0 \left[\exp\left(\frac{qV}{k_B T}\right) - 1 \right], \tag{2.1.2}$$

where I_0 is the saturation current under full reverse bias before an avalanche breakdown and is a constant for each material, q is the electron charge, k_B is the Boltzmann's constant, V is an applied bias in the dark and T is the temperature.

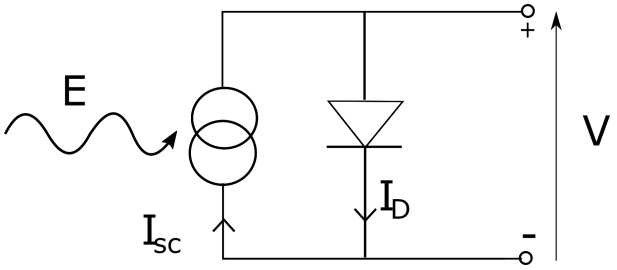

Figure 2.6: Illustrates an ideal solar cell, where photon with energy E is illuminated at the cell.

While a light source illuminates the solar cell, the light creates a photocurrent I_L and the over all current is the sum of I_L and I_D as

$$I = I_L - I_D = I_L - I_0 \left[\exp\left(\frac{qV}{k_B T}\right) - 1 \right], \tag{2.1.3}$$

where the negative sign is due to the opposite flow of the two currents. Per definition, I_{sc} is the current when an applied bias is zero. As a result, $I = I_{\text{sc}} = I_L$ in equation (2.1.3) leading to

$$I(V) = I_{\text{sc}} - I_D(V) = I_{\text{sc}} - I_0 \left[\exp\left(\frac{qV}{k_B T}\right) - 1 \right]. \tag{2.1.4}$$

The power from a solar cell is $P = IV$, where the voltage V is in the range from 0 to V_{oc}. The maximum of the power P occurs at a voltage V_{m} with a current I_{m}. Hence, the fill factor FF is defined as

$$FF = \frac{I_{\text{m}} V_{\text{m}}}{I_{\text{sc}} V_{\text{oc}}}, \tag{2.1.5}$$

which describes the squareness of the $I - V$ curve, i.e. if FF is close to 1, it will give a squareness of the $I - V$ curve. The efficiency of a solar cell is given by

$$\eta = \frac{I_{\text{m}} V_{\text{m}}}{P_{\text{s}}} = \frac{I_{\text{sc}} V_{\text{oc}} FF}{P_{\text{s}}}, \tag{2.1.6}$$

where the numerator is the power delivered at operating point and the denominator is the power incident from the light. FF, I_{sc}, V_{oc} and η are important quantities when discussing the performance of the solar cells.

In a real solar cell, there are leakage currents around the sides and resistance in the contacts, resulting in loss of power. These losses can be seen as a resistance in series and a resistance in parallel. An equivalent circuit for this case is shown in Figure 2.7. The series resistance R_s is the result from resistance in the material to current flow, and the parallel, or shunt resistance R_{sh}, is a result from the leakage around the edges of the solar cell. This will reduce the FF and reduce the overall efficiency of the solar cell. To obtain

the best efficiency, R_{sh} needs to be maximized and R_s minimized. Taken into account these resistances, the diode equation becomes

$$I = I_L - I_0 \left(\exp\left(\frac{q(V + IR_s)}{kT} \right) - 1 \right) - \frac{V + IR_s}{R_{\text{sh}}}. \tag{2.1.7}$$

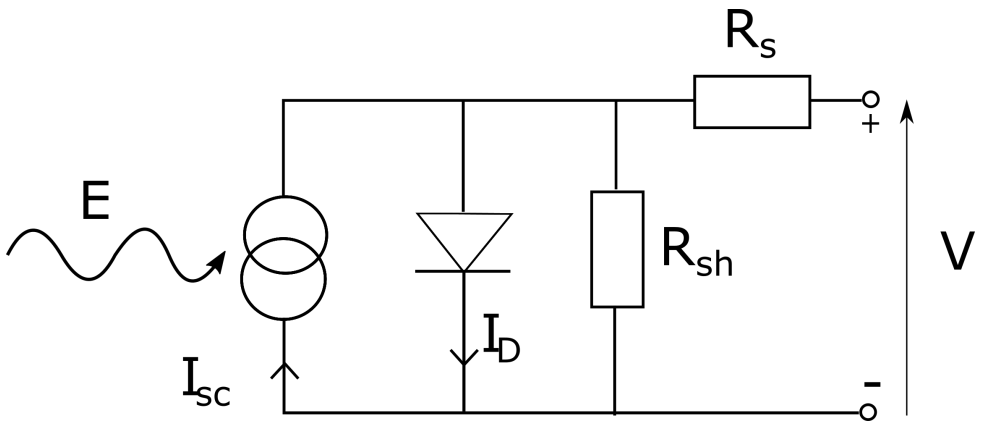

Figure 2.7: Equivalent circuit for a real solar cell with a series resistance R_s and a shunt resistance R_{sh}. The current is described by equation (2.1.7).

The ideal diode behavior of the solar cell is seldom seen, and it is common that the dark current depends more weakly on the bias. Instead the ideality factor m is introduced, which quantify the dependence on the applied voltage, or bias, V. Hence, the $I - V$ characteristic is given by the non-ideal diode equation

$$I = I_{\text{sc}} - I_0 \left[\exp\left(\frac{qV}{mkT} \right) - 1 \right], \tag{2.1.8}$$

where m typically is in the range between 1 and 2.

2.1.5 Loss Mechanisms

The largest losses can be seen in Figure 2.8 there 1) are the losses of energy from below the band gap. 2) High energy photons that excites the electron high up in the CB followed by a relaxation given as phonons, or lattice thermalization. 3) and 4) from junction and contact voltage losses, respectively. 5) Recombination losses. All losses with an approximate amount in percentages may be found in Table 2.1 [6] for a silicon solar cell. The remaining amount is the power delivered by the cell. The total amount is the total incident irradiance to the solar cell. As seen, photon energy less than band gap ($\approx 23\%$), excess photon energy ($\approx 33\%$) and voltage factor ($\approx 20\%$) is by far the largest losses. Photon energy less than the band gap, i.e. $h\nu < E_g$, is lost since there is not enough energy to excite the electron to the conduction band. The excess losses are given by $h\nu - E_g$ and appears as heat in the cells and can be seen as the energy larger than E_g. The remaining percentages is the power delivered by the cell.

Table 2.1: Overview of typically losses in a solar cell given in percentages [6] of the total amount of incident irradiance. The percentage of each loss is an approximation and the remaining percentages is the power delivered by the cell.

Type of loss	Percentages
Excess photon energy	33 %
Photon energy less than E_g	23 %
Voltage factor	20 %
Additional curve factor	5 %
Curve factor	4 %
Surface contact obstruction	3 %
Reflection top surface	1 %

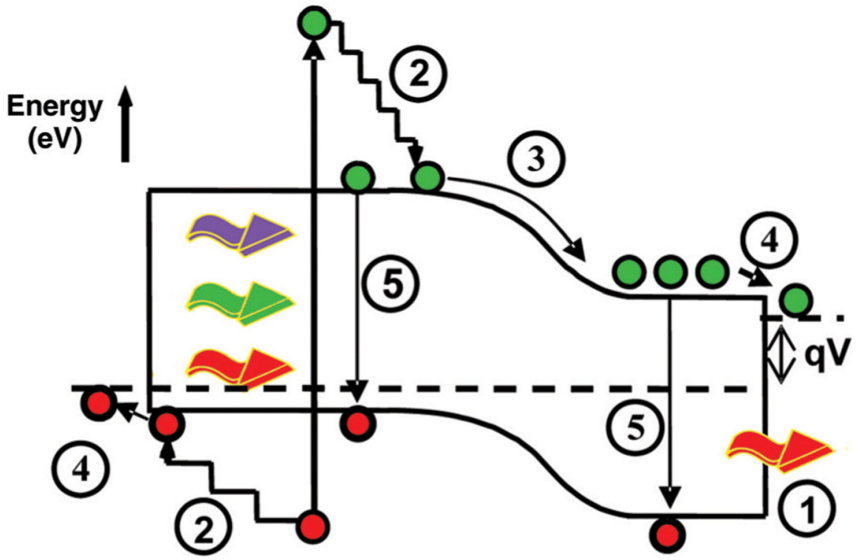

Figure 2.8: Illustrates the largest losses in a solar cell. 1) The losses of energy from below the band gap. 2) High energy photons that rise the electron high up in the CB followed by a relaxation given as phonons, or lattice thermalization. 3) and 4) Junction and contact voltage losses. 5) Recombination losses as described above. Figure is taken from Ref. [8]

2.2 Solar Cell Generations

Solar cells can be divided into three generations as Figure 2.9 [8] shows. In the figure, the efficiency is a function of the cost of production in US dollar per m^2, where the green ellipse correspond to the first generation, yellow to the second generation and the red to third generation. The first generation is wafer based on medium efficiency and high production costs. The second generation is based on thin-films that is cheaper to produce at an even lower efficiency. Third generation solar cells are now under development to increase the efficiency above the single band gap limit. In the following subsections, each generation is described in more detail.

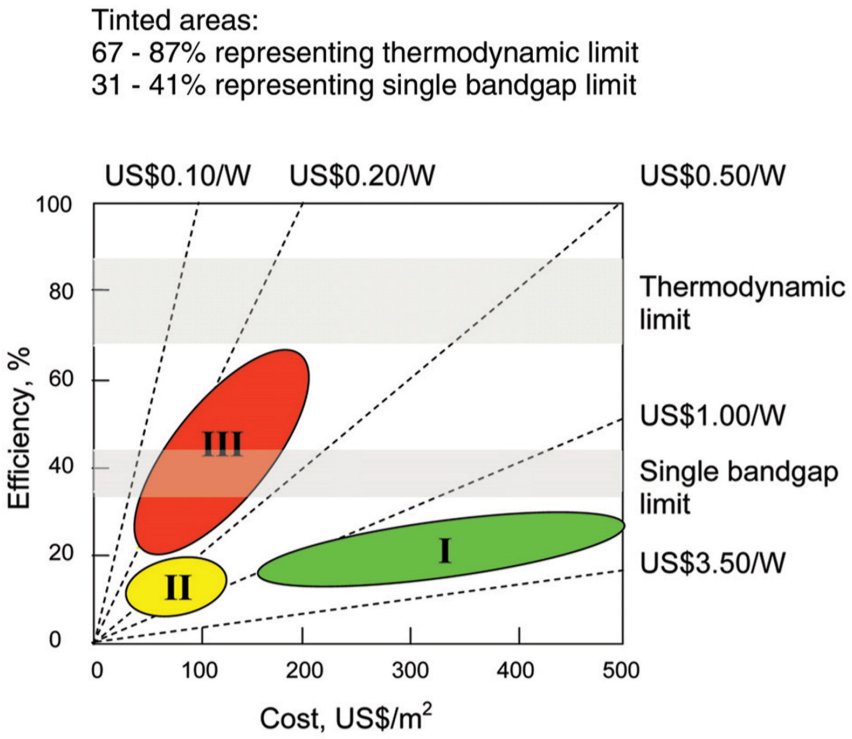

Figure 2.9: Graph over the efficiency and the cost projection for the different solar cell generations. Green (I) is first generation wafer based, yellow (II) is the second generation thin films and the red (III) is the third generation advanced thin films photovoltic technologies. The grey areas is the thermodynamic limit for third generation and the single band gap limit, typically 67-87 % and 31-41 %, respectively. Figure is taken from Ref. [8].

2.2.1 First Generation

The first generation solar cells are wafer-based, i.e. a thin slice of a semiconductor material, typically Si-wafers. Si-single crystal were used in the beginning, but due to high costs and sophisticated technology there was a change to multicrystalline Si wafers instead [14], nevertheless Si single crystals are still in use. These types of cells are today produced and are available on the marked with an efficiency between 12-16 % in 2013, depending on the manufacturing process and wafer quality [14]. The efficiency is significantly lower than the one Shockley and Queisser [15] found in 1960. In their work, a theoretical limit for the efficiency of the p-n junction was found to be 30 % for an $E_g = 1.1$ eV under one sun. The most common material is Si-wafers, where the efficiency can be found in Table 2.2 [7] under 1 sun with an AM1.5 spectrum (1000 W/m^2) for crystalline and multicrystalline solar cells. As seen in the table the crystalline solar cell is very close to Shockley-Queisser limit under one sun.

2.2.2 Second Generation

The second generation cells are based on thin film technology. In contrast to the first generation solar cells, thin film solar cells provides cost reduction in the production due to materials savings, low temperature processes integrated cell insulation and high automation level in series production [14]. Typically materials used in second generation

Table 2.2: Records for Si solar cells solar cells under one sun with an AM1.5 spectrum (1000 W/m^2) [7]. Crystalline and multicrystalline are first generation solar cells, while amorphous Si solar cells are second generation.

Type	Efficiency (%)
Crystalline	25.6 ± 0.5
Multicrystalline	21.25 ± 0.4
Amorphous	10.2 ± 0.3

solar cells are In, Ga and Te [16]. A problem with the second generation solar cells is the use of toxicity of elements in the materials like Cd. Therefore, alternative materials semiconductor compounds $Cu_2ZnSn(S_xSe_{1-x})_4$, Cu_2ZnSnS_4, $Cu_2ZnSnSe_4$ and In_2S_3 are investigated which all are Cd free and non-toxic. For copper indium gallium selenide (CIGS) the efficiency record has now reached 21.0 ± 0.6 and for CdTe the efficiency is 21.0 ± 0.4 [7]. Amorphous Si-wafers are also a second generation solar cell, with the record given in Table 2.2. As seen, the records for CIGS and CdTe are not far away from the Si-wafers crystalline record.

2.2.3 Third Generation

For the third generation solar cells, the efficiency limit is the thermodynamic limit for the third generation solar cells as shown in Figure 2.9 between 67 - 87 %. As presented earlier, two of the most important loss mechanisms in the solar cells are the photons with energy less than the band gap energy and thermalization loss exceeding the band gap energy. Different ways to solve the problem have been proposed: a) increasing the number of band gaps; b) multiple carrier pair generation per high energy photon or single carrier pair with multiple low energy photons; and c) capturing carriers before thermalization [8]. In the following, some concepts based on these alternatives will be presented.

Tandem Cells

The tandem cell is the easiest configuration to understand and is belonging to increasing the number of band gaps. A schematic drawing for how a tandem cell looks like is shown in Figure 2.10 [8]. The point here is to stack different p-n junction with different band gap top of each other, with the highest band gap at the top. The result is that the high energy photons are absorbed first, while the low energy photons pass through to smaller band gap materials. There are different ways how these cells can be connected together. However, one obtains the largest power when one independently optimizes each p-n junction. If the components are not separated, it is difficult to obtain this arrangement which requires independent electrical contacts to each junction and are difficult to produce. Therefore, the normal way is to connect the cells directly in series.

Increasing the number of band gaps in tandem cells, increases the overall efficiency of the cell. In the case of an infinite number of band gaps the efficiency under one sun is 69 %. Under full concentration the efficiency approaches the thermodynamic limit on 86 % [17]. Tandem cells are today very expensive to produce and therefore mainly used in space where the high efficiency is crucial [8, 13]. The efficiency record for a five junction

cell is 38.8 ± 1.2 %, while for an InGa/GaAs/InGaAs the efficiency is 37.9 ± 1.2 % [7]. These efficienies are indeed larger than the single band gap solar cells, but still far away from the thermodynamic limit for third generation solar cells.

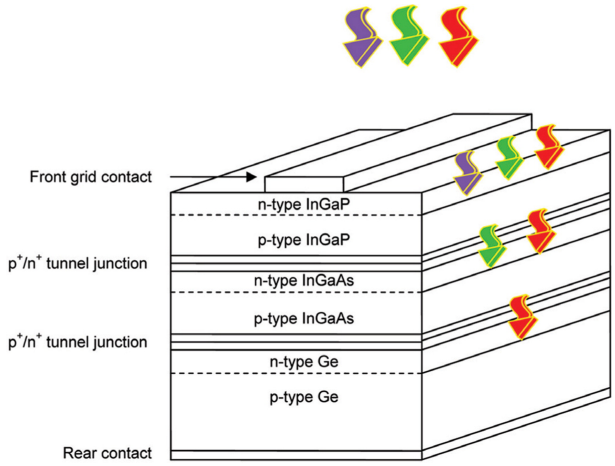

Figure 2.10: A schematic drawing of a tandem solar cell with three cells, where the band gap from each layer decreases from the front to the back. Figure is taken from Ref. [8].

Hot Carriers

An approach to increase the efficiency of the solar cell is to use the excess kinetic energy of the photogenerated carriers before they relax. The basic concept is to slow the rate of carrier cooling for the photoexcited carriers so they can be collected at higher energies ("hot"), and results in higher voltage [8]. It is a simple design compared to tandem cells. As a result, the excess photon energy loss mechanism is reduced. The challenge for such type of solar cells is to extract the carriers at these "hot" states before thermalization. To extract the carriers, selective energy contacts, which accepts only very narrow energy ranges, must be used. Such type of solar cells have a theoretical efficiency limit of 65 % for unconcentrated illumination, but still a lot of work have to be done before they are realized [8].

Multiple Electron-hole Pairs/Impact Ionization

Another idea is to use the high-energy photon (at least twice the band gap energy) to create additional electron-hole pairs, instead of giving up their excess energy as heat [18]. Evidence for this creation has been shown in Ref. [19]. In that work, it was shown that ultraviolet radiation can generate hot carriers with sufficient energy to cause impact ionization. This results in two electron hole pairs per incident photon and hence increases the overall efficiency. The efficiency of such type of cell is calculated to be 85.9 % for a cell of band gap approaching zero. The problem with this type is that there is a small probability for a impact ionization to occur in bulk materials, but recently it is shown that this process is more efficient in quantum dots [8]. Quantum dots based solar cells will be presented later.

Intermediate Band Solar Cells

The intermediate band solar cells (IBSC) was first introduced by Luque and Marti [20]. The concept is that there is an intermediate band (IB) between the VB and CB. This approach is related to increasing the number of band gaps. Photons with less energy than the band gap are absorbed in parallel with photons with higher energy than the E_g for the material. A schematic figure is shown in Figure 2.11. As one can see with the IB, there are three band gaps; The normal band gap energy E_g (3), and to and from the IB results in two new energy gaps labeled E_h (2) and E_l (1), where h indicate the highest energy and l indicates the lowest energy.

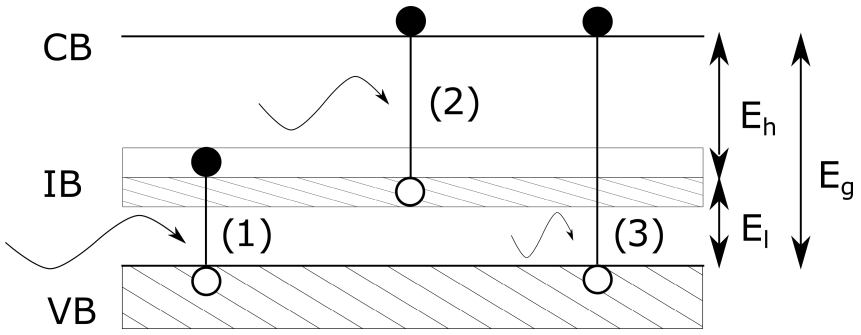

Figure 2.11: Illustrates the energy gaps in an IBSC, where two new energy gaps E_h and E_l are introduced due to the intermediate band. Taken from Ref. [21]

The IB needs to be partial filled to achieve the highest possible value for the photocurrent [21]. This maximize the absorption in transition one and two in the figure. The filling may take place by three different methods: 1) naturally of the IB material exhibits a metallic band; 2) dope the material if the IB materials naturally presents a filled or empty band to depopulate or populate the IB material; 3) use light concentration to photofill the IB material. To reduce the thermalization losses to a minimum, the absorption coefficient are assumed to not overlap for the three transmission in an ideal IBSC. This will cause the transition with largest possible energy from the incident photon to occur.

By introducing the IB material, the overall efficiency of the solar cell increases above the Shockley-Queisser limit of 40.7 % [22] under maximum concentration. Such type of a solar cell has the same limiting efficiency level as the three-layer tandem cells; 63 % under maximum concentration and 48 % under one sun. An IBSC is characterized by an empty band, fully filled band and a partially filled IB [23]. Therefore, the Fermi level needs to be placed in the IB. As a result, photons can both be excited from VB to IB, and from IB to CB in parallel [23]. IBSCs could be realized in several ways as nanostructures such as quantum dots, highly mismatched alloys (HMAs) and semiconductor bulk material containing a high density of deep level impurities (DLIs) [21]. These concepts will be presented in the next chapter.

Figure 2.12 shows a modified version of Figure 2.1 where an IB material has been introduced (turquoise).

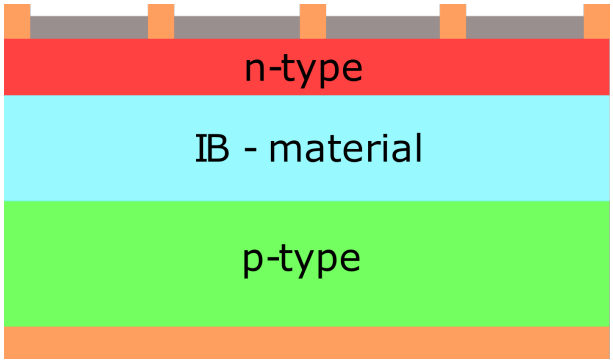

Figure 2.12: Modified version of Figure 2.1 where the IB material has been inserted between the n-type and p-type with metallic contacts and an antireflecting layer (grey).

Chapter 3

Intermediate Band Solar Cells - Realization and the State of Art

In this chapter different experimental techniques used to characterize IBSCs are presented. Thereafter, the sections about the possible realizations and the state of art will be presented briefly.

3.1 Experimental Techniques used to verify IBSC Operation

Eight different techniques are used to characterize IBSCs and IB material, as described in the review by Ramiro. et. al. [21]: sub-band gap spectral response (SR), or quantum efficiency (QE), two-photon sub-band gap photocurrent, increase in short-circuit current under white light illumination, voltage preservation, electroluminescence (EL), sub-band gap absorption, photoluminsescence (PL) and photoreflectance (PR). The first five techniques are applied to IBSC, while the last three are applied to IB-materials. In addition in this review, the characterization of the devices, both IBSCs and IB materials, has led to demonstration of two operational principle of IBSC. The first principle is the production of photocurrent while the IBSC absorbs photons with lower energy than the band gap energy. The second principle is the preservation of the output voltage while the absorption happens. Since it will be a lot to compare all eight techniques for all types of IBSCs, I will in the following sections only update on the SR, or QE, voltage preservation and PL measurements for different materials.

3.2 Quantum Dots

One possibility to create an IBSC is to use quantum dots (QD) and the concept was introduced in 2000 by Marti et. al. [24]. It is one of the most studied candidate materials for implementing the IBSC [21]. This was the first approach for the realization for an IBSC. QDs are nanoparticles that are embedded in matrix materials with a higher band gap [22]. The intermediate band (IB) will here arise from the confined states of the electrons in the conduction band 3-dimensional potential wells which are originated from the conduction band offset between the dot and barrier material. The most used material is In(Ga)As/GaAs, where In(Ga)As (X) is the QD material and GaAs (Y) is the material of the matrix with the notation X/Y. The band gap distribution in this material is not optimal for an IBSC realization, but it is a material that is well-known and hence the best candidate to test the concepts. Other materials such as InAs/AlGaAs, GaAs/AlGaAs and GaSb/GaAs have been investigated, in addition.

The state of art in 2014, reported in [21], SR, or QE, was reported by numerous of groups for In(Ga)As/GaAs, but in general the sub-band gap response was weak. This can be explained by the low QD density and limited numbers of QD layers. In measurements of the voltage preservation indicated that the V_{OC} is lower than the reference cell. The reference cell is a single band gap semiconductor with no IB materials inserted for comparison. One would expect some voltage loss in an ideal IBSC under concentrated light, but the experiments shows that the voltage loss was higher than the expected, possible due to non-radiative recombination. It is shown that QD materials have a lower effective band gap than the reference cell, for instance GaAs, due to a wetting layer [25]. In a PL measurement one would expect three distinct luminescent peaks for an IB material. So far, only relaxation from IB to the VB is reported in InAs/GaAs and InAs/AlGaAs systems, but no luminescence has been reported from CB to IB yet. Efficiencies of such modules are in the range from 7 % to 8.6 % in 2014 [26, 27].

3.3 Highly Mismatched Alloys

Another possible way to create an IBSC is to use highly mismatched alloys which are semiconductor alloys where band anticrossing effects takes place. The effect was first shown by Shan et. al. in Ref. [28]. These effects arises as a small amount of an element of high electronegativity produces a strong modification of the properties of the semiconductor. The CB may splits into two sub-bands which may lead to the formation of a band separated from the CB [29]. As a result, an IB is formed. The "mismatch" refers to different atom size, ionicity, and electronegativity in the elements that are combined. This model has predicted several new effects as the donor activation efficiency in $In_yGa_{1-y}As_{1-x}N_x$ alloys and the change in the nature of the fundamental band gap from indirect to direct in $GaP_{1-x}N_x$ [30]. The modification of the CB is the result of the anticrossing effect in the interaction between highly localized states of the introduced element and the extended states of the host material. It is also shown that the VB can exhibit anticrossing effects [31]. Typically materials investigated for this use are ZnTe:O and Ga(P,Sb)As:N with notation X:Y, where X is the main alloy and Y is the element introduced in small quantities and represents the anticrossing band effect. Adding such elements may invoke large challenges due to phase segregation and introduction of strains

in the material [32].

The state of art in 2014 [21] is that sub-band gap production QE has been reported for ZnTe:O and Ga(P,Sb)As:N IBSC prototypes. QE is not close to unity since the structure of such IBSCs are not been optimized. In unblocked devices, i.e. without a layer in the IBSC blocking charge transport in the IB, the QE in most cases is greater than 0.1 for energies higher than E_h. This indicates that the absorption coefficient for VB to IB is high enough for use in photovolatics applications [21]. For voltage preservation, no evidence for such phenomena is documented yet. In all cases, V_{OC} values have been smaller than E_h, as a consequence of disconnection between the CB and IB. A comparison with a reference cell indicated a voltage loss in the IBSC prototype, as for the QD-IBSC above. In PL measurements, there has been reported for an IB to VB radiative recombination for ZnTe:O and GaPAs:N, but no evidence for CB to IB yet for these type of materials.

3.4 Bulk Materials With Deep-Level Impurities

Bulk materials with deep-level impurities (DLI) is today the least investigated IBSCs [21]. The reason is the difficulty of production of such materials due to the requirement of high density of impurities. The high density of impurities degrades the electronic transport properties and the quality of the host material. In the beginning, fabrication of DLI materials with IB seemed impossible, but today it is possible to produce deep levels in semiconductors that may produce an IB. The IB material is inserted between the n-type and p-type in the normal solar cell, as showed in Figure 2.12. As described above, mid gap traps acts as an effective non-radiative recombination center. Luque et. al. [33] presented in 2006 arguments that suggested sufficiently high densities of traps, by introducing deep energy levels, suppressed the non-radiative recombination. As a result, this could indicate a good IB material that could be used as solar cells. Typically materials are ZnS:Cr, GaAs:Ti, GaN:Mn, $CuGaS_2$:Fe and $CuInS_2$:Sn [21], where X is the bulk material and Y is the DLI in the notation X:Y.

For this type of materials there has been reported two sub-band gaps in addition to the main band gap energy in GaN:Mn in a SR measurement. This measurement was not under short-circuit conditions, but with a bias of -2 V. Similarily to QDs IBSC, the sub-band gap response was found to be weak. In voltage preservation measurements, there are few results that compares the V_{OC} with a reference cell, but for $CuGaS_2$:Fe prototypes there has been shown that the voltage losses increase with the Fe content. For PL measurements on $CuInS_2$:Sn it is shown that it was additional IB to VB related emissions compared to undoped $CuInS_2$.

In summary, a lot of investigations has been done on different types of IB materials and IBSCs. The operating principle has been demonstrated, but not in room temperature. As said above, QD-IBSC is the most widely approach in the research to make an IBSC, but other candidates as HMA-IBSC and DLI-IBSC are recently used to verify IB behavior. A lot research has yet to be made before the realization for an IBSC to be available for commercial use.

3.5 IBs Based on Transition Metal Oxides

In the recent years, it has been shown that transition metal oxides could form IBs in semiconductors. Molybdenum oxides, which is the material used in this thesis, are one of the transition metals which has been studied for these properties [34, 35]. To achieve the IB properties of such materials, doping with hydrogen, lithium or sodium, or removing oxygen ions, or both is required. If the electronic structures are not destroyed, oxygen vacancies acts as sub-band gaps below the main band gap. In Vourdas et. al. [34], it is suggested such materials could be aligned with either the VB or CB in semiconductors as electrodes to extract carriers.

Chapter 4

Experimental Methods and Details

In this thesis, molybdenum oxide thin films deposited with two different techniques been studied. The properties of the the films depends strongly on both deposition technique, deposition parameters and a possible post-treatment. In this chapter, different phases of molybdenum oxides will be presented. Next, the two deposition techniques will be presented where deposition properties and details are presented, with some additional information about the samples from other experiments performed elsewhere. The last section is the spectroscopic ellipsometry experiment presented with theory, experimental setup and details and how the data analysis is performed.

4.1 Molybdenum oxides

Molybdenum oxide is a transition metal oxide and is of huge interest due to the broad area of application. It is one of the must studied materials due to its electrochromatic properties. The last decade, there have been a large interest of this phenomenon to create large area devices like smart windows, which control the solar energy flow into a room [10], and display devices [11]. This effect is due to the change of optical properties under the application of an external perturbation [36]. The changes are fast and reversible. Other areas MoO_3 may be used in are ion storage (cathode material in lithium batteries) [37, 38, 39], UV photographs [40], optical disk memories [41], diffusion barriers [42], sensors [43, 44], optical recording [45] and in photovoltaics [46]. In addition, MoO_3 can be used as catalyst for variety of partial oxidations [47]. In this section, the different molybdenum oxide phases, present in the materials in the thesis, will be presented. More detailed information about molybdenum oxides and its phases may be found in Ref. [48].

4.1.1 Molybdenum Trioxide (MoO_3)

MoO_3 is an insulator and optically transparent for low photon energies [49]. In the applications presented above, MoO_3 often appears as thin films. There are many ways to deposit MoO_3 thin films like, magnetron sputtering [50, 51], electron beam deposition [36, 52], chemical vapor depostion (CVD) [53], thermal evaporation [54], thermal oxidation [55], pulsed laser deposition [56] and wet chemical solution deposition [48]. MoO_3 can be

in different crystalline phases. The two most typically are the α and β phase, where α phase is an orthorhombic phase. It has a layered structure consisting of double layers of MoO_6 octahedra. These layers are held together with van der Waal's forces in the (0 1 0) direction, while in (1 0 0) and (0 0 1) direction held together by covalent forces [57]. β phase is a monoclinic phase, with a framework structure [36]. An illustration of α-MoO_3 (a) and β-MoO_3 (b) is shown in Figure 4.1. For α-MoO_3, top is in the *ac*-plane while bottom is in *ab*-plane. In addition, it has been reported that MoO_3 also exists in a hexagonal structure for bulk samples [58]. α-MoO_3 crystallizes with lattice constants a=13.855 Å, b=3.696 Å and c=3.963 Å, while β-MoO_3 crystallizes with lattice constants a=7.122 Å, b=5.366 Å and c=5.566 Å [59].

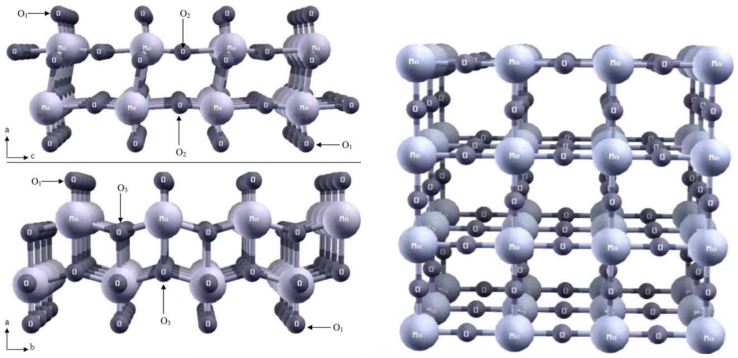

(a) **(b)**

Figure 4.1: (a) The crystall structure of α-MoO_3. The black spheres illustrates oxygen while the blue spheres illustrates molybdenum. Top is in the *ac*-plane while bottom is in *ab*-plane. (b) The crystal structure of β-MoO_3. Figure is taken from Ref. [59].

The band structure of MoO_3 is shown in Figure 4.2 along the high-symmetry points [60]. The valence band maximum is situated at U, while the conduction band minimum is situated at Γ. Since the valence band maximum and conduction band minimum are situated at different points, it is an indirect band gap with a calculated $E_g = 1.95$ eV from density functional calculations. The lowest direct band gap is at Γ with energy 2.76 eV using density functional calculations. It is important to note that with density functional calculations, the lowest gap from the calculations is smaller than the experimentally observed values.

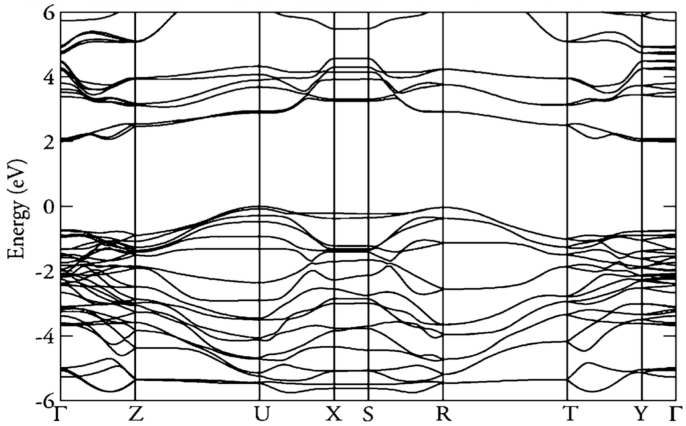

Figure 4.2: The band structure of MoO_3. It is a indirect band gap with $E_g = 1.95$ eV. The lowest direct band gap is at Γ with $E_g = 2.76$ eV. Figure is taken from Ref. [60].

4.1.2 Molybdenum Dioxide (MoO_2)

Another oxidation state of molybdenum oxide is molybdenym dioxide (MoO_2). MoO_2 exhibits a metallic electrical conductivity as it crystallizes in a distorted rutile monoclinic structure [49], as shown in Figure 4.3. Thin films of MoO_2 are of interest due to the possibilities for energy storage [61] and as soft magnetic [62] and optical material [63]. In addition, it is important for selective oxidation catalysis of organic compounds [64, 65]. As for MoO_3, there are different methods to fabricate MoO_2 films. The two most common are hydrothermal synthesis [61, 66] and thermal evaporation [62, 67]. It is also possible to reduce MoO_3 in a hydrogen environment at high temperatures [68].

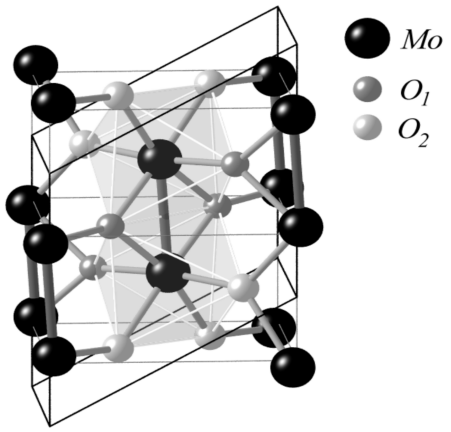

Figure 4.3: Shows the structure of MoO_2, where the black spheres are Mo and the small spheres are oxygen. Figure is taken from Ref. [69].

For amorphous MoO_2, results have shown that the materials are highly absorbing with a direct band to band transition [70]. The band gap energy varies with deposition techniques and lies between 2.38 - 2.83 eV [70, 71, 72]. MoO_2 can also be found in amorphous phase with high absorption coefficient. Therefore, MoO_2 films are a candidate to be electrodes for photovoltaic and photoelectrochemical solar cells. The band structure of MoO_2 is shown in Figure 4.4 where the Fermi level is the dashed line. As one can see, some of the bands cross the Fermi level. These crossings are responsible for the metallic nature of MoO_2 which are observed [60].

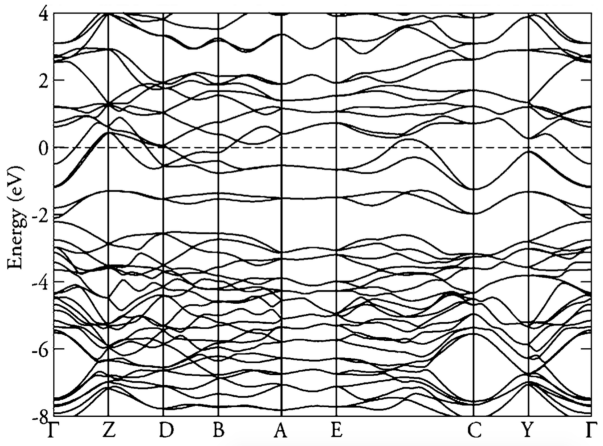

Figure 4.4: The band structure of MoO_2. Figure is taken from Ref. [60].

4.1.3 Intermediate Phases of Molybdenum Oxides, MoO_{3-x}

Since MoO_3 is a transparent material for low photon energies, there is no absorption below the band gap. One can do a post-process with the as-deposited MoO_3 films to make substoichiometric MoO_{3-x} oxides where $0 < x < 1$. When deposited on cold substrates, it often forms in an amorphous phase. Substoichiometric amorphous thin films of MoO_{3-x}, contains a number of oxygen ion vacancies which are positively charged structural defects, capable of capturing one or two electrons. One electron may be ionized thermally while the other can only be ionized optically. Thus, donor centers are formed in the amorphous layers of MoO_3. These donor centers exist in the forbidden gap of the insulator and form a defect band below the conduction band [73]. There are many different Mo oxidation states, such as Mo_4O_{11}, Mo_5O_{14}, Mo_6O_{23} and Mo_9O_{26} [74]. These deficiencies in oxygen controls electrical and the optical constants of the material. In addition, the optical constants and the band gap energy E_g for MoO_{3-x} depends on the method of deposition and processes after the deposition to make MoO_{3-x} oxides. Mo_4O_{11} is the most common of the intermediate phases of MoO_{3-x}, and Porter et. al. [72] showed that Mo_4O_{11} had absorption bands at approximately 1.3 eV, 2.13 eV and 2.42 eV, as shown in Figure 4.5. In this figure, an absorption peak is found for MoO_2 and Mo_9O_{29} at 2.48 eV and 2.12 eV [72], respectively.

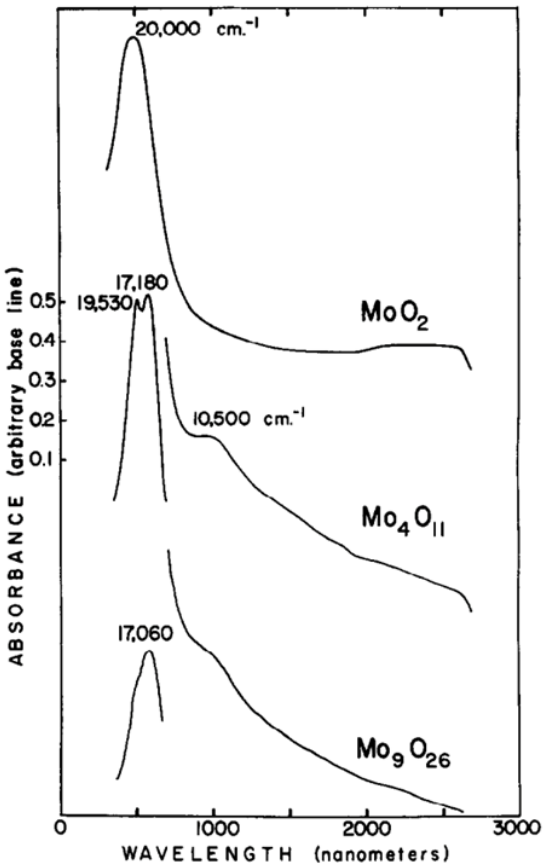

Figure 4.5: Absorption peaks for intermediate phases for molybdenum oxides, where MoO_2 has one at 2.48 eV, Mo_4O_{11} has peaks at 1.3 eV, 2.13 eV and 2.42 eV and Mo_9O_{29} at 2.12 eV. Figure is taken from Ref. [72].

4.2 Pulsed Laser Deposition

4.2.1 About Pulsed Laser Deposition

Pulsed laser deposition (PLD) is briefly presented in this section with basic principles and the experimental setup. The basic principles and setup are taken from Refs. [75, 76, 77].

PLD is today one of the most popular technique for thin films fabrication of multicomponent materials. It is a fast and simple way to deposit thin films on substrate and is very reliable for small-area films. With use of laser light, thin films are fabricated on a substrate due to a reaction between the target material and the laser light. The material is ablated from the target and condense on the substrate surface. Since it is possible to create multicomponent stoichiometric film from a single target, PLD is of huge interest. The most studied materials are high-temperature superconductors, compound semiconductors, dielectrics, ferroelectrics, insulators, polymers and biological materials. PLD is of huge importance in the developments of new materials. An advantage with PLD for research and development of new materials is the short time it takes to fabricate thin films of different compounds and doping.

Since the invention of lasers, use of pulsed lasers as energy source for thin film growth has been explored. The first experiments that used the PLD technique took place in the 1960s, and continued with limited efforts in the 1970s and 1980s. First in late 1980s, this technique become popular as it was possible to grow high quality of high-temperature superconducting films. Several characteristics made PLD more popular than other complex oxide thin-films techniques. The characteristics were to make stoichiometric samples, the simplicity in the experimental setup and the possibility to study arbitrary oxide compounds. In recent years, the PLD has gone from being an academic curiosity to a broad technique for thin-films deposition. PLD is one of the techniques that had a fast and widely way into studies and applicable venues of deposition of thin films of new and different materials.

The essential parts of the setup are the laser, chamber, target and the substrate and an illustration of the experimental setup is shown in Figure 4.6. The main point is that a pulsed laser is focused on to the target material. The target mainly consists of the deposited material and is typically in ceramics, or liquids in special cases. The target could also be in single-crystalline, polycrystalline, powdery or amorphous form. The material is ablated from the target and creates a plasma plume in the forward direction. The plasma will condense at the substrate surface and create a thin film. The ablation takes place in vacuum ,or in an inert, or reactive atmosphere, where the technique is termed reactive laser ablation for the latter case.

In PLD, a background gas is often introduced in the reaction chamber. The first reason is that many thin-films growth requires a reactive species, for instance molecular oxygen for oxides, as a component of the flux. The second purpose for using a background gas is to reduce the kinetic energy of the species in the plasma plume before hitting the substrate. It is shown that the kinetic energies of ions and other species in the plasma plume could be as high as several hundred electron volts. Such high energies could modify the stress state of the films through defects formation and could introduce compressive stress. Therefore, it is of interest to reduce the kinetic energy by using a background flow.

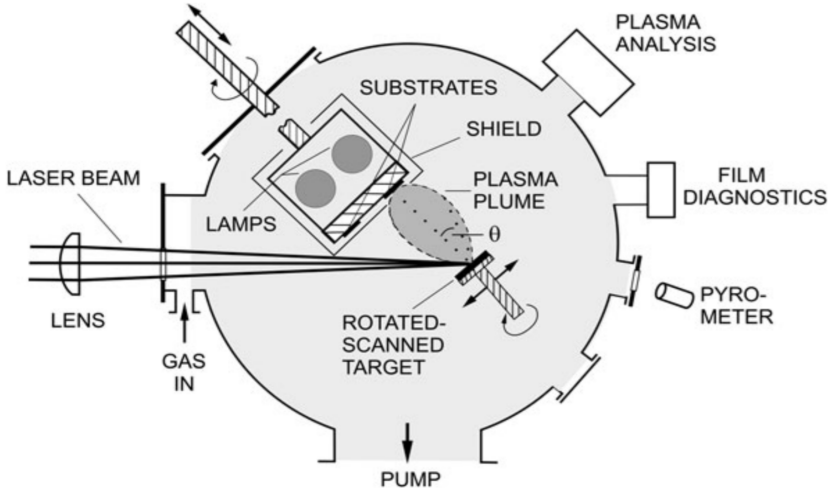

Figure 4.6: A schematic figure for the experimental setup for the PLD experiment. The most essential parts of the setup are the laser, reaction chamber, target and the substrate. Figure is taken from Ref. [75].

Another problem with PLD is the ejection of micron-size particles in the ablation process at the target. If such particles are deposited on the substrate, they affect the formation of multilayer devices structure. This occurs when the laser light penetrate too depth into the target material. To reduce this problem, it is possible to use velocity filters or use highly dense ablation targets and a wavelength from the laser with high absorption in the targets.

The plasma plume consists of electrons, ionized or neutral atoms, molecules, clusters and fragments, which is adsorbed, i.e. *the adhesion of molecules of gas, liquid, or dissolved solids to a surface* [78], on the substrate surface. The different species in the plume may react with each other and/or with the background atmosphere if it is not in vacuum. Some of the adsorbed species diffuses at the surface which results in a growth of the film. Surface diffusion increases with the increase of temperature, since it is a thermally activated process. The particles from the plasma needs a certain time after they impinging onto the substrate surface to allow diffusion and incorporate at proper site. This is why high-quality crystalline films need high temperatures to get reasonable grow rates. The time is also the reason why one have to adapt the laser-pulse-repetition rates to the material under investigation, substrate temperature and the flux of particles from the plume onto the surface. A problem that might occur during a PLD is the temperature on the substrate surface may change between each laser pulse.

Two possible parameters to vary in the thin-film growth are the substrate temperature and the pressure of the background gas. Increasing the substrate temperature results in normally a higher crystalline quality. While adjusting the pressure, for low pressure or vacuum, it is possible to grow epitaxial and large-grain oriented films. For higher pressures the situation changes significantly and favor vapor-phase condensation. This will hence results in formation of clusters and nanocrystals. These films have quite different physical properties compared with epitaxial and large-grain polycrystalline films, which could be entirely new composite materials formed in a reactive atmosphere for instance. In addition, it is possible to vary the repetition rate of the laser. Some problems occur with the repetition of the laser. If the rate is too large, the target temperature increase and the

material will be separated. On the other hand, if the rate is too low, the stoichiometry of the film may change where the properties of the films may get unwanted behavior.

The distance between the plasma plume and the substrate should be approximately the same as the visible plasma plume, with a typically length $l \approx 3 - 8$ cm. As a result, one can control the the energy of the species in the plasma plume impinging on the substrate. Since the plasma plume is not uniform and depends both on the plume size and shape, the thickness will not be uniform over the thin film. In addition, the morphology and microstructures of the thin films is determined, to a large extent, by the substrate temperature.

4.2.2 Samples of MoO_{3-x} from Pulsed Laser Deposition

Some of the samples used in this thesis of MoO_{3-x} were made by PLD by Mohammadreza Nematollahi. Two different series were made, where the first series had a growth temperature of 200 °C. The background gas here was only O_2 and the flow varied between 10 to 115 standard cubic centimeters per minute (sccm). With a constant pumping speed, this results in various chamber background pressures. The MoO_3 films were deposited simultaneously on both silicon and quartz substrates. The number of laser pulses hitting the target was 9000, except for one deposition a seen in Table 4.1, where the deposition parameters are listed. The first P in the sample name represents the deposition technique, in this case PLD. The Q, or Si, stands for the substrate for either quartz or silicon, respectively. x/y is the substrate temperature (x) and the gas flow in sccm (y).

Table 4.1: A summary of each sample with a sample name, kind of substrate, bakground gas flow (sccm), pressure (10^{-3}mbar) in chamber, substrate temperature and number of pulses from the laser for low growth temperature series from PLD.

Sample Name	Substrate	Flow (sccm)	Pressure (10^{-3}mbar)	Temperature (°C)	Number of pulses
P-Q-200/10	Q	10	2.5	200	5000
P-Si-200/10	Si	10	2.5	200	5000
P-Q-200/55	Q	55	25	200	9000
P-Q-200/115	Q	115	250	200	9000
P-Si-200/115	Si	115	250	200	9000
P-Q-200/85	Q	85	95	200	9000
P-Si-200/85	Si	85	95	200	9000
P-Q-200/95	Q	95	140	200	9000
P-Si-200/95	Si	95	140	200	9000

The second series had higher growth temperatures of 500 °C and 570 °C. A summary of deposition parameters can be found in Table 4.2, with the same setup as the Table 4.1. The number of pulses were set to 18 000 which resulted in significantly thicker samples than series one. The samples deposited with PLD did not have any post-treatment. It is the background flow of O_2 which decide the reduction fraction of MoO_{3-x}.

Table 4.2: A summary of each sample with a sample name, kind of substrate, bakground gas flow (sccm), pressure (10^{-3}mbar) in chamber, substrate temperature and an average thickness for high growth temperature series from PLD.

Sample Name	Substrate	Flow (sccm)	Pressure (10^{-3}mbar)	Temperature (°C)	Number of pulses
P-Si-500/65	Si	65	30	500	18000
P-Si-500/55	Si	55	25	500	18000
P-Q-500/55	Q	55	25	500	18000
P-Si-500/70	Si	70	-	500	18000
P-Q-500/70	Q	70	-	500	18000
P-Si-570/55	Si	55	25	570	18000
P-Q-570/55	Q	55	25	570	18000

4.2.3 Information About the Samples from Other Experiments

Some information about the samples was available from other experiments performed by Mohammadreza Nematollahi and Katherine Inzani. These experiments were not a part of this thesis, but will be presented since the information was used to create the final oscillator layer and model.

Scanning electron microscope (SEM) pictures for some of the samples from the low growth temperature series are shown in Figure 4.7, and for high growth temperatures in Figure 4.8. SEM pictures were only available for samples grown on silicon since conductivity is required. From the SEM pictures, it is possible to find an approximate thickness of the thin films, and are listed in Table 4.3. The thickness outside the brackets were given at the start of the thesis with the samples. The thicknesses inside the brackets are found from the SEM pictures in the figures. As seen in the table, the samples with 9000 pulses were significantly thicker than for sample P-Si-200/10 deposited with 5000 pulses. The thicknesses have large uncertainty as they are only measured by using SEM cross section images. This gives a reliable thickness for nearly the center of the sample, but not everywhere. Due to non-uniform plasma plume during the deposition it is not certain the surface is uniform. For some of the samples, the root mean square (RMS) roughness R_q and resistivity ρ are measured and the values are listed in the same table. The R_q value were found from atomic force microscopy (AFM). Transmittance measurements for the low growth temperature series from PLD are shown in Figure 4.9 and will be used as a reference to the transmittance measurements performed with SE, presented later.

For the series with high growth temperature, x-ray diffraction (XRD) was used to determine the phase composition of the films and x-ray photoelectron spectroscopy (XPS) determined the oxidation states presents in the films and the relative content of oxygen. From XRD and XPS, it was shown that P-Si-500/70 formed an orthorhombic MoO_3, i.e. α phase described in section 4.1.1, with weak reflections from Mo_4O_{11}. The band gap energy E_g was estimated from a Tauc plot for indirect transition and was found to be $E_g = 3.2$ eV from transmittance measurements. For sample P-Si-500/55, there was reflections of both Mo_4O_{11} and MoO_2. As seen from Figure 4.8 (b), the sample consists of columnar grains which is suggested to be mainly Mo_4O_{11}, while the MoO_2 is confined to the bottom. P-Si-570/55 showed mainly MoO_2 reflections with weak reflections from Mo_4O_{11}. For sample P-Si-500/70 and P-Si-500/55, amorphous phases could be present in

the samples. It could also be nitrogen in the samples which will give a higher formation of oxygen vacancies.

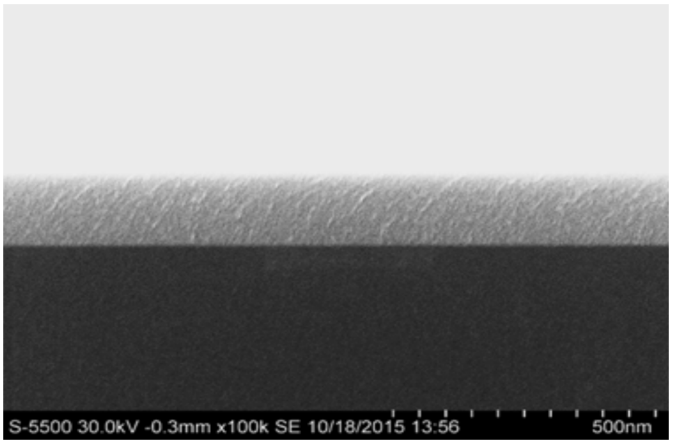

(a)

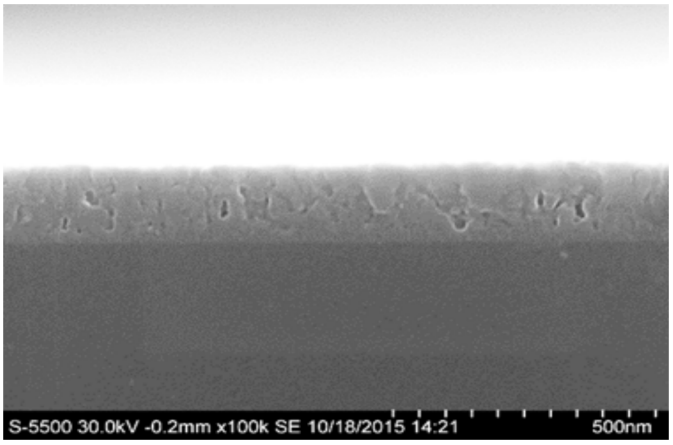

(b)

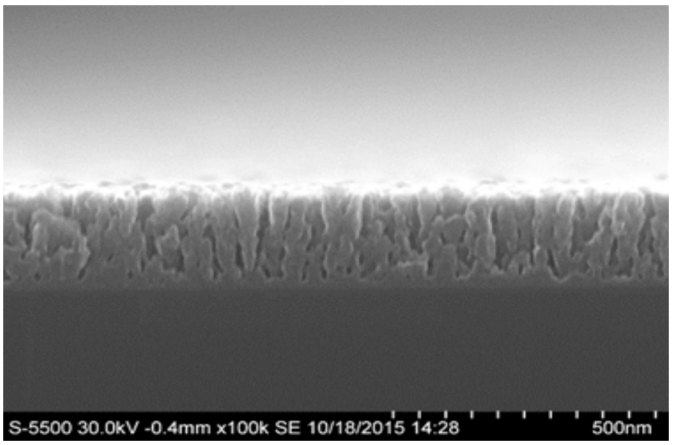

(c)

Figure 4.7: (a) SEM pictures for sample P-Si-200/10 with low growth temperature. (b) As (a), but P-Si-200/55. (c) As (a), but P-Si-200/95.

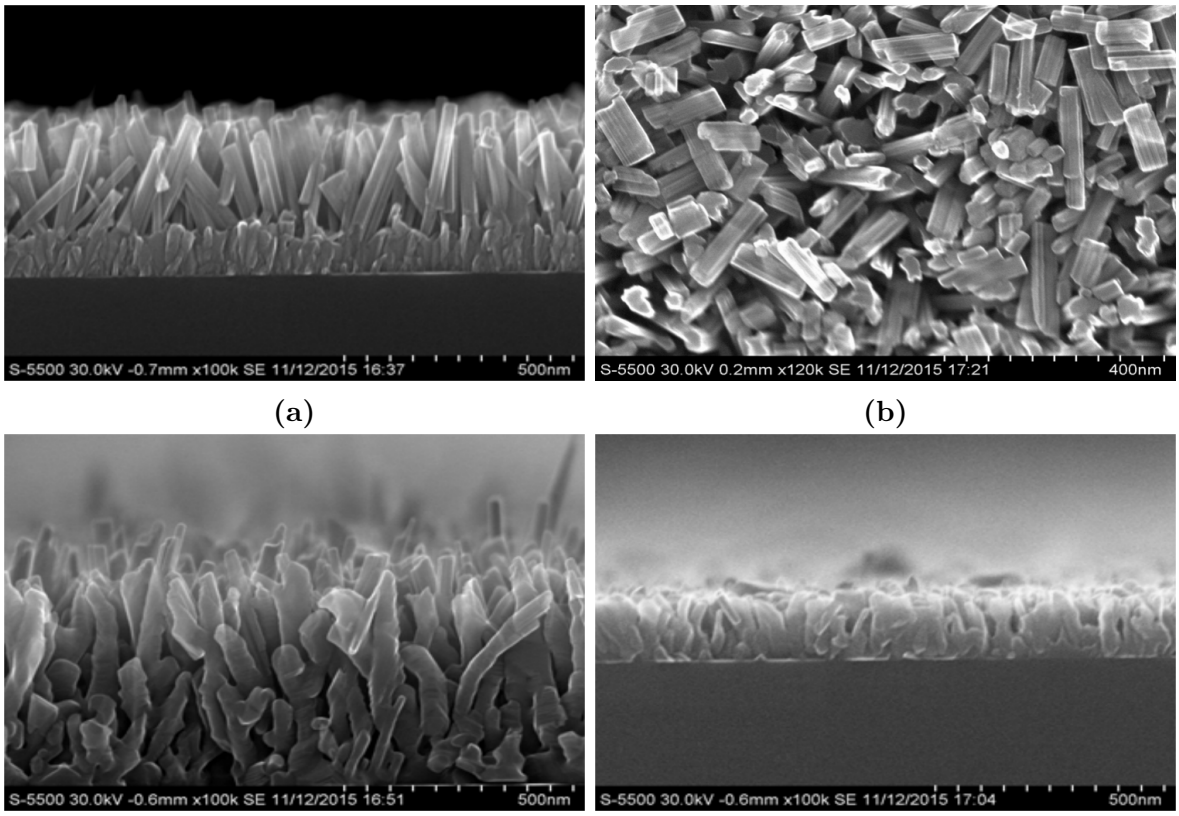

Figure 4.8: (a) SEM pictures for sample with high growth temperature P-Si-500/55. (c) As (a), but P-Si-500/70. (d) As (a), but P-Si-570/55. (b) Top view SEM picture for sample P-Si-500/55.

Table 4.3: Overview of the thickness of the samples, the root mean square roughness from AFM and resistivity. The thickness outside the brackets were given at the start of the thesis, and inside the brackets thickness obtained from the SEM pictures. The thicknesses for quartz were not available due to the requirement for conductivity during SEM experiments.

Sample Name	Thickness (nm)	R_q (nm)	Resistivity (Ω m)
P-Si-200/10	65 [75]	-	0.00231
P-Si-200/55	160 [170]	-	-
P-Si-200/85	170	-	-
P-Si-200/95	190 [200]	-	-
P-Si-500/55	400 [410]	25.9	0.00909
P-Si-500/70	570 [540]	37.5	-
P-Si-570/55	175 [200]	13.1	0.0166

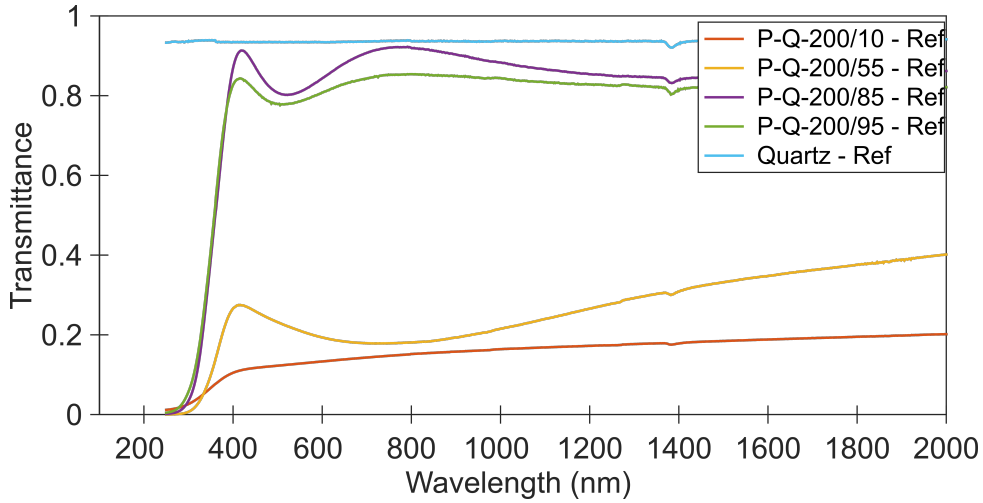

Figure 4.9: Transmittance measurements for the low growth temperature series from PLD, performed by Mohammadreza Nematollahi.

4.3 The Spin Coating Technique

Spin coating is one of the chemical solution deposition technique [79]. The first step in this process is the preparation of a precursor in liquid phase, typically a salt of carboxylates or other metallo-organic compounds. Further, an appropriate solvent is used to dissolve the precursor and create a stoichiometric accurate composition of the film. The next step is to deposit the solution on the substrate by spin coating, spray coating, blade coating or dip coating. For the spin coating technique, one typically use a sol-gel or a liquid phase precursor on the substrate. The substrate is held in spinner by applying a vacuum to the backside of the substrate. To spread the solution on the substrate, the solution is spun in the spinner at high velocity, typically with a velocity between 1000 to 8000 rpm. The thickness is dependent on the angular speed, viscosity and the time in the spinner. To increase the thickness, it is possible to repeat the deposition and spin the substrate again. This is a fast way to deposit thin films and is therefore an excellent technique at laboratory scale. One disadvantage is the incompatibility from the roll-to-roll printing technique to deposit on large areas. Therefore, this is not a good technique for industrial applicability. At last, the as-deposited film is dried, crystallized by heating and optionally post-annealed for further properties. A schematic figure of the process is shown in Figure 4.10.

4.3.1 Samples of MoO_3 with the Spin Coating Technique

The samples of the reduced MoO_{3-x} fabricated with the spin coating (SC) technique was performed by Katherine Inzani [48]. Two different series were made with different concentration of Mo cation per liter of solution, where ammonium heptamolybdate $(NH_4)_6Mo_7O_{24}$ was used, with distilled water as the solvent. The two series had concentrations of 0.1 and 0.5 Mo cation per liter of solution and the concentration of Mo correlated with the thickness of the samples, i.e. approximately 10 nm for 0.1 concentration of Mo and 60 nm for 0.5 concentration of Mo. The thicknesses were measured by profilometry,

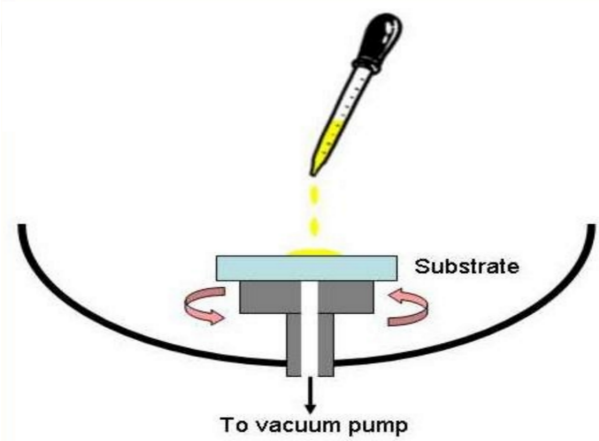

Figure 4.10: A schematic figure for the experimental setup for the spin coating experiment with a substrate held at a spinner by a vacuum and the solution in the middle. Figure is taken from Ref. [80].

with an uncertainty ± 5 nm. After the deposition of the films, they were annealed in a rapid thermal process, i.e. heating quickly, up to 400 °C and held for 10 minutes in a oxygen atmosphere (flow rate at 200 sccm). This is done to end up with crystalline MoO_3 films. One of the sample from the series with a concentration of 0.1 Mo was annealed at 300 °C, which resulted in an amorphous film instead of a crystalline. At last, the films had a post-treatment in hydrogen gas (flow rate at 1000 sccm) to remove oxygen from the MoO_3 films. This results in a mixture of different phases of molybdenum oxides, including MoO_2 and Mo_4O_{11} in different proportions. This was done in a rapid thermal process with different temperatures for 30 minutes. Higher temperature results in more reduced MoO_{3-x} films. One of the samples did not have any post-treatment. A sample name and an overview of the properties of each film can be found in Table 4.4. The sample name first consist of SC because of the SC technique. Thereafter a C due to crystalline MoO_3 film, with the concentration of $(NH_4)_6Mo_7O_{24}$. At last, the post-treatment temperature is specified for each sample, where NT had no post-treatment annealing. In the table, only the crystalline films are shown, as the amorphous sample was not examined in this thesis.

4.3.2 Information About the Samples from Other Experiments

Some information from other experiments was also available here, determined by Katherine Inzani. An overview of the root mean square roughness R_q and the average roughness R_a for the samples for both series are in Table 4.5 which were determined from AFM over a 10 μm x 10 μm area. As for the PLD series, XRD and XPS measurements were performed to determine information about the samples. XRD measurements showed that the as-deposited samples were amorphous while annealing up to 300 °C. Annealing to 400 °C crystallized the films in a multicrystalline-grain arrangement. Under the post-treatment annealing, the structures were not affected while annealing at 200 °C. For heating up to 300 °C, the thinner films started to reduce while the thicker ones remained unchanged. While increasing the temperature up to 400 °C, large areas of the substrate was exposed, but the thicker films was intact. For higher temperatures the thinner films totally disintegrated and provided little coverage of the substrate. The thicker films becomes inhomogeneous and had large roughness at the surface. XRD did not give much

Table 4.4: Table with a sample name and the different properties of the sample. The concentration is the moles of Mo cation per liter of solution and indicate the thickness of the films. Next, the post-treatment temperatures in the hydrogen environment are listed. At last, other important information

Sample	Concentration	Post-treatment (°C)	Other information
SC-C05-NT	0.5	No treatment	
SC-C05-200	0.5	200	Not affected
SC-C05-300	0.5	300	Started to reduce
SC-C05-350	0.5	350	
SC-C05-400	0.5	400	Contributions from Mo_4O_{11}, weak MoO_2
SC-C05-450	0.5	450	
SC-C01-NT	0.1	No treatment	
SC-C01-200	0.1	200	Not affected, no MoO_2
SC-C01-300	0.1	300	Not affected, MoO_2
SC-C01-350	0.1	350	No MoO_2
SC-C01-400	0.1	400	Mainly MoO_3, weak Mo_4O_{11}
SC-C01-450	0.1	450	

information about the reduced phases, especially for the thinner films. The thicker films showed reflections of Mo_4O_{11}. XPS results for the SC-C01-400 showed large contributions from the intermediate phases, such as Mo_4O_{11} and weak results from MoO_2. For sample SC-C05-400, the results showed mainly MoO_3 phases, with a small fraction of intermediate phases. No MoO_2 is assumed to be present in the thicker films annealed up to 400 °C. The films were too thin to perform any resistivity measurements to determine the conductivity.

Table 4.5: Overview of the root mean square roughness R_q and the average roughness R_a for the samples for both series from SC.

Sample	Rq (nm)	Ra (nm)
SC-C01-NT	1.16	0.85
SC-C01-200	1.15	0.9
SC-C01-300	0.745	0.53
SC-C01-350	-	-
SC-C01-400	3.5	1.2
SC-C01-450	-	-
SC-C05-NT	1.53	1.17
SC-C05-200	1.58	1.25
SC-C05-300	1.61	1.25
SC-C05-350	1.84	1.45
SC-C05-400	1.91	1.48
SC-C05-450	19.2	12.3

4.4 Spectroscopic Ellipsometry

The theory in this section can be found in [81], [82] and [83]. Spectroscopic ellipsometry (SE) is a technique that uses polarized light to characterize thin films, surfaces and material microstructure and is a non-destructive optical technique. The technique was first introduced and developed by Drude in 1887 and many of the equations used today were derived by himself. Firstly, the measurements were operated manually and was a time consuming measurement. In the period from early 1970s and up to recent late 1990s, the technique developed fast and today SE is a fast and automated process that can be used in many areas. SE offers three main advantages: precision, sensitivity and information. Since SE measures two variables at each wavelength, the information is doubled compared to an intensity reflection, or transmission measurement. Since the change in polarization and amplitude is defined as a ratio, the SE is not sensitive to the changes in absolute intensity and hence the sample itself works as a reference. Since SE measurements contains phase information it is possible to examine films much thinner than the wavelength of the light. It is possible to use SE to determine optical constants, layer thickness and a lot of other physical constants that provides information about the sample. In the next subsections, the theory and other relevant information to understand SE is presented.

4.4.1 Spectroscopic Ellipsometry Theory

The measured variables in SE are Ψ and Δ, which are related to Fresnel reflection coefficients r_p and r_s for p- and s-polarized light respectively. This is a complex number given by

$$\rho = \frac{r_p}{r_s} = \tan(\Psi)e^{i\Delta}, \tag{4.4.1}$$

where ρ is defined as the ratio between r_p and r_s, and Ψ and Δ are the measured variables. $\tan(\Psi)$ can here be seen as the magnitude of the reflectivity ratio and Δ is the phase. The basic principle of a SE measurement is shown in Figure 4.11, where linearly polarized light, for instance oriented at $+45°$ to the axis with an angle of incidence ϕ, is incident to a sample. The linear polarized light is hence reflected and a phase shift will arise and make elliptically polarized light. This is due to the reflection coefficients differ significantly for p- ans s-polarization and one observes different changes in amplitude and phase. Thus, the change in the polarization state is a measure of the variation of light reflection. The p-plane is lying in the plane of incidence (hatched area and is normal to the sample) and the s-plane is perpendicular to the p-plane. Thus, the propagation, p-plane and s-plane define a right-handed Cartesian coordinate system. For a simple sample structure, the Ψ is characterized by the refractive index n, and Δ represents light absorption described by the extinction coefficient k. That means n and k can directly be obtained by measuring Ψ and Δ, and by applying Fresnel equations that will be described later.

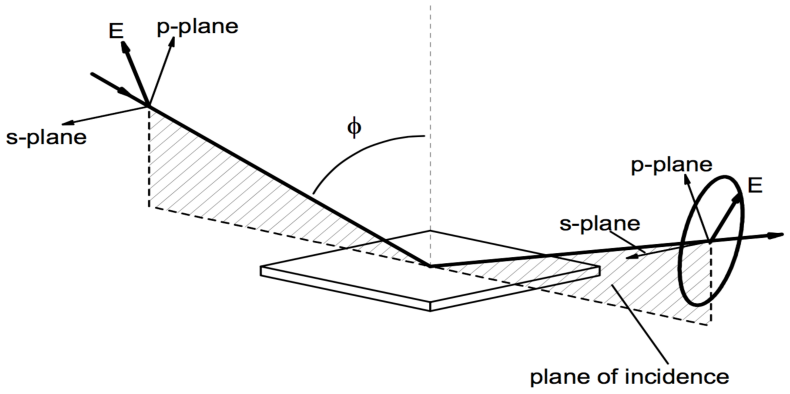

Figure 4.11: A schematic figure of a typically SE measurement, where linearly polarized light is reflected off a sample which will give elliptical polarized light. The p-plane is in the plane of incidence (hatched area) and the s-plane is perpendicular to the p-plane. Figure is taken from Ref. [81].

Optical Constants

Before proceeding with the Fresnel equations, optical constants need to be introduced. Optical constants are physical quantities that characterize the material while it is excited by an electromagnetic field at a desired frequency. These constants are n, k, ϵ_1 and ϵ_2 where there are two important relationships. The first one is the complex index of refraction defined as

$$N = n + ik, \tag{4.4.2}$$

where n is the refractive index and k is the extinction coefficient of the material. This equation governs information about change in phase and amplitude as the waves propagates through the medium. The second relationship is the complex dielectric function defined as

$$\epsilon = \epsilon_1 + i\epsilon_2. \tag{4.4.3}$$

Equation (4.4.3) governs information about how the material responds to an applied electrical field

Equation (4.4.2) and (4.4.3) are closely related by

$$\epsilon = N^2 \tag{4.4.4}$$

which leads to

$$\epsilon_1 = n^2 - k^2, \qquad \epsilon_2 = 2nk. \tag{4.4.5}$$

That means equation (4.4.2) describes the electromagnetic waves propagation through a medium, while equation (4.4.3) relates to how the material react to an electromagnetic wave. The optical constants describes two different properties, but are closely connected. Which of the constants one use is usually determined by the method, or application. In addition, ϵ_2 is an important quantity while one look at absorption of light as it is proportional to the extinction coefficient k. I.e. the peaks in the ϵ_2 function represents the area where the material absorbs the incident photons for approximately constant n. The dielectric function and models will be presented more closely in Chapter 5.

Kramer-Kronig Relations

In equation (4.4.2) and (4.4.3), the real and imaginary parts of the function are not independent quantities, i.e. if ϵ_1, varies also ϵ_2 changes. This is taken into account in the Kramer-Kronig (KK) relations. For the complex dielectric functions variables ϵ_1 and ϵ_2, these relations are given by [83]

$$\epsilon_1(\omega) = 1 + \frac{2}{\pi} P \int_0^\infty \frac{\omega' \epsilon_2(\omega')}{\omega'^2 - \omega^2} \, \mathrm{d}\omega', \tag{4.4.6}$$

and

$$\epsilon_2(\omega) = -\frac{2\omega}{\pi} P \int_0^\infty \frac{\epsilon_1(\omega' - 1)}{\omega'^2 - \omega^2} \, \mathrm{d}\omega', \tag{4.4.7}$$

where P is the polarization of the medium and ω is the angular frequency of the incident wave. For the complex index of refraction it is possible to find a similar relation between n and k. Thanks to these relations, it is possible to find the imaginary (real) part if the real (imaginary) part is known. For a model to be physically correct, the KK-relations needs to be satisfied as they follow causality, i.e. the absorption happens after the light enters the medium. To desire which model to use to extract the dielectric function of a material, the KK-relations must be respected.

Fresnel reflection

Fresnel equations are Maxwell's equations applied at a boundary between two materials. If the light field is assumed to be plane waves on the form $E \propto \exp\left(i(k_x x + k_z z - \omega t)\right)$, i.e. the wave vector lies in the x and z plane called the plane of incidence, and solve the wave equation, some important results are obtained. The first thing one can find is that the reflected and incident angle must be equal. The second properties is the well known Snell's law $n_0 \sin(\phi_0) = n_1 \sin(\phi_1)$, where n_0 and n_1 are the index of refraction of the incident wave and the sample respectively. ϕ_0 is the angle between the normal to the sample and the incident wave, while ϕ_1 is the angle of propagation in the sample to the same normal. The third and last step is to use these two results and find the Fresnel reflection coefficients both for p- and s-polarized light, defined as

$$r_p = \frac{n_1 \cos(\phi_0) - n_0 \cos(\phi_1)}{n_1 \cos(\phi_0) + n_0 \cos(\phi_1)}, \tag{4.4.8}$$

and

$$r_s = \frac{n_0 \cos(\phi_0) - n_1 \cos(\phi_1)}{n_0 \cos(\phi_0) + n_1 \cos(\phi_1)}. \tag{4.4.9}$$

Inserting equation (4.4.8) and (4.4.9) into equation (4.4.1), the behavior of Ψ and Δ is examined as function of incidence for different choices of the index of refraction for the sample. If the incident medium is air or free space, then $n_0 = 1$. It is important to note that all n_0 and n_1 may be complex numbers if the medium of the sample absorbs some of the incident wave and can change with the complex index of refraction function.

The results in equations (4.4.8) and (4.4.9) are obtained for bulk materials which is a bare substrate without overlayers, or coatings. For a thin film deposited on an absorbing substrate, or infinitely thick substrate, the reflecting beams from the transition between the

two mediums needs to be taken into account. An example is shown in Figure 4.12 where there are in principle an infinite number of reflections and transmissions. However, since the beams splits up, the amplitude decreases rapidly and the beams dies out. Absorption will in addition attenuate the intensity. The Fresnel equations for reflection, (4.4.8) and (4.4.9), are valid locally at all interface between two different mediums. The same yields for transmission equations which is outside the scope of this thesis. As a result, this give us the opportunity to calculate Fresnel reflection coefficients as function of film indices of refraction and the angle of incident that are valid for all mediums (air and film interfaces). This holds for all interfaces, and can be illustrated as

$$r_{jk,p} = \frac{n_k \cos(\phi_j) - n_j \cos(\phi_k)}{n_k \cos(\phi_j) + n_j \cos(\phi_k)}, \quad r_{jk,s} = \frac{n_j \cos(\phi_k) - n_k \cos(\phi_j)}{n_j \cos(\phi_k) + n_k \cos(\phi_j)}. \tag{4.4.10}$$

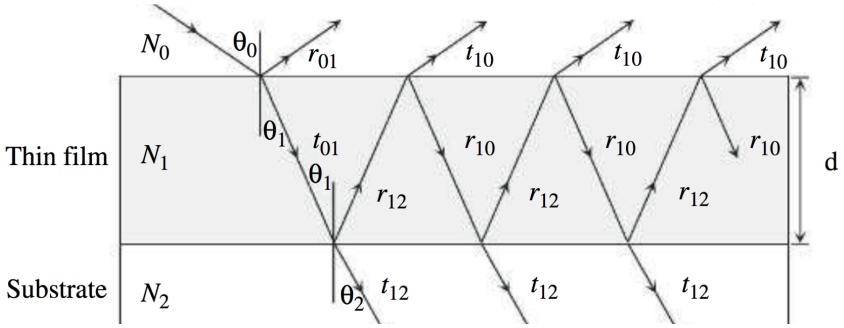

Figure 4.12: Illustrates reflections and transmissions between air (N_0) and the thin film with thickness d with the index of refraction N_1. Further the transmitted wave in the thin films again is reflected and transmitted in the transition from the thin film to the substrate with index of refraction N_2 and so on. Figure is taken from Ref. [82].

The final wave after propagation through the film is $E_f = E_i \exp(-i2\beta)$, where E_i is the initial state of the wave. β is the optical thickness defined as

$$\beta = 2\pi \frac{d}{\lambda} \sqrt{n_1^2 - n_0^2 \sin^2(\phi_0)}, \tag{4.4.11}$$

where d is the film thickness and λ is the wavelength. It is possible to find the n'th reflected wave as

$$E_n^r = t_{10} t_{01} (r_{10})^{n-2} (r_{12})^{n-1} e^{-(2n-2)\beta} E_i, \tag{4.4.12}$$

where $t_{j,k}$ and $r_{j,k}$ is the transmission and reflection coefficients respectively between medium j and k. The amplitude reflection coefficient can be written as a sum of the reflected beams as

$$E_{\text{total}}^r = \left[r_{01} + t_{10} t_{01} e^{i2\beta} \sum_{n=2}^{\infty} (r_{10})^{n-2} (r_{12})^{n-2} e^{-i2n\beta} \right] E_i. \tag{4.4.13}$$

Using that $r_{01} = -r_{10}$ and $t_{10} t_{01} = 1 - r_{01}^2$ and the fact that the sum is a convergent series, equation (4.4.13) can be rewritten as

$$E_{\text{total}}^r = \left(\frac{r_{01} + r_{12} e^{-i2\beta}}{1 + r_{01} r_{12} e^{-i2\beta}} \right) E^{\text{incident}}. \tag{4.4.14}$$

This method is valid both for p- and s-polarized beams, while the respective r_p and r_s Fresnel reflection coefficients are used. Thus one can find the pseudo-Fresnel coefficients $\tilde{R}_p$ and $\tilde{R}_s$ as

$$\tilde{R}_p = \frac{r_{01,p} + r_{12,p}e^{-i2\beta}}{1 + r_{01,p}r_{12,p}e^{-i2\beta}}, \quad \tilde{R}_s = \frac{r_{01,s} + r_{12,s}e^{-i2\beta}}{1 + r_{01,s}r_{12,s}e^{-i2\beta}}. \tag{4.4.15}$$

$\tilde{R}_p$ and $\tilde{R}_s$ can hence be connected to Ψ and Δ through

$$\tilde{\rho} = \tan(\Psi)e^{i\Delta} \equiv \frac{\tilde{R}_p}{\tilde{R}_s}. \tag{4.4.16}$$

Thus, it is possible to calculate the film thickness through equation (4.4.11) and other physical properties. The same method can be expanded to take into account for more complex structures and can also be used for the transmitted beams.

Mueller-Stokes Formalism

Since the real samples can depolarize the incident light, Mueller-Stokes formalism needs to be used. Usually, Jones vectors are used to describe polarized light, but Jones vectors fails for unpolarized. To describe both unpolarized light and partial polarized light, the Stoke parameters are used instead of Jones vectors. The Stoke parameters describes all states of light and in SE measurement these parameters are measured. The Stokes parameters may be given as a vector and is defined as

$$S = \begin{pmatrix} S_0 \\ S_1 \\ S_2 \\ S_3 \end{pmatrix} = \begin{pmatrix} I_x + I_z \\ I_x - I_y \\ I_{+45\,\mathrm{deg}} - I_{-45\,\mathrm{deg}} \\ I_R - I_L \end{pmatrix}, \tag{4.4.17}$$

where S_0 is the total light intensity, S_0 to S_3 are the Stoke parameters as function of the linear polarization in the x direction I_x, the liner polarization in the y direction I_y, the linear polarization I_{-45° and I_{+45° at at $\pm 45^\circ$ respectively and the left- and right-circular polarization I_L and I_R. If the light intensity S_0 is normalized, i.e. setting $S_0 = 1$, the degree of polarization p is given by

$$p = \sqrt{S_1^2 + S_2^2 + S_3^2}, \tag{4.4.18}$$

where $p = 1$ for polarized light, $p = 0$ for unpolarized and $p < 1$ for partial polarized light.

The Stokes vector could be transformed by a 4 x 4 matrix (Muller-Matrices) which represents the optical elements the Stokes vector are sent through. This matrix is on the form

$$\mathbf{M} = \begin{pmatrix} 1 & m_{12} & m_{13} & m_{14} \\ m_{21} & m_{22} & m_{23} & m_{24} \\ m_{31} & m_{32} & m_{33} & m_{34} \\ m_{41} & m_{42} & m_{43} & m_{44} \end{pmatrix}, \tag{4.4.19}$$

where m_{ij} are different elements that depends on the setup and/or sample. If the sample is isotropic, the Mueller matrix is simple and is given as

$$\mathbf{M}_{\text{isotropic}} = \begin{pmatrix} 1 & -N & 0 & 0 \\ -N & 1 & 0 & 0 \\ 0 & 0 & C & S \\ 0 & 0 & -S & C \end{pmatrix}, \tag{4.4.20}$$

where $N = \cos(2\Psi)$, $S = \sin(2\Psi)\sin(\Delta)$ and $C = \sin(2\Psi)\cos(\Delta)$. If there are N optical elements given by a Mueller matrix $\mathbf{M}_i$, the final Stoke vector is given by

$$S_f = M_N M_{N-1} ... M_2 M_1 S_i, \tag{4.4.21}$$

there S_i is the initial Stoke vector and S_f is the final state of the polarized, unpolarized or partial polarized light. For other samples and optical setups, the Mueller matrices could take form in complex forms that will not be presented in this thesis.

To analyze the polarization state one can either measure a discrete number of states, or it could be continuously measured [84]. For discrete number of states, it is required at least 16 intensity measurements, i.e. four probing states and four analysis states. In the continuously, it is a rotating compensator which measure the polarization states continuously and is time dependent due to the rotation of the compensator. The intensity is dependent on 32 Fourier coefficients which are functions of Mueller Matrix elements. Typically, a fast Fourier transform is used on the intensity measurements to determine the Mueller Matrix elements for continuously measurements.

4.4.2 Experimental Setup

To perform the SE measurements, the RC2 Model XI ellipsometer provided by J. A. Woollam Co., Inc was used. A figure of the setup is shown in Figure 4.13. Number 1 is the light source, which is a 150W Xenon lamp that is turned on by using the RC2 Electronics box. To achieve good measurements, it is recommended to let the light warm up for at least 30 minutes to obtain stable spectra. Number 2 in the figure is the source optics that contains an achromatic lens that collimate the beam before it is passed through a fixed MgF_2 Rochon polarizer element. At last, the beam is sent through an achromatic prisms compensator that rotates at 10 Hz. The standard sample mount is represented by number 3 in the figure. The sample mount may be changed with another sample mount depending of the type of measurements. For instance, it is possible to use a translation stage, or a rotation stage instead of the standard. To hold the sample in the right position at the sample mount, a Linicon LV-125A vacuum pump is used. Number 4 in the figure represents the receiver optics that contains at first a through-hole quadrant detector. Thereafter, the beam passes through a new continuously rotating compensator at 6 Hz before entering the detectors, or spectrometers, which are represented by number 5 in the figure. The first one is for ultraviolet (UV) and visible light (VIS) in the range 193-1000 nm, using a Si CCD detector. The second detector is for near infrared (NIR) in the range 1000-1700 nm by using an InGaAs photodiode array. Finally, number 6 represents the auto angle vertical sample mount that rotates to the angle of incidence [85]. Measurements in this thesis uses the standard sample mount with focus probes to decrease the size of the beam. These probes can be both attached to the receiver optics

and source optics and should be used for non-uniform samples. For samples made with PLD, the thickness may not be uniform and the beam size is too large. If this is the case, the beam will depolarize and affect the results.

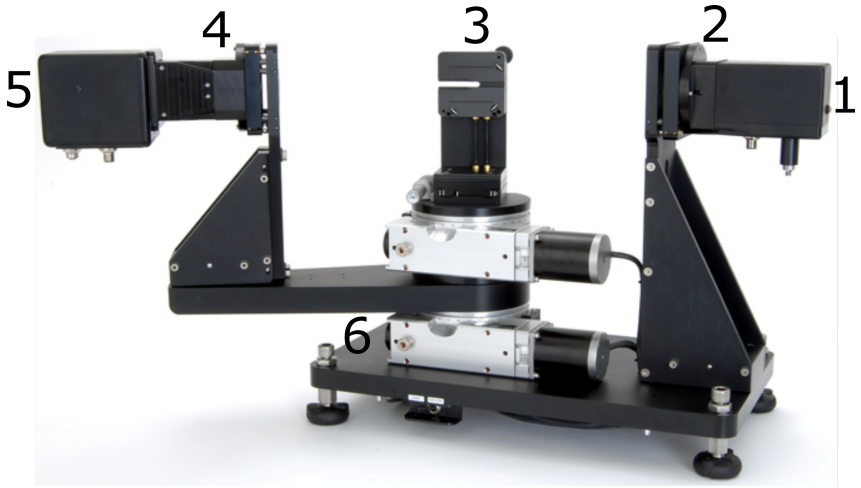

Figure 4.13: Experimental setup with 1) Light source. 2) Source optics. 3) Sample mount. 4) Receiver optics. 5) The detectors. 6) Auto angle vertiacl sample mount. Figure is taken from Ref. [86].

Before a measurement, the system must be aligned by a straight-through alignment, with help from a red nose cone which sense the beam position. If the system is not perfectly aligned, this can be adjusted at the source and receiver optics. The sample mount is used to adjust the sample position to optimize the intensity and beam signal. In addition, one needs a tweezers to pick-up the samples to and from the sample mount and glows for protection.

All SE measurements in this thesis were done at angles of incidence in the range between 55° - 75° with 5° interval for 10 seconds at each angle. Measurements both with and without focus probes were done for all samples. For samples deposited on quartz, transmittance measurements were performed in addition to obtain more useful information in the modeling, for 10 seconds. Due to large thickness variation on the sample surface from the PLD series, the measurements were performed with focus probes at the middle of the sample for the PLD series.

4.4.3 Data Analysis - CompleteEASE

The data analysis is an important part of the SE experiment. To determine the optical constants and the thickness of the layers in a sample, a model based analysis of the data from the measurements is performed. The only exception from this rule is for bulk materials where it is possible to calculate the so called "Pseudo" dielectric function defined as

$$\langle\epsilon\rangle = \langle\epsilon_1\rangle + i\langle\epsilon_2\rangle) = (\langle n\rangle + i\langle k\rangle)^2 = \sin^2(\phi)\left[1 + \tan^2(\phi)\left(\frac{1-\rho}{1+\rho}\right)^2\right] \tag{4.4.22}$$

where ϕ is the angle of incidence and ρ is defined in equation (4.4.1).

A typically method of the analysis is illustrated in Figure 4.14. The first step is to perform the SE measurements to obtain the experimental data. The second step is to

build a layered optical model which is used to generate SE data. Thirdly, the model fit parameters are defined and the software adjust the fit parameters automatically to improve the agreement between the model generated SE data and the experimental data. Finally, the results of the fit are evaluated and if the result is not acceptable, step two is performed to adjust and define fit parameters before running a new fit. The evaluation of the fit is one of the most important steps in the analysis and for a model fit to be acceptable, the mean square error (MSE) should be in the range 0.5-2 for thin film samples and 10-20 for thicker films. In addition the model should be unique which is easiest to obtain while the model is simple. Only layers, or other optical properties that significantly decrease the MSE, should be used. At last, the fit parameters must be physicals. For instance, k can not be a negative number, or $n > 10$.

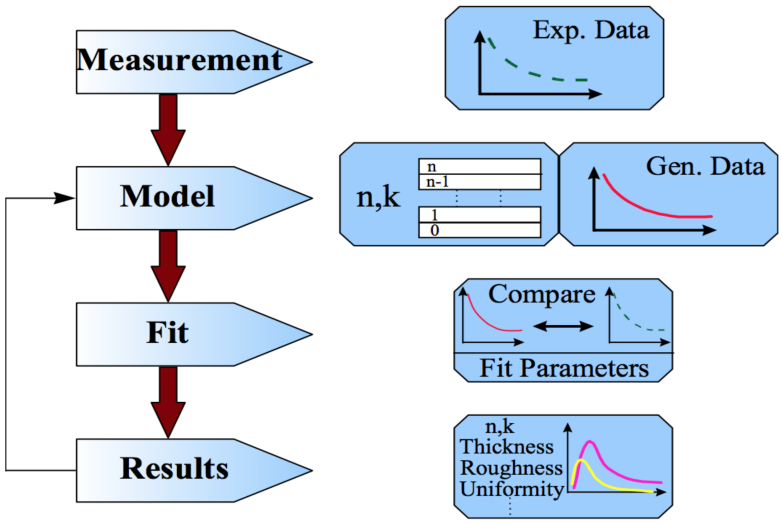

Figure 4.14: Illustrates the typically procedure to analyze the data obtained from the SE measurements in the CompleteEASE software. Figure is taken from Ref. [81].

The software CompleteEASE (version 4.64) is used to acquire and analyze the data obtained from SE measurements in this work.

Mean Square Error

A measure of the goodness of fit is the mean square error (MSE) [87]. It is a way to quantify how well the optical model agree with the experimental measurements. This is an important process in the analysis of the SE measurements. The MSE is defined as

$$MSE = \sqrt{\frac{1}{3n-m}\sum_{i=1}^{n}[(N_{E_i}-N_{G_i})^2+(C_{E_i}-C_{G_i})^2+(S_{E_i}-S_{G_i})^2]}\text{x}1000, \qquad (4.4.23)$$

where n is the number of wavelengths, m is the number of fit parameters and N, C and S as defined in equation (4.4.20). The subscription E and G is the experimental and the model generated variable, respectively. The reason that N, C and S are used instead of Ψ and Δ is that they are in the range -1.0 to 1.0 and the rotating compensator ellipsometer measure approximately the same accuracy and precision on any sample. The multiplication factor of 1000 is due to the precision and accuracy in the measured parameters N, C and S which implies an ideal model fit to have a $MSE = 1$. Normally

this value is much larger, but lower the MSE value indicate a better agreement between the model and the experimental values.

Multi-Sample Analysis

Multi-Sample analysis is a feature in the CompleteEASE software that allows different types of samples to be fitted together. Each sample has its own fit parameters, but some of these fit parameters may be common for all types of the samples. For instance, the thickness of a sample may vary over the surface, but have the same band gap energy E_g. Hence, it is possible to fit the optical parameters in a so-called global fit environment, i.e. they are the same for all samples, and fit the thickness alone for each sample in an individual fit environment.

Roughness Layer

To model the roughness layer (RL) there are several opportunities. The most common is to use the roughness function in the software which is efficiently an effective medium approximation (EMA) (presented later), with a mixture of 50 % void and material [87]. The only possible fit parameter here is the thickness of the layer. The 50/50 method of void and materials is not necessary a good model for the materials. For this types, graded layer is a possibility. The grading are done by dividing the layer into a number of layers specified by the user of the software. Each of these slices will have varying optical constants for approximate the index gradient profile.

There are four possibilities of grading types. The simplest one is the simple, where only the percentages of inhomogeneity is the fit parameter. It allows linear variation of the refractive index and can either increase or decrease from the bottom to the surface depending on the sign. This grade does not affect the extinction coefficients and therefore will not be used in this thesis. The next grade type is the linear which behave the same as the simple one, but will affect the extinction coefficient, in addition. The linear grade uses an EMA to mix the material with void, depending on the offset and slope which are the fit parameters here. The offset defines the point where the void goes to zero in the material, and the slope defines the slope of the linear variations through the film. It is important to note here if the offset is greater than zero the void can goes to negative values in the bottom and hence is not necessarily a physical representation. It is rather a mathematical calculation to adjust the optical constants up and down.

The third possibility is the non-linear variant of the graded layer. It is essential the same as the linear with an EMA, but instead of varying linearly, it allows an exponential varying. This variation can either be symmetric, or not, about the center of the layer. It is possible to vary the layer, depending on if the exponential is greater, or lower than one. A couple of examples are show in Figure 4.15, where the exponential are set to 2.5 and with symmetry in (a) and without in (b). The mix cannot be negative in this case, and therefore it has a more physical interpretation for the variation of void in the RL. The fourth and last type of graded variation is a parametric grade, but is beyond the scope for this thesis.

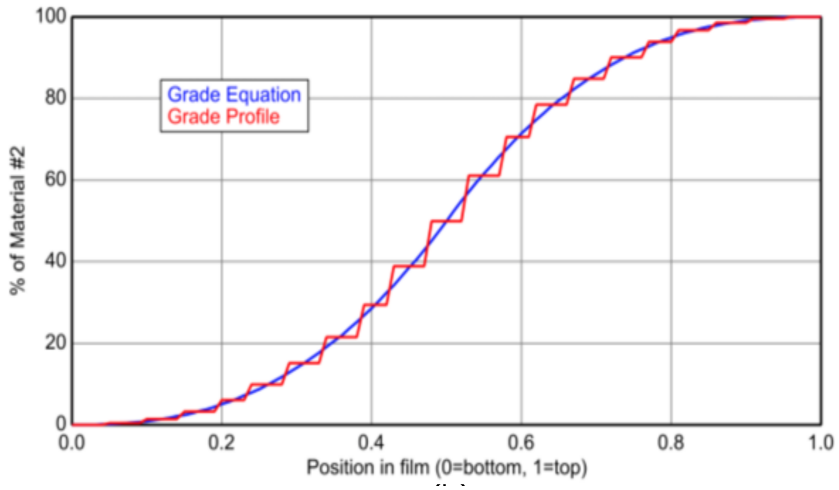

(a)

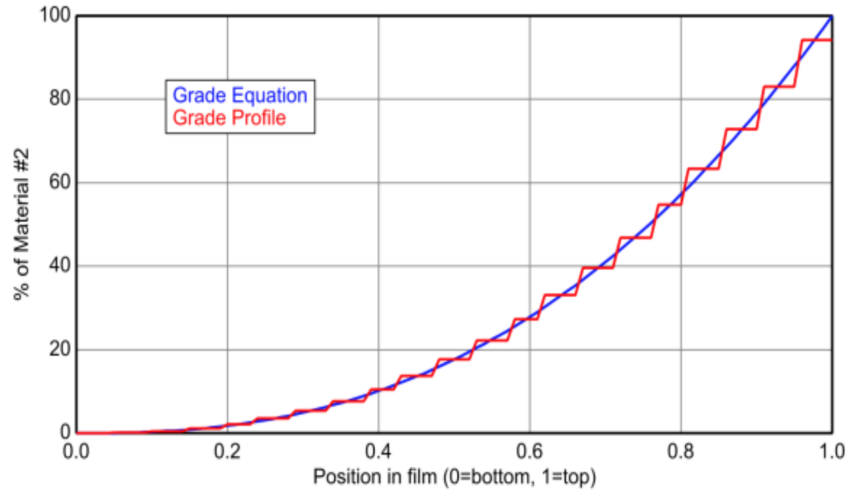

(b)

Figure 4.15: (a) Example of the non-linear variation in the film where the grade equation is the blue line and the grade profile in the software is the red line. The exponential are set to 2.5 with the symmetry on. (b) As (a), but with asymmetry. Figure is taken from Ref. [87].

Chapter 5

The Dielectric Function

This chapter takes a more detailed look on the dielectric function (DF), and explains different models that can be used to model the behavior of the DF. In the last three sections, three phenomena that affects the DF are presented.

5.1 The Dielectric Function - Theory

The magnitude of polarization inside a material is described by the dielectric constant, or the DF, ϵ. If a dielectrics is placed between a capacitor, the electric field is given by [83]

$$E = \frac{D}{\epsilon_p}, \tag{5.1.1}$$

where D is the electric displacement and ϵ_p is the permittivity of the dielectric. ϵ_p is generally greater than ϵ_0, which is the free space permittivity. The surface charges on the capacitor generates a polarization P given by

$$P = \chi \epsilon_0 E, \tag{5.1.2}$$

where χ is the dielectric susceptibility. The electric field inside the capacitor can be rewritten as

$$E = \frac{(D - P)}{\epsilon_0}. \tag{5.1.3}$$

Using that $\epsilon = \epsilon_p/\epsilon_0$, and combining (5.1.1) through (5.1.3), one obtains the dielectric constant, or DF [81, 82]

$$\epsilon = 1 + \chi = 1 + \frac{P}{\epsilon_0 E}. \tag{5.1.4}$$

As presented earlier, the DF describes how a material will respond while an electromagnetic field is incident on it and consists of an imaginary part and a real part ($\epsilon = \epsilon_1 + i\epsilon_2$), where ϵ_2 is of interest in this thesis as it is proportional to the extinction coefficient k, for approximately constant n. Hence, it is an easy way to calculate the absorption coefficient

$$\alpha = \frac{4\pi k}{\lambda}, \tag{5.1.5}$$

where λ is the wavelength.

It is possible to use a semi-classical approach to describe the interaction between an external electromagnetic field and Bloch electrons in a semiconductor where the electromagnetic field is treated classically and electrons by quantum mechanical wave functions. The approach is not as rigorous as a fully quantum mechanical treatment, but gives the same results [88]. Using a such approach, ϵ_2 can be written as

$$\epsilon_2(\omega) = \frac{1}{4\pi\epsilon_0}\left(\frac{2\pi e}{m\omega}\right)^2 \sum_k |P_{\mathrm{cv}}|^2 \delta(E_c(k) - E_v(k) - \hbar\omega), \tag{5.1.6}$$

where m is the mass of an electron, $\hbar$ is the reduced Plancks constant, P_{cv} is the momentum matrix element for the transition from the VB to CB and $E_c(k)$ and $E_v(k)$ is the energy of the conduction and valence band, respectively. To obtain a result for ϵ_1, the Kronig-Kramer relations in equation (4.4.6) can be used.

Normally, the DF of a sample is not known and hence a modeling of the function is required. The construction of such an optical model is one of the most important steps in the analysis of the data from SE measurements. For semiconductors, these DFs may be complex and have complicated structures. Mathematical inversion is used to find the DF. This is done by using equation (4.4.1) where Ψ and Δ is known to find ρ which can be function of n_0, n_1 and θ_0 for instance where n_1 is unknown in the sample. The optical transition in a semiconductor can be both direct and indirect band gap. In a direct band gap, the transition is direct from the VB to CB without help from phonons, i.e. the maximum in the VB and the minimum in the CB is in the same place in the $\vec{k}$ space, where k represents the momentum of an electron. In the case of an indirect band gap, the positions of $\vec{k}$ differs from the minimum and maximum. A function that helps to describe the DF is the joint density of state $J(E_n)$ which can be written as [88]

$$J(E_{\mathrm{cv}}) = \frac{1}{4\pi^3}\int \frac{\mathrm{d}S_k}{|\nabla_k(E_{\mathrm{cv}})|}, \tag{5.1.7}$$

where E_{cv} is an abbreviation for the energy difference $E_c - E_v$ between the CB and VB, respectively. S_k is the constant energy surface defined as $E_{\mathrm{cv}}(\vec{k}) = \text{const}$.

$J(E_n)$ is the density of paired initial and final states which participates in a transition at a certain photon energy E_n. In a semiconductor, the initial state is the VB and the final state is the CB. A typically shape of the joint density of state function is shown in Figure 5.1, where the optical transition starts at the band gap energy E_g. For higher energies, the joint density of state increase for energy larger than E_g. E_0 in the figure is known as the critical point, also known as Van Hove singularities [88]. This is a point where, in photon energy, the joint density of state function has a singularity and $|\nabla_k(E_{\mathrm{cv}})|$ vanishes in equation (5.1.7). With equation (5.1.7), one can replace

$$\sum_k = \int J(E_{\mathrm{cv}})\mathrm{d}E_{\mathrm{cv}} \tag{5.1.8}$$

in equation (5.1.6).

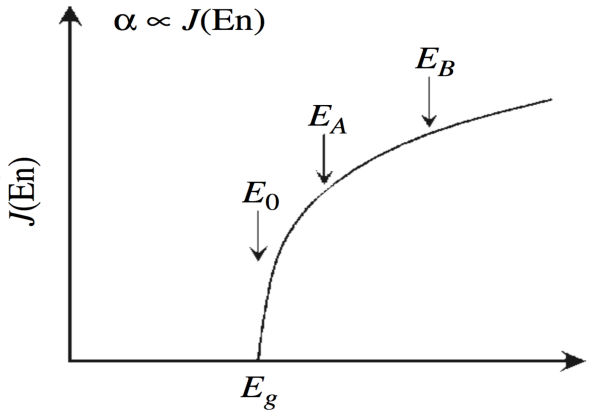

Figure 5.1: Typically joint density of state as function of photon energy. Figure is taken from Ref. [82].

There are mainly four different types of critical points. The first one is M_0 which is the minimum energy between the VB and CB, or the band separation E_{cv}. This is the same as the band gap energy E_g in a direct semiconductor. M_1 and M_2 are known as saddle points due to their energy plots against the wavevector $\vec{k}$ is similar to a saddle. The fourth type of critical point, M_3, represents a maximum in the interband separation. Usually, a graph of ϵ_2 contains a absorption edge, E_0, and two other energy peaks for instance E_1 and E_2. E_1 is often asymmetric and lie above the absorption edge and contains transitions from different directions in the Brillouin zone and E_2 is a strong and absolute maximum peak in the function. This is due to large contributions from a range in the Brillouin zone close to the edges.

5.2 Dielectric Function - Models

In order to analyze the data from SE measurements, the DF must be known. If the DF is not known for the sample, it is necessary to model the function by using different models. To model the DF of semiconductors, each critical point is modeled to account for the optical transitions. Since there are often a lot of critical points in a semiconductor, the DF becomes complicated and modeling the function is hard. To do this, different models for different cases have been developed. In general, 10-50 parameters is usually enough to model the DF for semiconductors [82]. Some of these models will be presented in this section. An illustration of some of the models is shown in Figure 5.2.

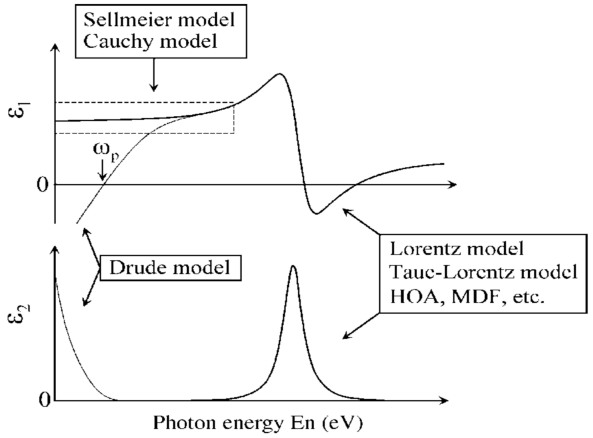

Figure 5.2: Illustrates the different models that is typical used to to model the DF in SE analysis. Figure taken from Ref. [82].

5.2.1 Oscillator Approximation

Oscillator approximation uses different oscillators to account for the different parts of the spectral range in the DF. One problem by using this method is that one often use hypothetical oscillators that necessary not corresponds to a critical point. The different types of oscillators will now be presented.

Lorentz Oscillator

The Lorentz oscillator is based on a classical model and can be seen as a negatively charged electron bound to a positively charged atomic nucleus with a spring between. Assuming that an electric field ($E = E_0 \exp(i\omega t)$) is incident on the sample, it will induce a dielectric polarization in the x-direction where the electron oscillates in a viscous fluid. In addition, it is assumed that the mass of the atomic nucleus is much larger than the electron. Thus, the classical model can be expressed as

$$m_e \frac{\mathrm{d}^2 x}{\mathrm{d}t^2} = -m_e \Gamma \frac{\mathrm{d}x}{\mathrm{d}t} - m_e \omega_0^2 x - eE_0 \exp(i\omega t), \tag{5.2.1}$$

where m_e is the electron mass, e is the charge of the electron, Γ is a proportional constant for the viscous force (damping coefficient), N_e is the number of electrons per unit volume and ω_0 is the resonant frequency of a spring, by applying Newton's second law. On the right hand side, the first term is the viscous force on the fluid, the second term is the how the electron moves according to Hook's law and the last term represents the electrostatic force from an electric field.

One assumption is that the electron oscillates in the same manner as the electric field varies, i.e. $x(t)$ varies as $x(t) = a\exp(i\omega t)$. Using $x(t)$ in (5.2.1), rearranging and setting into equation (5.1.4) one obtains

$$\epsilon = 1 + \frac{e^2 N_e}{\epsilon_0 m_e} \frac{1}{(\omega_0^2 - \omega^2) + i\Gamma\omega}. \tag{5.2.2}$$

Equation (5.2.2) can further be divided into a real and a complex part resulting into

$$\epsilon_1 = 1 + \frac{e^2 N_e}{\epsilon_0 m_e} \frac{(\omega_0^2 - \omega^2)}{(\omega_0^2 - \omega^2)^2 + \Gamma^2 \omega^2}, \quad \epsilon_2 = \frac{e^2 N_e}{\epsilon_0 m_e} \frac{\Gamma \omega}{(\omega_0^2 - \omega^2)^2 + \Gamma^2 \omega^2}. \tag{5.2.3}$$

By looking at the equation for ϵ_2, one can see that ω_0 will represents the maximum value and Γ becomes the half width. ω is proportional related to the photon energy E_n and hence the Lorentz oscillator can be expressed as

$$\epsilon = 1 + \sum_j \frac{A_j}{E_{n0j}^2 - En^2 + i\Gamma_j E_n}, \tag{5.2.4}$$

where E_{n0j} is the oscillator placement energy, j is the subscript for the j'th oscillator term and A_j is the oscillator strength. The Lorentz oscillator is only valid for energies significantly lower than the band gap energy.

Tauc-Lorentz and Cody-Lorentz

The Tauc-Lorentz and Cody-Lorentz oscillators both uses a broad Lorentzian line shape with zero absorption below a defined band gap to account for the main absorption for amorphous materials. The Tauc-Lorentz oscillator was first introduced by Modine et. al. [89] in 1996. In the Lorentz oscillator, the function for ϵ_2 peaks at ω_0 and is symmetric. For amorphous materials this is not the case and generally such types of materials shows an asymmetric behavior. Therefore, the Tauc-Lorentz oscillator is a product of the unique band gap and the Lorentz oscillator. The DF behavior above the band gap is given by the Tauc band gap, given as [82]

$$\epsilon_2 = A_{\text{Tauc}} \frac{(E_n - E_g)^2}{E_n^2}. \tag{5.2.5}$$

To obtain the final results for ϵ_2, equation (5.2.5) is multiplied with equation (5.2.4) and one obtains

$$\epsilon_2 = \begin{cases} \frac{AE_{n0}C(E_n - Eg)^2}{(E_n^2 - E_{n0}^2)^2 + C^2 E_n^2} \frac{1}{E_n}, & (E_n > E_g) \\ 0 & (E_n \leq E_g) \end{cases} \tag{5.2.6}$$

where A represents the amplitude and C the half width of the function. To derive the expression for ϵ_1, one can use the Kramers-Kronig relations. An example of such oscillator is shown in Figure 5.3 with $E_g = 1.1$ and $E_n = 3.5$.

The Cody-Lorentz oscillator was developed by Ferlauto et. al. [90] in 2002. It is similar to the Tauc-Lorentz oscillator in the sense that they both defines a band gap energy E_g and a Lorentzian absorption peak. The difference is that for above the band gap, $\epsilon_2 \propto (E_n - E_g)^2$ instead of $\epsilon_2 \propto (E_n - E_g)^2/E_n^2$ as for the Tauc-Lorentz oscillator. In addition, Cody-Lorentz oscillator defines two new transitions energies, E_p and E_t in the model. E_p is the energy at where absorption transistions goes from Lorentzian to Cody behavior, while E_t is the energy where the absorption transitions goes from Cody to Urbach behavior. The Urbach behavior, or tail, will be presented in a following section. The Cody-Lorentz oscillator has also a parameter E_u which is the exponential decay rate for the model. An example of a Cody-Lorentz oscillator is shown in Figure 5.4 with details of E_t, Urbach transitions regions and other different parameters.

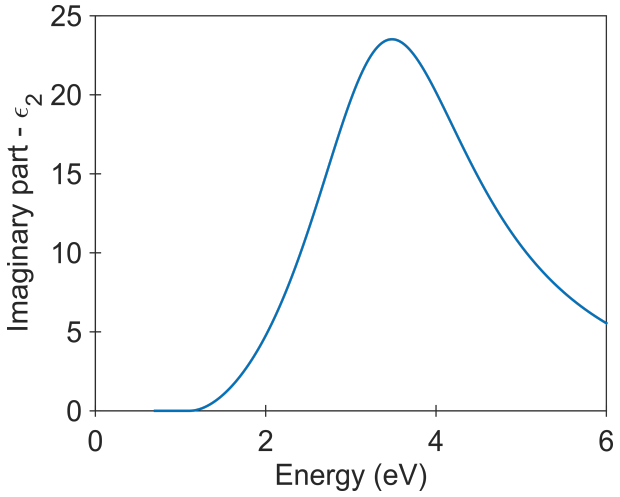

Figure 5.3: An example of the Tauc-Lorentz oscillator for amorphous silicon material with $Eg = 1.1$ eV and $E_n = 3.5$ eV.

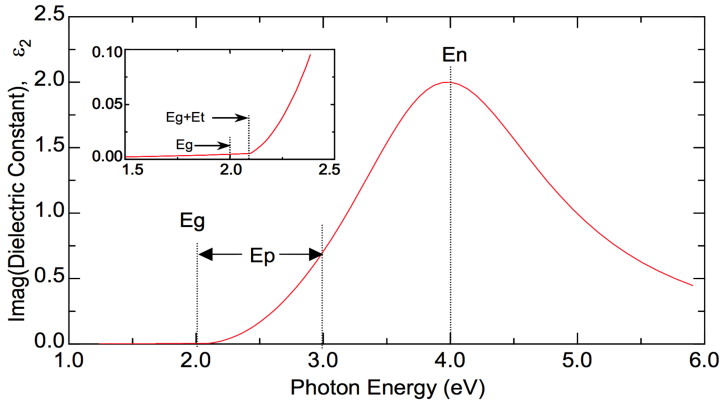

Figure 5.4: Example of a Cody-Lorentz oscillator with details of E_t and urbach transitions regions. Figure is taken from Ref. [81].

Gaussian

There is a Gaussian oscillator type defined as [87]

$$\epsilon_{\mathrm{G}} = A\left[\left(\Gamma\left(\frac{E-E_n}{\sigma}\right)+\Gamma\left(\frac{E+E_n}{\sigma}\right)\right)+i\left(\exp\left(-\left(\frac{E-E_n}{\sigma}\right)^2\right)+\exp\left(-\left(\frac{E+E_n}{\sigma}\right)^2\right)\right)\right], \tag{5.2.7}$$

where σ is defined as

$$\sigma = \frac{B_r}{2\sqrt{\ln(2)}}. \tag{5.2.8}$$

In these two equations A is the amplitude, E_n is the center energy and B_r is the broadening. To produce a Kramers-Kronig consistent line shape for ϵ_1, a convergence series is defined as the function Γ. The interesting part of equation (5.2.7) is the imaginary part, as this is the part that affect ϵ_2. At the center energy E_n, A is equal ϵ_2. While σ is defined as in equation (5.2.8), B_r is approximately equal the full width at half maximum value (FWHM). The difference between a Gaussian oscillator and Lorentz oscillator may be seen in Figure 5.5. As one can see, the imaginary part of the DF rapidly approaches zero beyond the FWHM, while the Lorentz oscillator is more tailing.

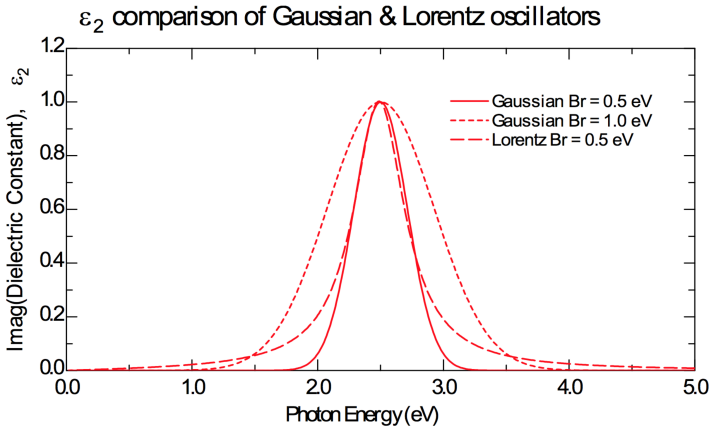

Figure 5.5: Comparison between the Gaussian oscillator and the Lorentz oscillator. Figure is taken from Ref. [81].

Drude Oscillator

The Drude oscillator is used to describe free carriers effects in the DF. It is basically a Lorentz oscillator placed at zero energy (0 eV). In the software CompleteEASE there are two different Drude oscillators. The first one is defined as [87]

$$\epsilon_{\text{Drude}} = \frac{-\hbar^2}{\epsilon_0 \rho_n (\tau_n E^2 + i\hbar E)}, \tag{5.2.9}$$

with

$$\rho = \frac{1}{q\mu N}. \tag{5.2.10}$$

$\hbar$ is the reduced Planck constant, ϵ_0 is the vacuum dielectric constant, ρ is the resistivity, τ is the scattering time in femto seconds, q is the electron charge, N is the carrier concentration and n is the nth oscillator. The fit parameters here are ρ and τ. The second Drude oscillator is given by [87]

$$\epsilon_{\text{Drude}} = \frac{-\hbar^2 q^2 N_n \mu_n}{\epsilon_0 (\mu_n m^* m_e E^2 + iq\hbar E)}, \tag{5.2.11}$$

where m^* is the carrier effective mass, m_e is the electron rest mass and the other parameters as given above. In this thesis, the Drude oscillator, given by equation (5.2.9), is used since ρ was known for some of the samples.

5.2.2 B-spline

The B-spline model in the software (CompleteEASE) [87] is not a physical model for the DF. Instead, it uses a series of control points that are equally spaced in photon energies in eV. B-spline is used to obtain the DF versus wavelength, or photon energy. The curves are smooth in zeroth, first and second derivatives, i.e. they are by definition smooth and continuous, and interpolate the DF between each of the control points. Using shorter spacing between each control point, increase the resolution and the model is more flexible to define sharper features in the DF. If the resolution is set too low, noise and unphysical

artifacts could arise in the DF. An advantage of using B-spline model is that if one property in the UV is changed, the change will not affect the DF in the near infrared for instance due to the control points. Another advantage is that the Kramer-Kroing (KK) relations can be used to generate KK consistent functions, i.e. change in ϵ_1 will also change ϵ_2. To help the model, a starting material can be set as a starting point to help the program to fit the model to experimental values.

5.2.3 Cauchy Layer

To determine the optical properties for transparent, or partially transparent materials, the Cauchy layer from the library in the software CompleteEASE [87] can be used. The Cauchy layer is good for dielectrics and semiconductors below the band gap where little absorption takes place ($\epsilon_2 \approx 0$). In this part of the spectral range, the optical constants can be represented as a slowly varying function of wavelength with an exponential Urbach tail absorption just below the band gap. The refractive index of the layer is given by an inverse power series with only even terms. given by

$$n(\lambda) = A + \frac{B}{\lambda^2} + \frac{C}{\lambda^4}, \tag{5.2.12}$$

where λ is the wavelength and A, B and C are the variable fit parameters that determines the refractive index n. In addition, there is a term for the extinction coefficient to describe an Urbach tail absorption, given by

$$k = K \exp\left(D(E - E_g)\right), \tag{5.2.13}$$

where K is the amplitude, E is the energy, D is a fit parameter to determine the shape of the exponential and E_g is the band gap energy which can be set manually, but is not a fit parameter as it is correlated to the amplitude K. For the Cauchy layer to be a physical model, the refractive index must increase towards higher energies, i.e. for lower λ. An example for the optical constants is given in Figure 5.6, with $A = 1.45$, $B = 0.01$ and $C = 0$.

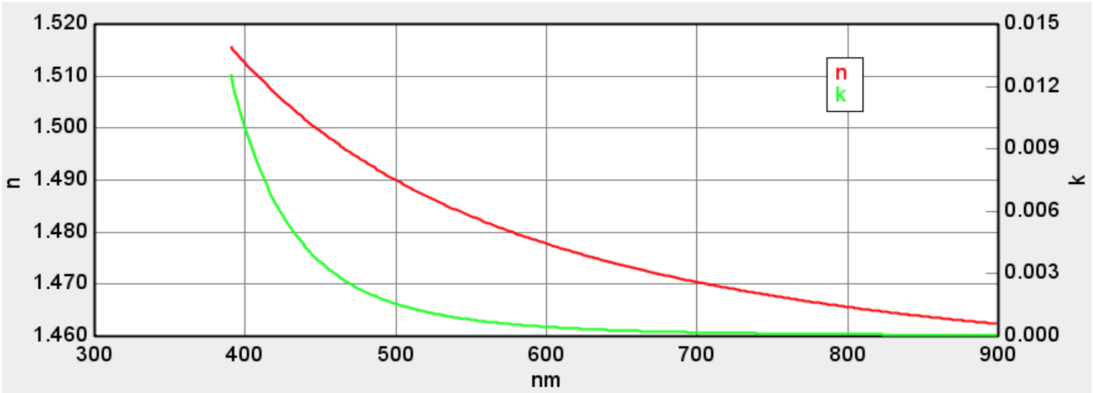

Figure 5.6: Example of the optical constants for a Cauchy layer with $A = 1.45$, $B = 0.01$ and $C = 0$. Figure is taken from Ref. [87].

5.2.4 Effective Medium Approximation

For all SE measurements, the surface and interface structures affects the sensitivity of the measurements and thereby the results. The effective medium approximation (EMA) [82, 83] consists of different models for calculations of the DF in a sample with a mixture of two or three composites. There is possible to find the volume fraction of the different composites in the materials, in addition. To apply one of the EMA models, some conditions must be satisfied. The first one is that the sizes of structures of different dielectric functions in the matrix material is sufficiently greater than the atom sizes, but smaller than $\lambda/10$ of the wavelength. The second condition is that the DF is independent of size and shape. The simplest EMA model is to linearly interpolate between the constituent of the DF given as [81]

$$\epsilon = f_a\epsilon_a + f_b\epsilon_b, \tag{5.2.14}$$

where ϵ is the effective complex dielectric function of the mixture, f_a and f_b are the volume fractions of the each composite of the materials, and ϵ_a and ϵ_b are the complex dielectric function of each composite of the material. It is not very accurate, but reduce the computational time significantly and is often used in graded layers.

Another model is the Lorentz-Lorenz relation expressed as [82]

$$\frac{\epsilon - 1}{\epsilon + 2} = f_a\frac{\epsilon_a - 1}{\epsilon_a + 2} + (1 - f_a)\frac{\epsilon_b - 1}{\epsilon_b + 2}, \tag{5.2.15}$$

with the same meaning of the variables as for the linear case. It is assumed that the surrounding medium is air. $(1 - f_a)$ represents here the volume fraction of the composite b of the material.

A third model is the Bruggeman EMA, given as [81]

$$f_a\frac{\epsilon_a - \epsilon}{\epsilon_a + 2\epsilon} + (1 - f_a)\frac{\epsilon_b - \epsilon}{\epsilon_b + 2\epsilon} = 0. \tag{5.2.16}$$

The variables have the same meaning as above. More EMA models exist, but is outside the scope of this thesis.

EMA theory is an effective way to calculate the DF in the surface roughness layer. One example of a such model is shown in Figure 5.7, where the roughness of a sample structure is shown leftmost. Rightmost, the roughness is replaced by a surface roughness layer with optical constants N_1. It is possible to use the EMA models to estimate the DF in the layer where d is the thickness of the layer and f_{void} is the volume fraction. f_{void} is possible to set to be fixed, most typically 0.5, or could be one of the analytically fit parameters. Thus it is possible to set $\epsilon_a = N_1^2$, $\epsilon_b = N_2^2$ and $f_a = f_{\text{void}} = 0.5$ in one of the equation above and get the dielectric function of the roughness layer and thickness.

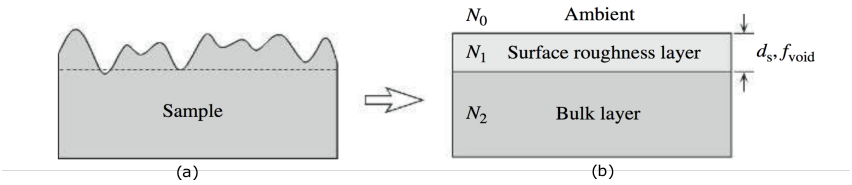

Figure 5.7: Example of how EMA converts the roughness of the top of the sample to a surface roughness layer with a thickness d_s and a volume fraction f_{void}, typically set to 0.5. Figure is taken from Ref. [82].

There are some limitations for EMAs. For instance, it is difficult to use this theory on calculations of the DFs of semiconductor alloys. Another problem arises if the morphology is larger than $\lambda/10$. Thus, it will be difficult to characterize the surface roughness. In addition, it is difficult to characterize if there is a two-dimensional island growth on the substrate. Finally, transparent films have small n which make them more difficult to evaluate at the surface.

5.3 Urbach Tail

The Urbach tail, or edge/energy, was first introduced by F. Urbach [91] in 1953, often associated with the transitions from VB to CB in disordered materials. It is an empirical rule for the absorption coefficient proportional to [92]

$$\alpha(E) = \alpha_0 \exp\left(\frac{E - E_a}{E_0}\right), \tag{5.3.1}$$

where E is the photon energy, E_a and α_0 are constants and E_0 is the Urbach tail width. E_0 is expected to be a function of the disorder in the material. Many studies the last decades indicates the Urbach tail is a behavior that is nearly universal for all disordered solids, there among semiconductors and glasses [93]. The Urbach tail affecst the DF in the sense that the band gap have an exponential shape instead for an abrupt change in the band gap region. It is experimentally found that in amorphous semiconductors films, the Urbach tails arises as a result of the VB tail and it hence roughly represents the VB width. In addition, it is found that there is a correlation between the stress and the structural disorder in the solid [94], resulting in an increase in the Urbach tail when the stress increases in the solid. This means that in heavily doped materials, the Urbach tail increases due to the disorder in the material.

5.4 Excitons

Another property observed in the DF is the excitons in semiconductors and other solids [95, 96]. Excitons are quasi-particles and are electron-hole pairs that are bound into pair states. An ideal exciton is electrically neutral and is a transport of energy instead of charge. Since the electron-hole pairs are not bound to any ion, but pass from one ion to the next, excitons can be seen as free particles and hence transport energy in the periodic structure of a crystal. The reason for these bound states to exist is due to the attracted force from the Coulombe potential $\frac{-e^2}{\epsilon r}$, where e is the is the charge of the electron or hole, r is the distance between and ϵ the dielectric constant. Excitons have many properties

analogues to hydrogen atoms where the hole corresponds to the positive proton. For hydrogen atoms, $\epsilon = 1$ in free space, but for other solids ϵ may be much larger and reduce the potential energy due to this coupling between the electrons and holes. This behavior should take place on an uniquely energy, but due to lattice vibration this energy can spread over a larger range of allowed bands. For small temperatures, clearly excition peaks can be seen, but they broadens with increase of temperature. As a result of excitons, the energy band structure in the semiconductors is complicated. Excitons often appears in the absorption, and therefore they can be of interest in this thesis as they may affect the DF.

5.5 Polarons

Strong interaction between electrons and phonons in transition metals have been of huge interest [97] since the concept was first presented by Landau in 1933 [98]. The strong interaction causes a potential well and binds the electron [99] which are surrounded by a cloud of phonons [100]. Such clouds have complex dynamical nature and affects the position of the electron and the lattice deformation. The effective mass of the trapped electron becomes much heavier than of an isolated electron in free space, but since it has almost the same behavior as an electron in free space it is transformed into a quasiparticle with the name polaron. It is the electron interacting with phonon from a vibrating ion in the lattice. There are two types of polarons; large polarons and small polarons. Large polarons could be extended largely while the small polarons often self trap themselves in small spaces [100]. The polarons behaves as negatively charged particles and can often be seen in semiconductors and polymers. The process happen even though the material has a perfect crystal lattice. Since phonons occurs for low photon energies, an absorption peak could be observed in the imaginary part of the DF and affect the function at low photon energies.

Chapter 6

Results and Discussion

In this chapter, the results will be presented and discussed. First, a section will compare how Ψ and Δ change with and without use of focus probes during the SE measurements. Next, a section show how the transmittance measurements with a spectroscopic ellipsometer looks like and compare with the transmittance measured elsewhere(Figure 4.9). Thereafter, the road towards the final model for the dielectric function will be described, with descriptions of different models developed during the work. Next, the final model and the oscillator layer is presented. Thereafter, the results and discussions for the two spin coating series (SC-series) and the two PLD series will be presented. The last section in the chapter contains a comparison and discussion, where features found in all samples will be presented and compared to each other and how they changed with the method of deposition.

6.1 Comparison of Ψ and Δ with and without Focus Probes

As presented in section 4.4.2, the SE measurements were performed both with and without the focus probes. Figure 6.1 shows how Ψ and Δ changed with (solid lines) and without (dashed lines) use of focus probes for two samples P-Q-200/85, (a) and (b), P-Q-570/55, (c) and (d) for two angles of incidence. As seen from the figure, there is not a huge difference between the measurements with and without the use of focus probes for sample P-Q-200/85. The small differences that are seen could be due to different positions of the beam, since the measurements were performed at different occasions. For sample P-Q-570/55 there are huge differences between the measurements with and without focus probes. In Figure 6.2, Ψ an Δ for the measurements for two samples from the spin coating (SC) series, SC-C05-350, (a) and (b), and SC-C01-350, (c) and (d), are shown. The other samples showed similar trends as for the results plotted in Figure 6.1 and 6.2: Small differences, with and without focus probes for the SC series, and large difference for the PLD series, especially for high growth temperature.

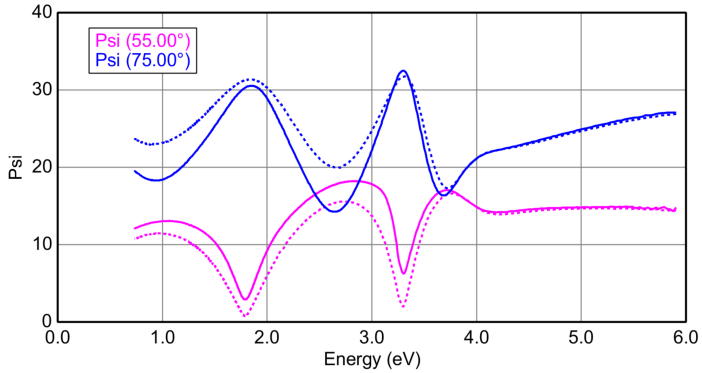

(a)

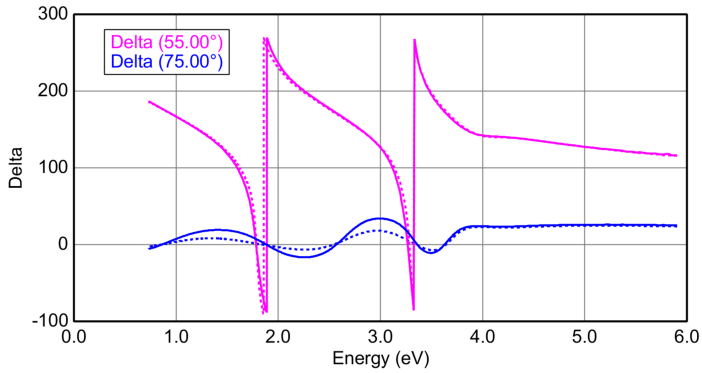

(b)

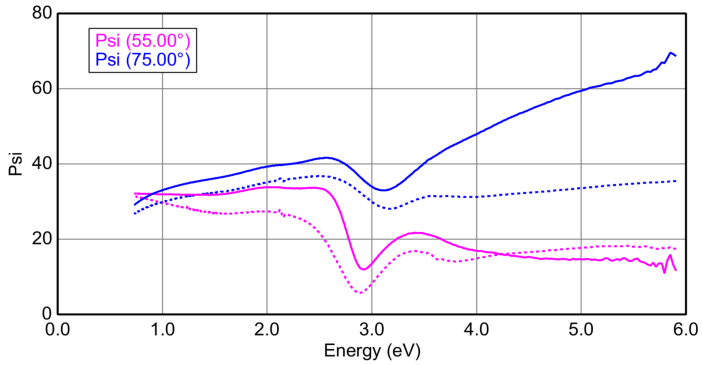

(c)

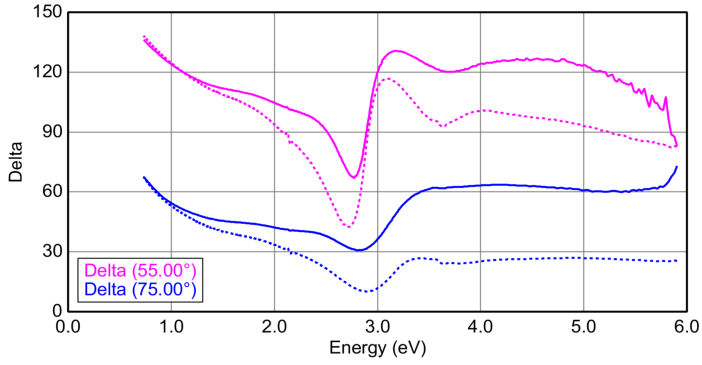

(d)

Figure 6.1: Ψ and Δ with (solid lines) and without (dashed lines) focus probes for sample P-Q-200/85, (a) and (b), and for sample P-Q-570/55 (c) and (d), for two angles of incidence: 55° (magneta lines) and 75° (blue lines).

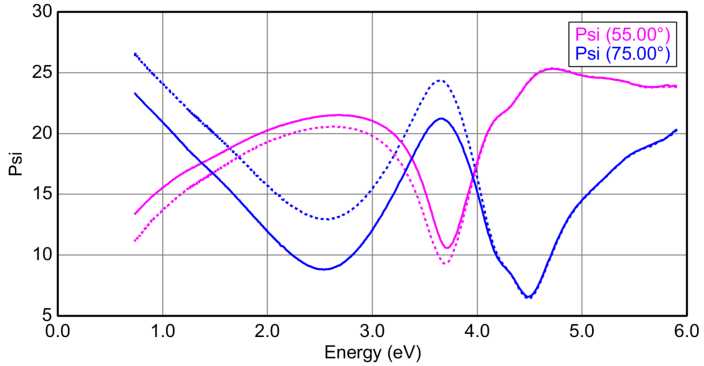

(a)

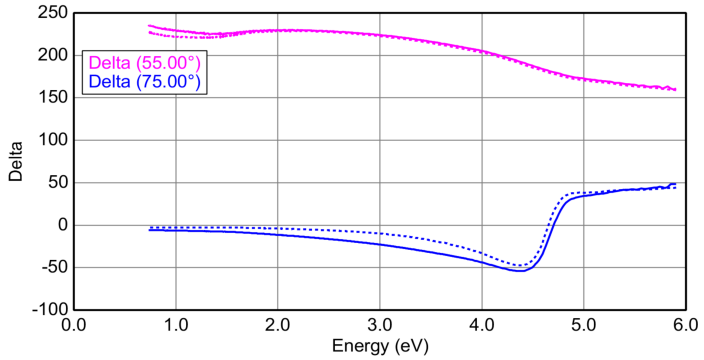

(b)

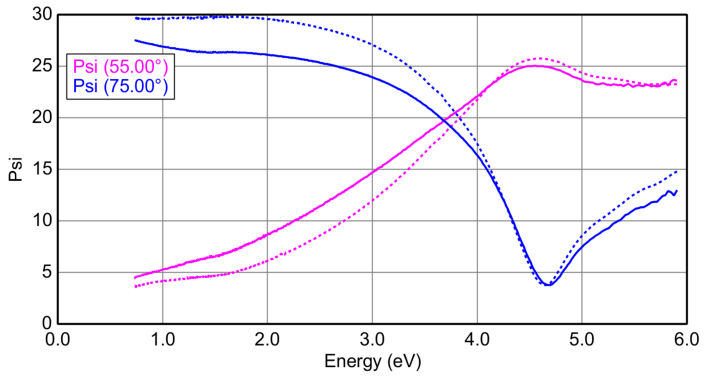

(c)

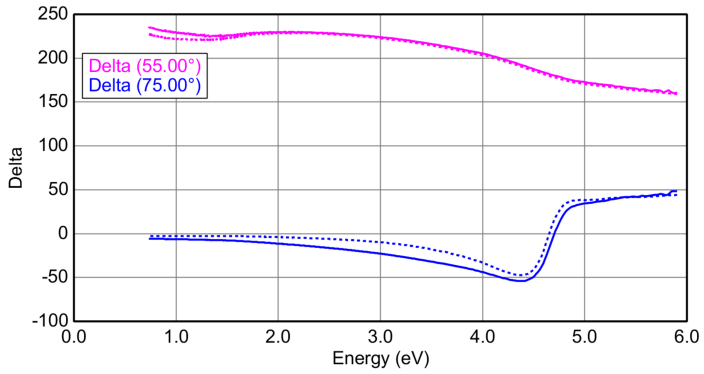

(d)

Figure 6.2: Ψ and Δ with (solid lines) and without (dashed lines) focus probes for sample SC-C05-350, (a) and (b), and for sample SC-C01-350 (c) and (d), for two angles of incidence: 55° (magneta lines) and 75° (blue lines).

As seen from Figure 6.1, it is for higher photon energies the largest difference occurs, especially for P-Q-570/55 in (c) and (d). As seen in the SEM pictures in Figure 4.8 (d) for P-Si-570/55, there are large variations across the sample with some higher "islands" in the back. The same is observed for P-Si-500/70 as can be seen from the same figure. Even though the SEM pictures are for Si substrates, one can assume there will be similar variation for the quartz substrates. A reason to the difference could be due to the wavelength for the high photon energies, where the wavelengths have the same magnitude as the morphology. If so, it would be more difficult to make good models due to many different structures is measured in parallel if one not use focus probes. Another reason to the difference could be that the SC-series and the low growth temperature series have more uniform surface roughness than the high growth temperature series. Based on result found from these comparisons, it was decided to use measurements without focus probes for the SC-series and the low growth temperature series from PLD, while the focus probes results was used for the high growth temperature series that will be presented later in this chapter.

6.2 Transmittance Measurements

A feature with the spectroscopic ellipsometer used in this thesis, the RC2 Model XI ellipsometer provided by J. A. Woollam Co., is that it is possible to measure the transmittance for the samples. Quartz is a transparent material, so the substrate should not absorb the incident light. Since silicon absorbs much of the incident light it does not make any sense to measure the transmittance on samples with silicon substrates. Figure 6.3 shows the measured transmittance of the series with low growth temperature from PLD (solid lines) while dashed lines is the reference measured elsewhere (Figure 4.9). If one compares the transmittance measurements one can see they are approximately equal, excepts for P-Q-200/95 which is measured to have a higher transmittance with the SE than the reference. However, the transmittance measured with SE seems more reasonable because P-Q-200/95 had more oxygen available during the deposition. As a result, one would expect the sample to be less reduced than P-Q-200/85 and therefore be more transparent since MoO_3 is transparent for low photon energies. The dip just before 1400 nm is shown in both the transmittance measured with the SE and the reference, and could be a feature either in the substrate, or in the air. Since transmittance measurements performed with the spectroscopic ellipsometer are approximate equal to the reference, except P-Q-200/95, the results should be reliable and can be used in the modeling of the DF for the reduced MoO_{3-x} presented in the later sections.

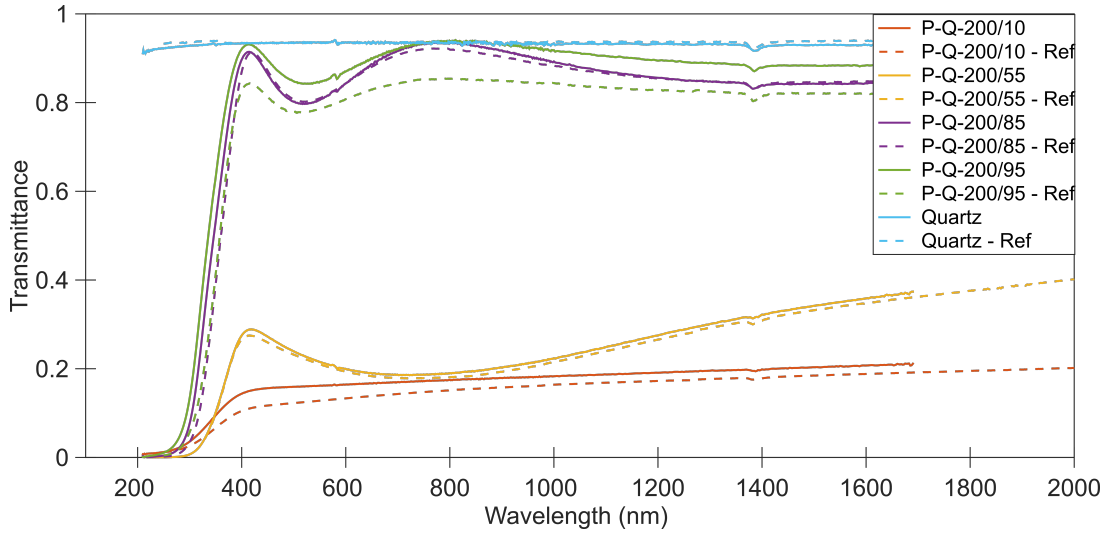

Figure 6.3: Transmittance measurement performed with the spectroscopic ellipsometer (solid lines) for the samples on quartz for the samples with low growth temperature from PLD given in Table 4.1. Dashed lines is the reference measured elsewhere (Figure 4.9).

6.3 The Development of the Model

In this section, the development of the model used to extract the DF is presented briefly in a chronological order. Therefore, there could be some places in the text where there are jumps between which series that are examined. Only the most important figures and tables will be shown.

Firstly, the DF for the quartz substrate was obtained for all series: The DF was obtained by using a Cauchy layer, as described in section 5.2.3, since quartz is a transparent material. It was assumed all quartz substrates in the series had an identical DF as the bare quartz sample. This will give a more correct model instead of use the DF for quartz in the library in the software. The DF may change from sample to sample even though all are quartz. In the beginning, an approximate thickness and surface roughness were available, an the hope was to model the DF without any other information. A normal way to start to model the DF is to use a Cauchy layer in the transparent region for the material. As presented in section 4.1, the least reduced samples, containing mostly MoO_3, were assumed to be transparent below approximately 3 eV. The Cauchy layer is used to determine the thickness of the film and the roughness layer (RL). Thereafter, one can use the B-spline model, presented in section 5.2.2, with starting values from the transparent region, and expand to the rest of the spectral range for the spectroscopic ellipsometer. The DF is modeled point for point with an interval of 0.2 eV between each point with the thickness of the film and RL fixed and only varying the DF. While a good MSE is obtained in the B-spline model, the next step is to parameterize the DF extracted from the B-spline with the different oscillator models presented in section 5.2.1.

The surface roughness of the SC-series were assumed to be small compared to the PLD samples and therefore it should be easier to make a good model. As described in section 4.1.1, MoO_3 can be regarded as a transparent medium for low photon energies and a Cauchy layer will describe the DF of the material in the transparent region. Therefore, the first thing was to use a Cauchy layer for energies below the band gap to see whether this was a good model. The model was in good agreement both with thickness and the Cauchy dispersion for the sample with no post-treatment and the one with 200 °C post-treatment temperature in hydrogen environment. These two samples were assumed to be least reduced and therefore most transparent.

After finding thicknesses and RL thickness from using the Cauchy layer, the next step in the modeling development was to replace the Cauchy layer with the B-spline. One of the first results is shown Figure 6.4. As shown in the figure, there is absorption ($\epsilon_2 > 0$) below the band gap energy, in a "tail" (red arrow), and a clear top around 1 eV (blue arrow). Actually, no transparent region was seen and is one reason why a Cauchy layer did not work at all for this sample. The B-spline was used to parameterize the DF by using different oscillator models. Since this thesis was based on Benjamin Roaldssønn Hope master thesis [9] from 2015, the first model was similar to the chromium doped ZnS samples. He used a Cody-Lorentz (C-L) and a Tauc-Lorentz (T-L) oscillator to account for the absorption edge and above the band gap. For a peak around 5.5 eV, a T-L oscillator was used. In addition, he used a Gaussian oscillator for higher energy to account for contributions from states immediately outside the upper measurement range. A Lorentz oscillator was used below the band gap to account for increased absorption due to the chromium. An illustration for contribution for each of these oscillators is shown in Figure

6.5, where the light blue line is the total ϵ_2. Therefore, the first model consisted of a T-L and a C-L for the band edge and above, and a Gaussian to account for the absorption observed around 1 eV in Figure 6.4. A Gaussian was used instead of the Lorentz oscillator as the tail from the Gaussian decays faster towards zero, and not affect ϵ_2 above the band gap. One important comment is that no surface roughness was taken into account since it was assumed to be very small due to the fabrication technique.

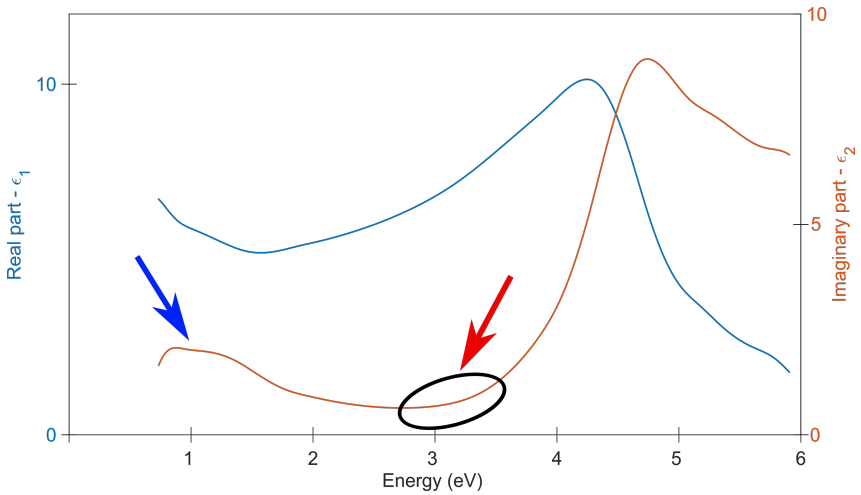

Figure 6.4: First results for sample SC-C01-300 with B-spline without RL, where the blue line is ϵ_1 and the orange line is ϵ_2.

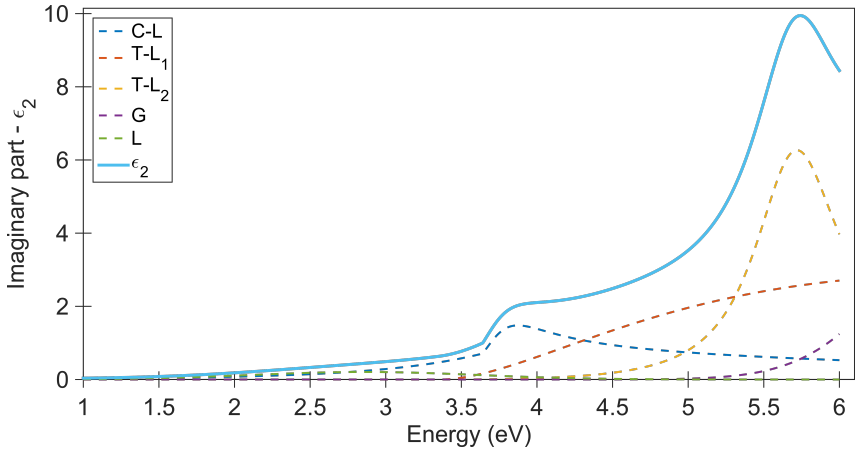

Figure 6.5: Illustration of the contribution from each oscillator for chromium doped ZnS from Hope's master thesis [9], where the green line is the total ϵ_2.

The second model contained the same oscillators, with one additional Gaussian for low energies, i.e. two Gaussians in total, as there was reported in [54] that the absorption around 1 eV could be deconvoluted into two Gaussians. An example of each contribution from the oscillators is shown in Figure 6.6. These models gave good MSE for the series and reasonable thicknesses around 10 nm, as one can see in Table 6.1, except for SC-C01-450 which was found to be twice as thick. Another thing to note is that the contribution from the C-L oscillator (dashed blue line in Figure 6.6) kept increasing after the band gap maximum which seems unphysical. Therefore, Hope's model was changed with a new model (model 3): Instead of using both a C-L and a T-L oscillator, the T-L oscillator was replaced with a Gaussian to account for absorption for high energies, as for ZnS in Hope's thesis. The thicknesses were reasonable around 10 nm (Table 6.1) and with good

MSE between 5.1 to 11. Figure 6.7 shows the results for the spin coating series with a concentration of 0.1 Mo cation per liter, the SC-C01 series, for the real and imaginary part of the DF in (a) and (b) respectively. In (c), an example for the contribution from each oscillator may be found. Figure 6.8 shows the results for spin coating series with a concentration of 0.5 Mo cation per liter, the SC-C05 series. One thing to note is that the thickness for the latter samples were found to be around 70 nm instead of 60 nm which was measured with a profilometry elsewhere [48], as seen in Table 6.2.

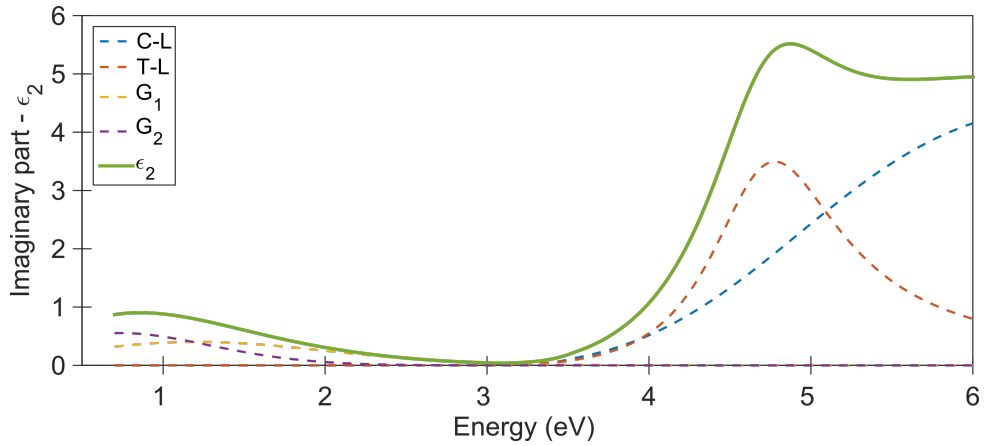

Figure 6.6: An example of the contribution from each oscillator in model 2 with a C-L, T-L and two Gaussians.

Table 6.1: Thicknesses for the SC-C01 series for model 1, 2 and 3 in nm.

Sample	Model 1	Model 2	Model 3
SC-C01-NT	10.7	12.0	11.4
SC-C01-200	10.6	12.3	11.1
SC-C01-300	12.6	11.5	12.0
SC-C01-350	11.4	10.8	10.5
SC-C01-400	11.4	11.3	12.7
SC-C01-450	19.4	20.5	20.2

Table 6.2: Thicknesses for the SC-C05-series for model 1, 2 and 3 in nm.

Sample	Model 1	Model 2	Model 3
SC-C05-NT	73.7	73.8	75.5
SC-C05-200	66.7	67.4	66.8
SC-C05-300	70.1	70.6	71.1
SC-C05-350	69.5	69.5	70.1
SC-C05-400	70.6	70.5	70.4
SC-C05-450	72.9	63.2	66.2

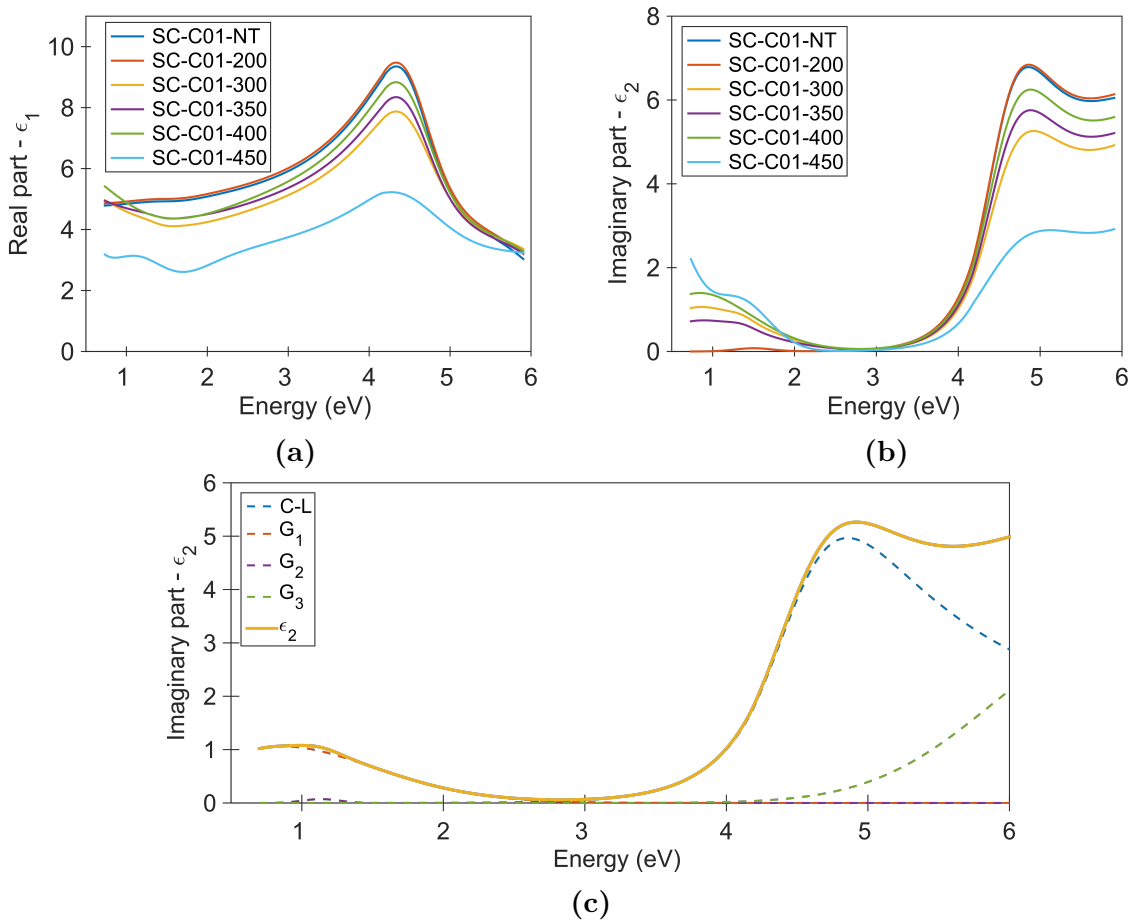

Figure 6.7: (a) The real part of the DF for the SC-C01 series obtained using model 3 with a C-L and three Gaussians. (b) As (a), but for the imaginary part of the DF. (c) The contribution from each oscillator for sample SC-C01-300.

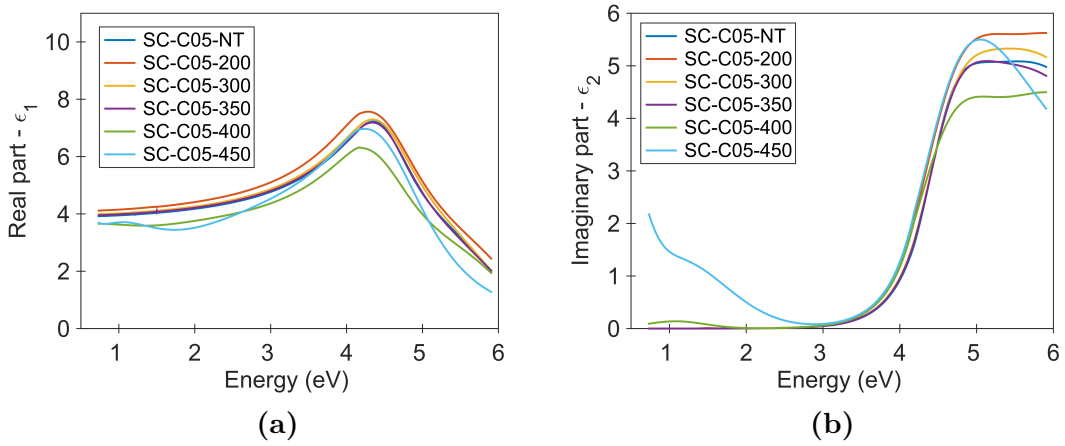

Figure 6.8: (a) The real part of the DF for the SC-C05 series obtained using model 3 with a C-L and three Gaussians. (b) As (a), but for the imaginary part of the DF.

In addition, a multi sample analysis (MSA) was performed for the 10 nm samples, in addition. The results are shown in Figure 6.9. The thicknesses varied around 9 nm. For all results in Figure 6.7 to 6.9, the transmittance measurements was a part of the data and the band gap energy $E_g = 3.0$ eV was fixed to reduce the numbers of fit parameters.

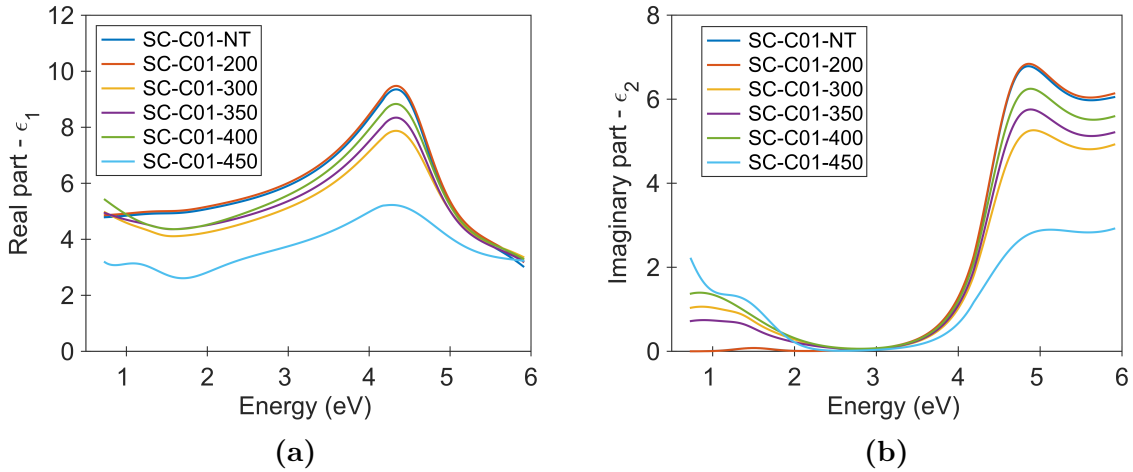

Figure 6.9: (a) The real part of the DF obtained for the SC-C01 series using model 3 with a C-L and three Gaussians, in a MSA. (b) As (a), but for the imaginary part of the DF.

One important feature for ϵ_2 in Figure 6.7 to 6.9 is the peak around 1 eV for the samples that were most reduced. SC-C01-NT and SC-C01-200 did not show any significant contribution at low energies, shown as dark blue and red lines in the Figure 6.7 to 6.9 (b). For SC-C01-450 and SC-C05-450 in Figure 6.7 and 6.8, respectively, ϵ_2 did not decline towards zero for lower photon energies, but increased instead. This indicated there could be free carriers present in these two samples. Hence, the next model was the same as above, but with a Drude oscillator (presented in section 5.2.1) in addition. This decreased the MSE and matched the experimental data from the SE measurements better (not shown). However, in the models presented up to now, the surface roughness had not been taken into account and the next step was to do exactly that.

There are different ways to model the surface roughness. The most common is to use an effective medium approximation (EMA), usually the Bruggeman EMA, given in equation (5.2.16). On the SC-series, listed in Table 4.4, two different models were tested with an EMA layer coupled to a B-spline layer. A coupled EMA layer uses the DF from a layer specified by the user, the B-spline in this case, to adjust the DF in the roughness layer (RL). Both the oscillator layer and EMA layer thickness were fixed in the first attempt. Up to this point, no other information about the samples was used, except the approximate thicknesses. Now, for the SC-series the root-mean-square (RMS) roughness, as presented in section 4.3.2, were set to be the EMA thicknesses. The oscillator layer thickness was set so that the total thickness added up to 10 nm in total. In the second model taking roughness into account, both thicknesses were allowed to vary to obtain the best fit to the experimental results. The results of the imaginary part of the DF are shown in Figure 6.10 where the thicknesses were held constant in (a) and were varied in (b). The thicknesses found from the varying model were reasonable and had good MSE values (not shown), but after consulting with the supervisors, it was concluded that the SC-C01 series could be too thin to establish a good oscillator layer.

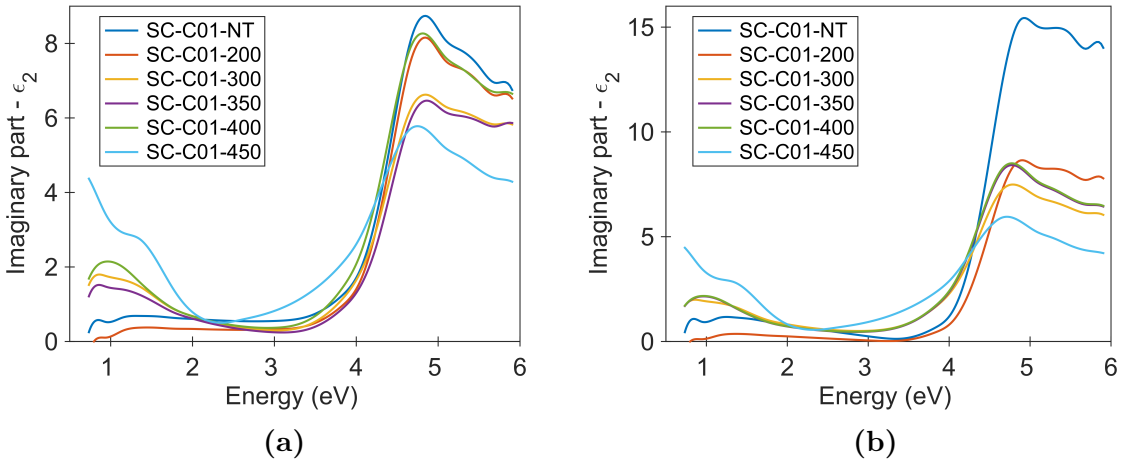

Figure 6.10: (a) The imaginary part of the DF, ϵ_2, for the SC-C01 series for fixed thickness to model the surface roughness. (b) as (a), but for varying thicknesses.

Therefore, the same procedure as for the thin samples was performed on the thicker samples from the PLD series for low and high growth temperatures, found in Table 4.1 and Table 4.2. Firstly, a Cauchy layer for low photon energies was used, and then expanded with a B-spline for the whole spectral range, like for the SC samples. From the SEM pictures in Figure 4.7, it is seen that, especially in (c), there are large grass like columnar rods, which indicates that a lot of void were present in the samples. Therefore, it was necessary to make a yet another model for such type of samples. The first attempt was to use a Bruggeman EMA layer with 50/50 percentage of void and the oscillator layer as for the SC-series. In the first model, the materials were modeled as B-splines with a coupled EMA layer to it. A coupled EMA layer uses the DF from a layer specified by the user, the B-spline in this case, to adjust the DF in the roughness layer (RL), as earlier. Some of the results are shown in Figure 6.11, where the thicknesses were held fixed, (a) and (c), or were fitted by the software, (b) and (d), for quartz and silicon substrates respectively. These results did not give any good MSE and further model development was still needed.

To understand how the EMA-layer responded with varying the thickness and the percentage of void in the layer, a simulation was performed on sample SC-C01-300. The model used here was a B-spline layer coupled to an EMA-layer. At all time the sum of the two layer thicknesses were summed to 10 nm. The simulation results are shown in Figure 6.12, where the percentages of void present varied from 0 % to 100 % with fixed thickness of both the B-spline and the EMA-layer in (a). Each of the layers was set to be 5 nm thick. In (b), the EMA-thicknesses varied, but both layers summed to 10nm in total. As one can see, both for increase of EMA-layer thickness and percentages of void present, the magnitude of ϵ_2 increased. An increase in ϵ_2 seemed reasonable as the oscillator layer needs to absorb more while more void is present in the sample.

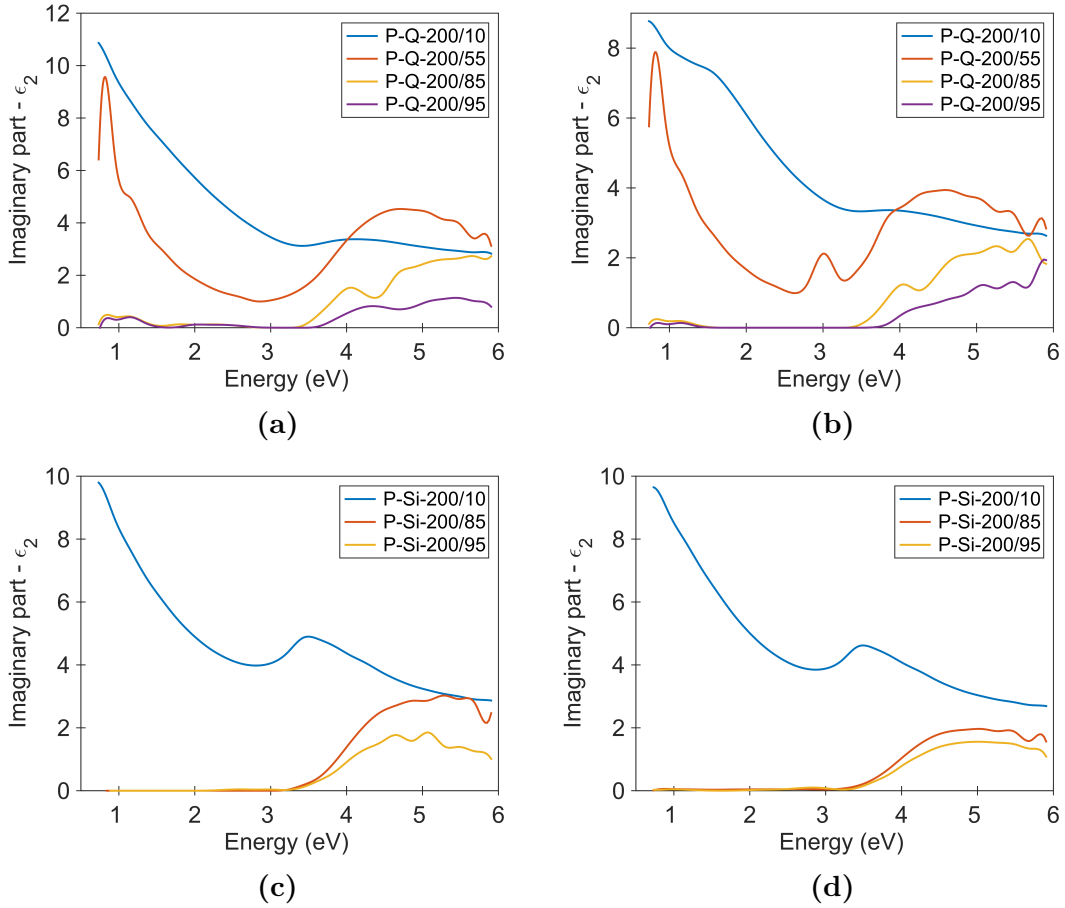

Figure 6.11: (a) and (b) is the imaginary part of the DF for fixed and varying thickness, respectively, to model the surface roughness in the low growth temperature P-Q series. (c) and (d) same as for (a) and (b), but for the low growth temperature P-Si series.

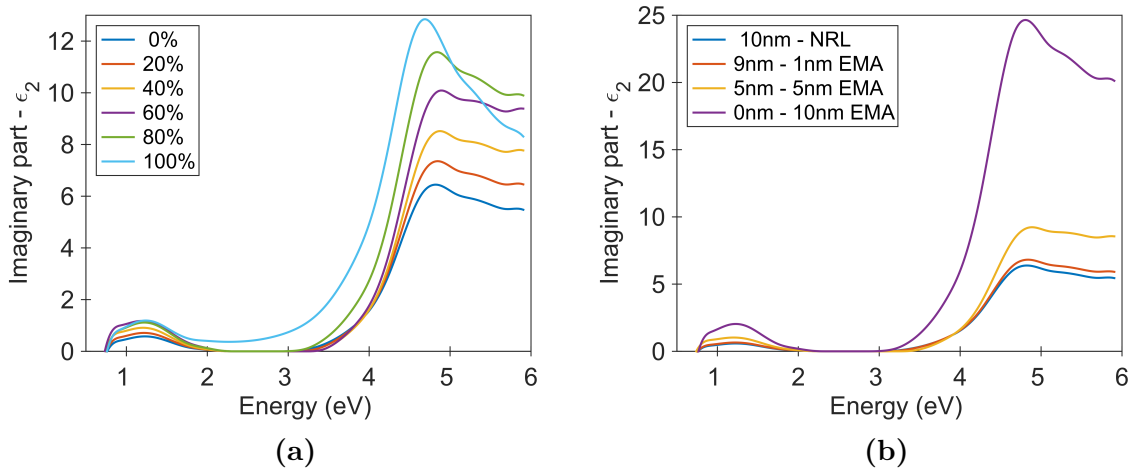

Figure 6.12: (a) Simulation of the DF for different percentages of void for sample SC-C01-300 with a B-spline and EMA-layer model. (b) As (a), but thicknesses of the EMA and B-spline layers varied.

After understanding more of how the DF was affected of different parameters in the EMA layer, an attempt of using two EMA-coupled layers was performed. The upper layer was assumed to be the top surface roughness with a 50/50 mixture of materials and void. The second layer had the percentage of void as a fit parameter between 0 and 50 %. The new attempt did not results in a better MSE, and yet a new model was developed: In the software CompleteEASE, a graded layer can be coupled to another layer with exactly the same DF. The idea here is to use the graded layer function, as described in section 4.4.3, and use either the linear or non-linear grade type to model the roughness and the mixture between void and material. As mentioned in section 4.4.3, the non-linear grade can be found in four different formats, depending on the exponential and the symmetry. In addition, the percentage of void could be negative which results in an unphysical model. However, in all cases, the linear grade type obtained the best MSE (not shown). Another thing noted during the attempts was that the thickness of the coupled layer was thicker for the linear model.

As seen in Figure 6.11, there seems to be a peak around 1 eV, especially for P-Q-200/85 and P-Q-200/95. Therefore, two new different models were made with a T-L used above the band gap, and a Gaussian for the peak around 1 eV as an oscillator layer and a graded layer coupled to this oscillator layer. Both a linear (model 13) and a non-linear (model 14) layer was used. The results for P-Q/Si-200/85 and P-Q/Si-200/95 are shown in Figure 6.13. As one can see, both models followed each other for all four samples, but divided after the band gap. The linear model reached a maximum in the spectral range of the light emitted from the lamp, while the non-linear continued to increase. Based on this new knowledge about how the graded layers reacted, a B-spline and a coupled layer with linear grade model was created for P-Si-200/85 and P-Si-200/95, showed in Figure 6.14. Here, it were observed peaks around 1 eV, 2.2 eV and 2.8 eV, as pointed out with black arrows.

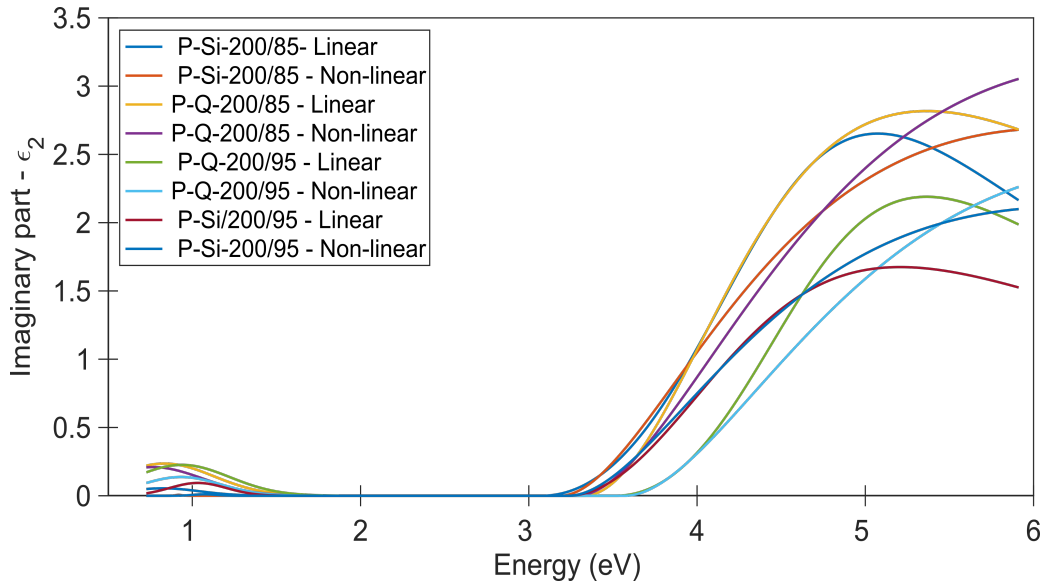

Figure 6.13: ϵ_2 of the DF for model 13 and 14 with a coupled linear and non-linear graded layer, respectively, for P-Q/Si-200/85 and P-Q/Si-200/95.

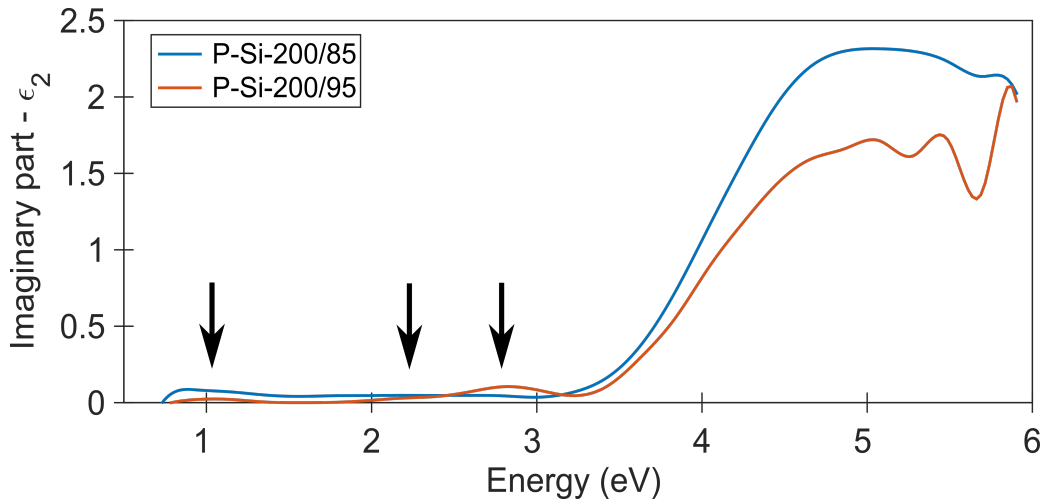

Figure 6.14: ϵ_2 of the DF for a B-spline with a coupled and linear grade model for P-Q/Si-200/85 (blue line), and P-Q/Si-200/95 (red line).

Based on the B-splines shown in the figure, new oscillator layers were developed. One of the models had a Tauc-Lorentz (T-L) and a Cody-Lorentz (C-L) for the band gap and above, and two Gaussians for absorption below the band gap. A MSA was performed with individual fit on all parameters except the band gap E_g and the center of the energy peaks. The results for ϵ_2 of the SC-C01 series are shown in Figure 6.15 (a), while in (b) the contributions from each oscillator for SC-C01-300 is shown. In addition, a Drude oscillator for free carriers was added to the model, but this only decreased the MSE for the most reduced samples (not shown). The surface roughness was modeled as a coupled layer to the oscillator layer with linear grading. The slope was set to be larger than zero and lower than one. As a result, the percentages of void decreases from top to bottom as one would expect without the void to exceed 100%. The offset, i.e. the place in the sample with void equal zero, was one of the fit parameters, but was set to almost zero for all samples. In section 4.4.3, it was presented that the linear grade could results in negative percentages of void to raise the DF. However, it is possible to make the linear grade physical with restricting the slope of the linear variation to be between 0 and 1, and set the offset equal zero, i.e. zero void in the bottom of the layer. This was one motivation for trying the same model on the thicker samples for the PLD series. The only difference between model 16 and 2 was that the surface roughness layer was included. The C-L oscillator did not continue to increase after the band gap as it did in model 2. Seen from Figure 6.15 (b), the T-L seemed to have a peak just outside the spectral range and could therefore be justified to exists.

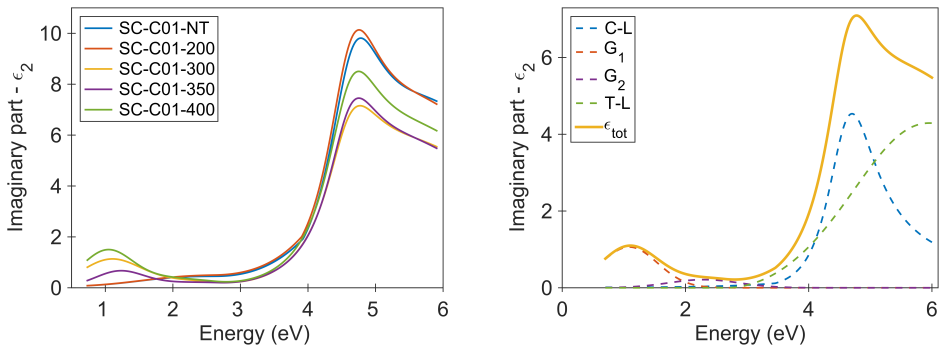

(a) **(b)**

Figure 6.15: (a) ϵ_2 of the DF for model 16 (T-L, C-L, 2 Gaussians) for SC-C01 series given in Table 4.3.1 with MSA. (b) Contribution from each oscillator for SC-C01-300.

Figure 6.16 shows the results for model 19, 20, a B-spline-Coupled model (model 21) and 23 where (a) is for P-Q-200/10, (b) P-Si-200/10, (c) P-Q-200/55, (d) P-Si-200/85, (e) P-Q-200/85, (f) P-Si-200/95 and (g) P-Q-200/95. Model 19 consists of a T-L, four Gaussians and a Drude oscillator with a linear graded layer coupled. The offset was one of the fit parameter and void in the sample could be a negative value which is not physical. Model 20 is the same as 19, but with offset set equal zero to make the model physical. The B-spline-Coupled model used first a Cauchy layer for energies between 1.8 eV to 2.8 eV to determine the thicknesses, and then expanded to the whole spectral range. The RL was modeled by a linear grade type with offset set to zero and the slope was fitted in the range between zero and one. Model 23 was as 20, but with a T-L and a C-L for above the band gap, three Gaussians for absorption below the band gap and a Drude for free carriers at low photon energies. For all samples deposited on quartz, backside reflections were taken into account as there are reflections from the backside of the transparent substrate. As a result for including the backside reflection, the MSE improved significantly (not shown). As seen in Figure 6.16 (h), both the T-L and C-L has the energy peak in the spectral range of the measurement and it seemed to be possible to only use a T-L to model above the band gap.

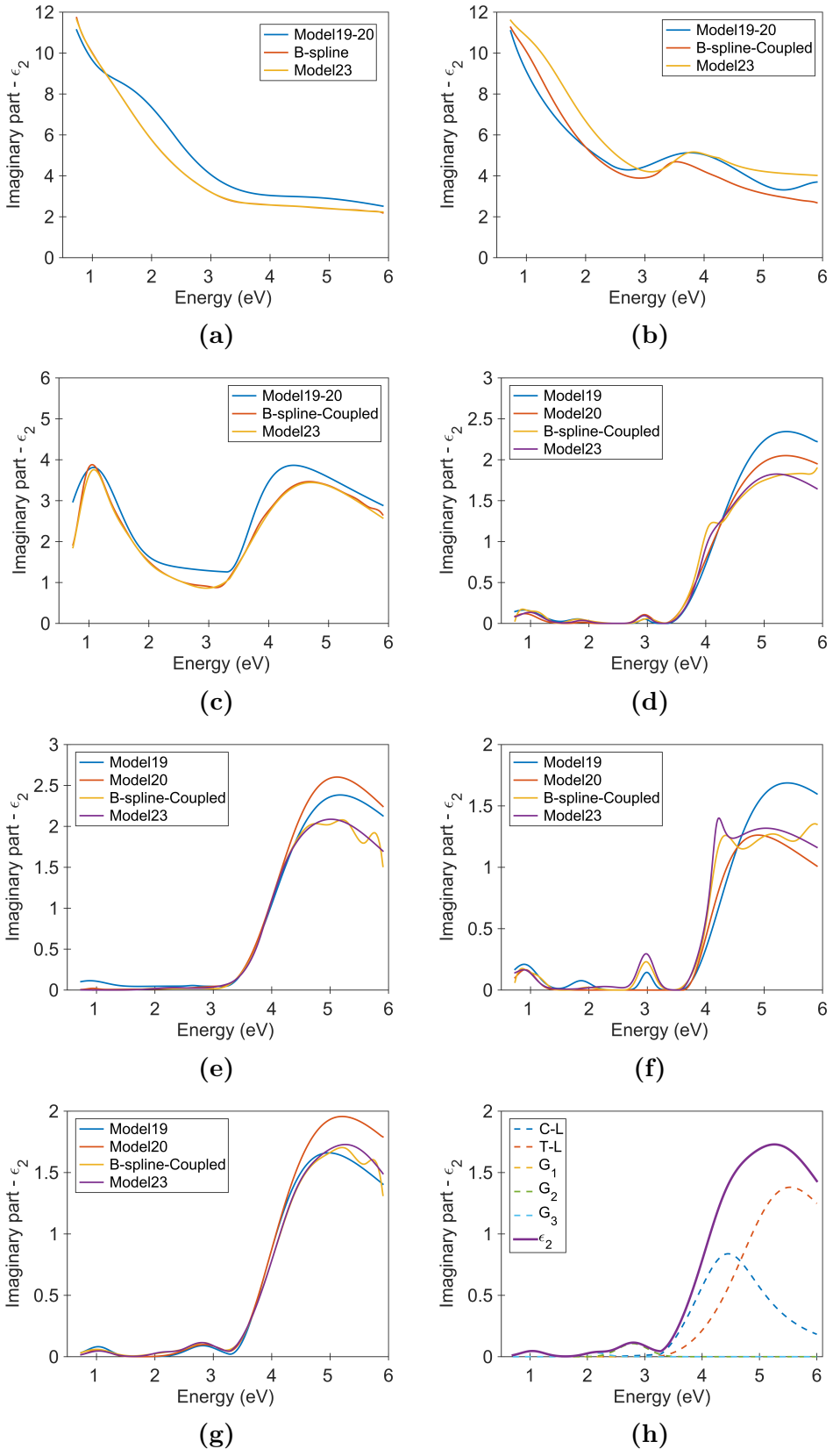

Figure 6.16: ϵ_2 for 4 of the models (see legends) for the low growth temperature series from PLD, given in Table 4.1: (a) P-Q-200/10, (b) P-Si-200/10, (c) P-Q-200/55, (d) P-Q-200/85, (e) P-Si-200/85, (f) P-Q-200/95 and (g) P-Si-200/95. The model (model 19) consists of a T-L, four Gaussians and a Drude oscillator with a coupled linear graded layer. The offset is one of the fit parameter and void can be negative. Model 20 is the same as 19, but with offset set to zero. The B-spline-Coupled model (model 21) used first a Cauchy layer for energies between 1.8 to 2.8 eV to determine the thicknesses, and then expanded to the whole spectral range. This model is yet another model with a linear graded layer as surface roughness with offset set to zero. Model 23 is a model as 20, but with a T-L and C-L for above the band gap, three Gaussians for absorption below the band gap and a Drude oscillator for free carriers at low energies. (h) Contribution from each oscillator for model 23 for sample P-Si-200/95.

Something else that helped to modeling was to compare the transmittance measurements and the transmittance generated from the model, as shown in Figure 6.17 for the the low growth temperature series, given in Table 4.1. The measured transmittance are shown as solid lines and the generated transmittance as dashed lines. The blue lines are for P-Q-200/10, red lines for P-Q-200/55, black lines for P-Q-200/85 and green lines for P-Q-200/95. As one can see, the agreement between the measured transmittance and the generated transmittance is poor. The region with bad fit coincides with the absorption peaks shown in Figure 6.16 (d) and (f). As seen, the model does predict too low transmittance, which indicates that the contributions from the Gaussians below the band gap actually should be closer to zero.

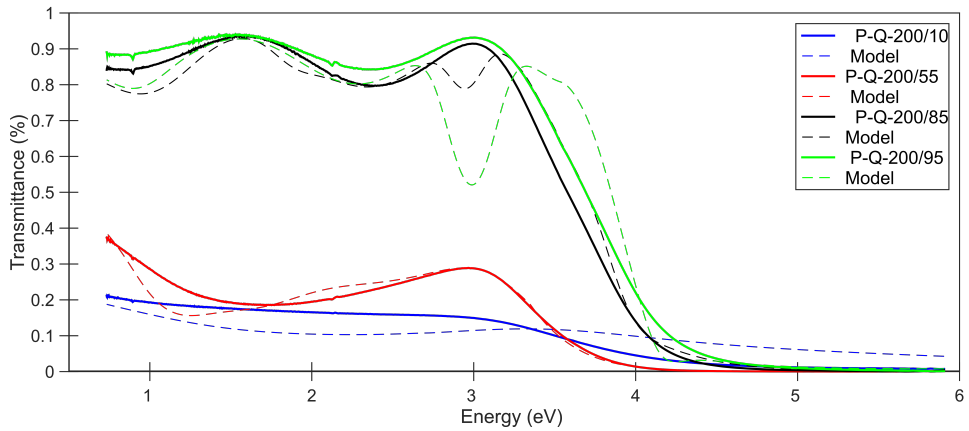

Figure 6.17: Shows the measured transmittance as lines and the generated transmittance as dashed lines for the quartz samples for low substrate temperature series for model 23. The blue lines are for P-Q-200/10, red lines for P-Q-200/55, black lines for P-Q-200/85 and green lines for P-Q-200/95.

A summary of all oscillator models are listed in Table 6.3, with a short comment. Based on the results from model 23 and the transmittance measurements, the final model and oscillator layer were developed and will be presented next.

Table 6.3: An overview of the different models developed during the work with the thesis, with a small comment to the models.

Model #	Layers/Oscillators	Comment
1	C-L, T-L, G	Fixed E_g
2	C-L, T-L, 2G	Fixed E_g
3	C-L, 3G	Fit on: Amp 1-4, Br 1-4, Ep1, En 2-4
4	Model 3 + D	Improved MSE for most reduced
5	Model 3 + T-L	Not physical
6	C-L, T-L, 2G	With roughness layer
7	Model 6 + D	As model 6, with a Drude model
8	Bspline + EMA-coupled	fitted % of void
9	Cauchy ⇒ B-spline + EMA-coupled	As 8, but thickness from Cauchy
10	B-spline + 2 EMA-coupled	For high growth temperature series
11	B-spline + Coupled with grade	Starting mat. for B-spline
12	Model 11	As 11, but another starting mat.
13	T-L, G + Coupled with grade	Linear
14	T-L, G + Coupled with grade	Non-Linear
15	T-L, 3G	New oscillator
16	T-L, C-L, 2G	New attempt for old model
17	Model 16 + D	As 16, but with a Drude oscillator
18	T-L, C-L, G, D	New model, with roughness layer
19	T-L, 4G D	Backside reflection, varying offset
20	Model 19	Offset = 0
21	B-spline with grade	Linear, offset = 0
22	T-L, 3G	Backside reflection, linear grade
23	T-L, C-L, 3G, D	As 22, new oscillators

6.4 The Final Model

After much trial and error, and with use of information from other sources, as presented in section 4.2.3 and 4.3.2, a final model and oscillator layer were developed. The final model for the low growth temperature series from PLD is shown in Figure 6.18 (a). Leftmost is a schematic illustration of the layers. In the middle, SEM picture for sample P-Si-200/95 and rightmost P-Si-500/55. The substrate is either quartz or silicon and is the bottom layer. Top of that follows first the oscillator layer, which is assumed to be 100 % dense (0 % void). As seen from the SEM pictures in the figure, above the homogeneous and continuous layer, there is a mixture of void and material where the material dominates. Therefore, the third layer in the final model was a Bruggeman EMA (equation (5.2.16)) layer where the percentage of void could be fitted in the range between 0 % to 50 %. At the top of the model, a surface roughness layer was included with a 50/50 mixture of material and void from the software. The final model for the SC-series is similar, but the EMA layer was skipped and only modeled as Substrate/Oscillator/Roughness, as shown in Figure 6.18 (b). For samples deposited on quartz, backside reflections from the substrate were taken into account. Transmission data seen in Figure 6.3 were also used as help for the fitting routine to obtain the best results.

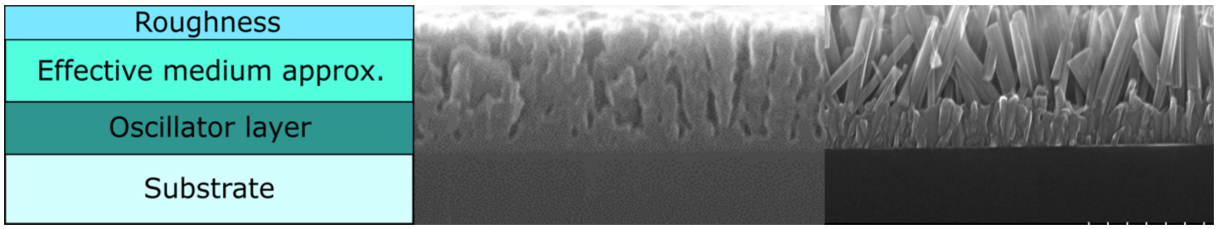

(a)

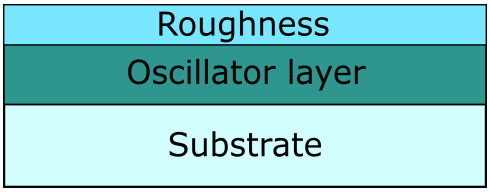

(b)

Figure 6.18: (a) All layers for the model for the PLD series with low growth temperatures. Leftmost is a schematic illustration of the order of the layers. In middle, SEM picture for sample P-Si-200/95 and rightmost P-Si-500/55. (b) All layers for the model for the SC-series.

The final oscillator layer in both models in Figure 6.18 consists of five oscillators in total, where an example of the contribution from each of the oscillators is shown in Figure 6.19. The dark blue line is a Tauc-Lorentz (T-L) oscillator, red, yellow and purple lines are Gaussians, the green line is the free carriers contribution (Drude oscillator) and the light blue is the final ϵ_2 which is the sum of all oscillators. The free carriers contribution D* is calculated as the sum of the T-L and the three Gaussians subtracted from ϵ_2 obtained from the fitting process. The example is for sample P-Q-200/10. The T-L describes ϵ_2 above the band gap E_g, as presented in section 5.2.1. The three Gaussians are for absorption bands below E_g and the Drude oscillator take into account the free carriers absorption. In total there were 19 fit parameters for the oscillators. These may be found in Table 6.4, where A_0 and A_n $n = 1, 2, 3$ are for the amplitudes of the oscillators, Br is the broadening, E_g the band gap energy, E_0 and E_n $n = 1, 2, 3$ is the energy position of the oscillators, ρ is the sample resistivity and τ is the scattering time. In addition, the thickness of the layer, E_∞, A_{UV} and E_{UV} were fitted simultaneously. E_∞, A_{UV} and E_{UV} represents contributions to ϵ_1 outside the range of the measurement. The reason to use a Tauc-Lorentz oscillator is that it only describes the DF above the band gap and will not affect the results below the band gap. In addition, the Gaussians were restricted in width so they would not affect the DF above the band gap significantly. However, in Figure 6.19 it is possible to see that the Gaussians have small contributions above the band gap.

Table 6.4: Overview of the fit parameters in the oscillator layer. A_0 and A_n $n = 1, 2, 3$ are for the amplitudes of the oscillators, Br is the broadening, E_g the band gap energy, E_0 and E_n $n = 1, 2, 3$ are the placement energy of the oscillators, ρ is the resistivity and τ is the scattering time.

Oscillator	Fit parameters	Description
Tauc-Lorentz	A_0, Br, E_0, E_g	Band gap, and above
Gaussian	A_n, Br, E_n $n = 1, 2, 3$	Absorption peaks below E_g
Drude	ρ, τ	Free carriers contribution

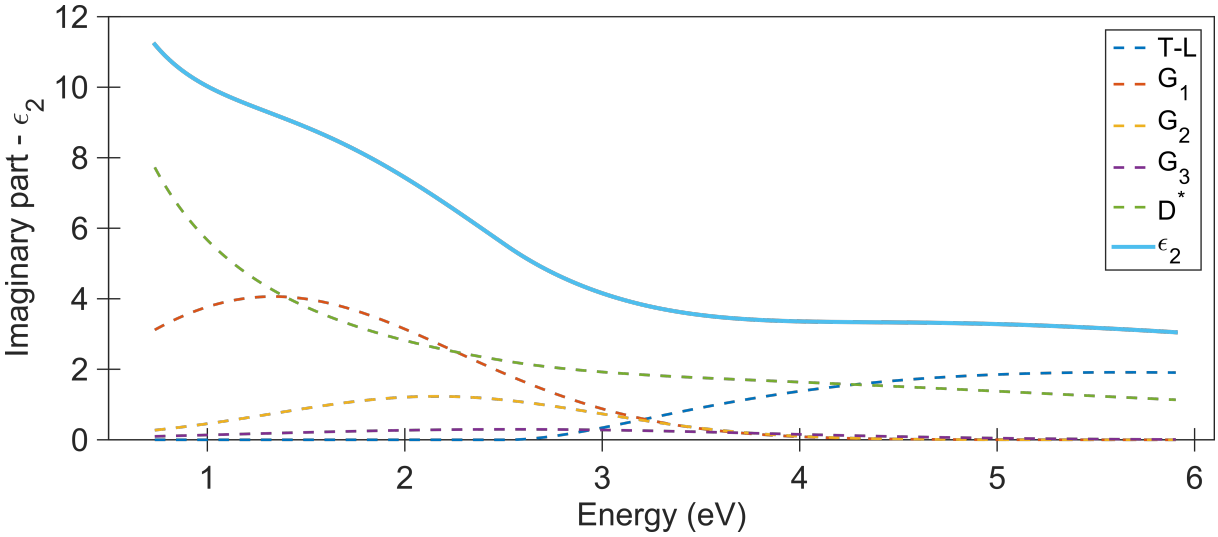

Figure 6.19: An example for contributions from each oscillator in the oscillator model. The dark blue line is a Tauc-Lorentz (T-L) oscillator, red, yellow and purple lines are Gaussians, the green line is the free carriers contributions (Drude) and the light blue is the final ϵ_2 which is the sum of all oscillators.

6.5 Results and Discussion - PLD Series

The samples from PLD consisted of two different series, as presented in section 4.2.2. Two different fitting procedures (called runs from now) were performed, where the first run fitted all parameters, including the thicknesses of all the three layers. The second run obtained the thickness of the oscillator layer from a Cauchy layer for low energies, where the samples were assumed to be transparent. The EMA and the roughness layers were fitted simultaneously with the Cauchy layer. Next, the Cauchy layer was replaced with the oscillator layer and the thicknesses were held fixed. Thus, only the oscillator parameter from Table 6.4 were fitted over the whole spectral range. The results for sample P-Q-200/55 is not a part of the results due to strange behavior, both in the SE measurements (Figure 6.16 (c)) and other experiments. First, the results and discussion for the samples with low growth temperature (hereafter PLD LT-series) are presented, before the results from the high growth temperature series (hereafter PLD HT-series) follow the same procedure.

6.5.1 PLD LT-Series

Results

To see how well the model matches the experimental values of Ψ and Δ, it is possible to plot the pseudo DF given in equation (4.4.22). The pseudo DF for the PLD LT-series is shown in Figure 6.20 for sample P-Q-200/10 (a), P-Si-200/85 and P-Q-200/95 (c) from the first run at three angles of incidence (60°, 65° and 70°). The red lines are for ϵ_1, the green lines for ϵ_2 and the dashed lines is the generated values from the model. As one can see, it is very good agreement between the model and the experimental obtained values for the pseudo DF, ϵ_1 and ϵ_2. This is not a physical representation of the DF, just a way to compare the model with the experimental values. This can be confirmed from Figure 6.20 where ϵ_2 is negative for low energies, which is not a physical value for ϵ_2.

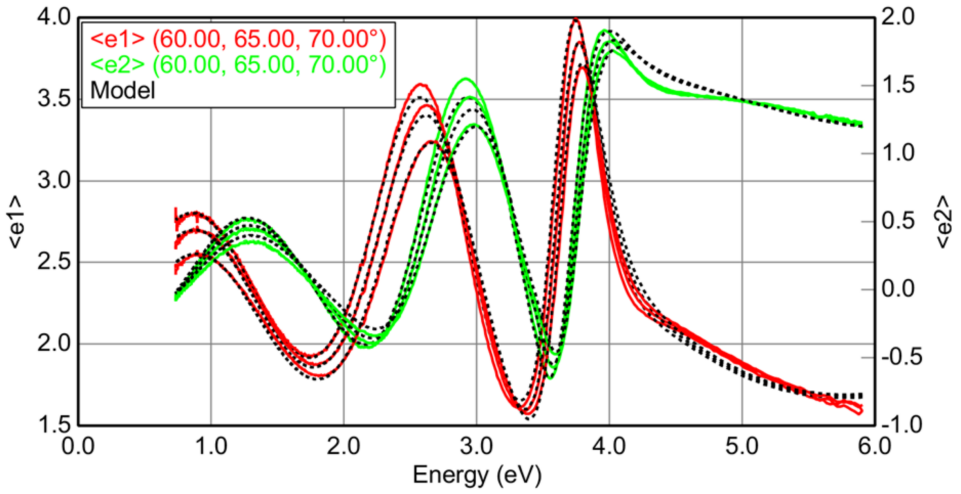

(a)

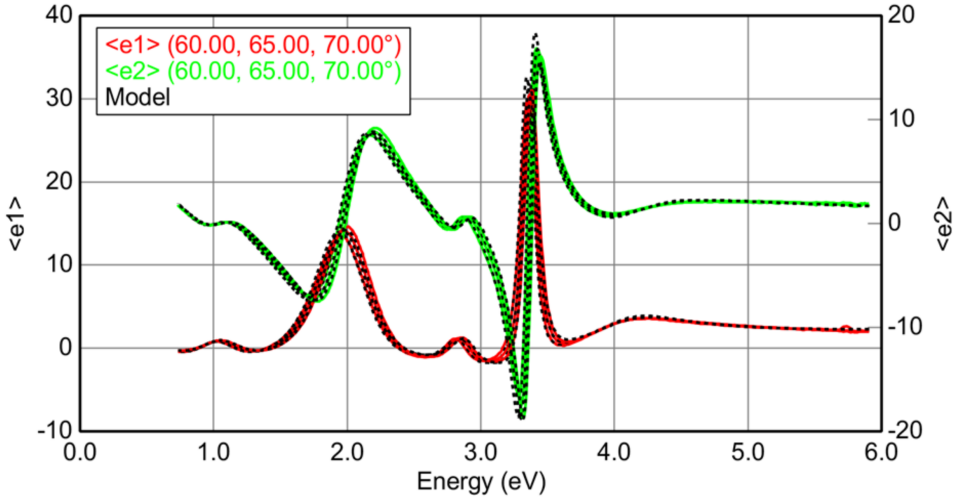

(b)

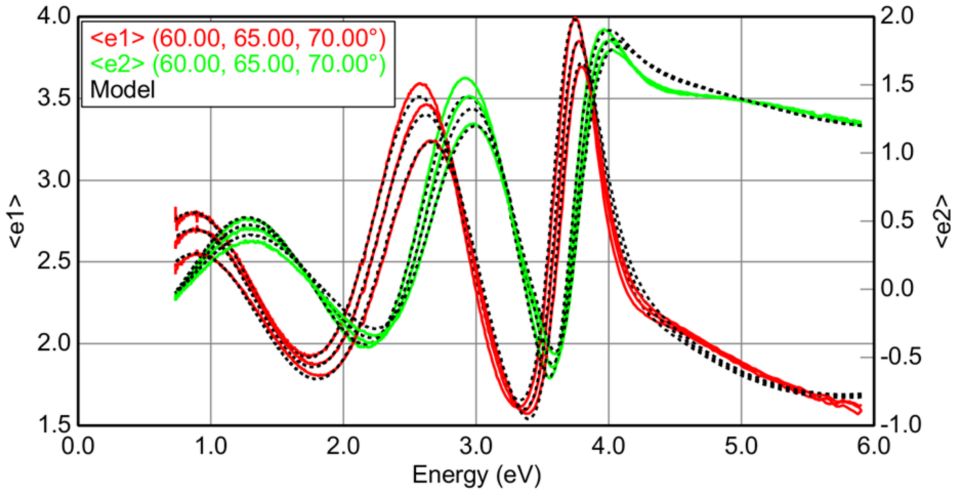

(c)

Figure 6.20: (a) Pseudo-dielectric function for P-Q-200/10 for angles of incidence of 60°, 65° and 70° for ϵ_1 (red), ϵ_2 (green) and the generated pseudo DF from the oscillator layer (dashed). (b) As (a), but for P-Si-200/85. (c) As (a), but for P-Q-200/95.

The results for ϵ_1 of the PLD LT-series in the oscillator layer are shown in Figure 6.21, where (a) is the real part of the DF, ϵ_1, for the PLD LT-series from the first run and (b) Zoom of the four least reduced samples. (c) ϵ_1 where the thicknesses were found by using a Cauchy layer in the second run. The results for ϵ_2 are shown in Figure 6.22. P-Si-200/10 and P-Q-200/10 were skipped from the second run since they did not have any transparent region, as Figure 6.22 (a) shows. If there are no transparent region, the Cauchy formalism fails. The values for the most important fit parameters are listed in Table 6.5 and 6.6 for run one and two, respectively. The values will be used later for trying to determine the molybdenum oxide phases present in each sample.

Table 6.5: The most important fit parameters for the PLD LT-series with sample name, total thickness as a sum of the three layers in the model, RL thickness (a part of the total thickness) in nm, EMA layer thickness in nm, percentages of void, band gap energy E_g, the placement of the oscillators E_i, $i = 0, 1, 2, 3$, and the mean square error (MSE).

Sample	Total (nm)	RL (nm)	EMA (nm)	Void (%)	E_g (eV)	E_0 (eV)	E_1 (eV)	E_2 (eV)	E_3 (eV)	MSE
P-Q-200/10	78	2.5	21	22	2.5	3.6	1.3	2.2	2.5	6.2
P-Si-200/10	79.6	0.61	16	40	2.5	4.3	1.2	2.4	2.6	5.4
P-Q-200/85	220	12	180	11	3.2	3.7	1.5	-	2.8	6.9
P-Si-200/85	210	9.6	170	28	3.1	4.4	1.1	-	-	19
P-Q-200/95	250	19	210	23	3.3	4.0	-	-	2.8	8.5
P-Si-200/95	220	18	170	32	3.2	4.4	1.3	-	-	6.4

Table 6.6: The most important fit parameters for the PLD LT-series, where the thicknesses were obtained from the transparent region with a Cauchy layer. The table contains the total thickness as a sum of the three layers in the model, RL thickness (a part of the total thickness) in nm, EMA layer thickness in nm, percentages of void, band gap energy E_g, the placement of the oscillators E_i, $i = 0, 1, 2, 3$, and the mean square error (MSE).

Sample	Total (nm)	RL (nm)	EMA (nm)	Void (%)	E_g (eV)	E_0 (eV)	E_1 (eV)	E_2 (eV)	E_3 (eV)	MSE
P-Q-200/85	230	13	180	12	3.3	3.7	1.5	2.3	2.8	9.6
P-Si-200/85	210	9.6	150	10	3.1	4.4	1.3	-	-	19
P-Q-200/95	250	18	210	25	3.3	4.0	-	2.1	2.8	10
P-Si-200/95	220	15	170	25	3.2	4.3	-	-	2.6	10

As one can see for both ϵ_1 and ϵ_2 in Figure 6.21 and 6.22, P-Si-200/10 and P-Q-200/10 differs from the other samples. For ϵ_1, the function continues to increase significantly for low energies towards zero, while the other samples slowly decrease. All samples have a maximum around 4 eV, before they starts to decline and flatten out at higher energies. As seen from the zoomed in version (Figure 6.21 (b)), ϵ_1 starts to increase again after 5.5eV. Another feature is that the samples grown on silicon have larger ϵ_1 than the samples grown on quartz. The same is observed for the second run. The differences between the first and second run are significant. For the second run the function are closer each other, but the more reduced samples, i.e. P-Si-200/85 and P-Q-200/85, are still slightly larger.

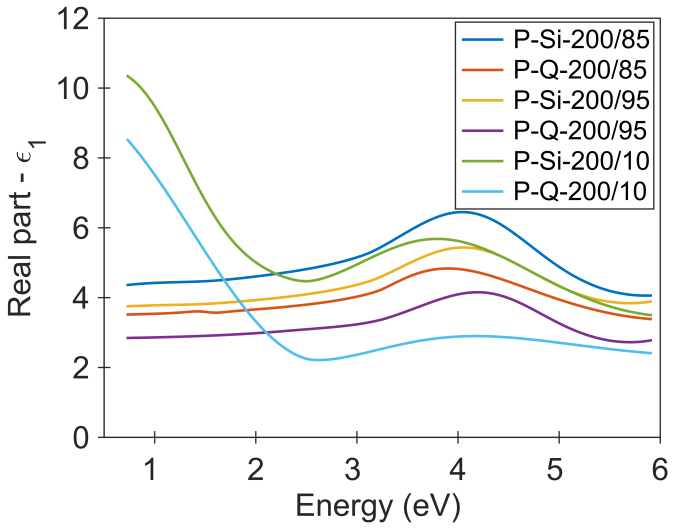

(a)

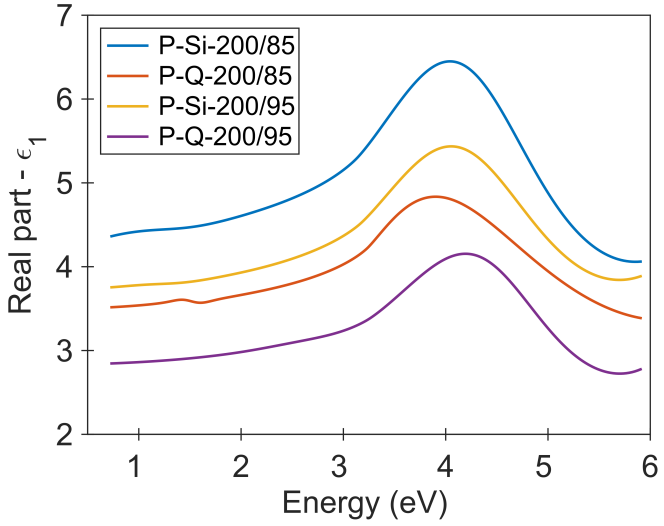

(b)

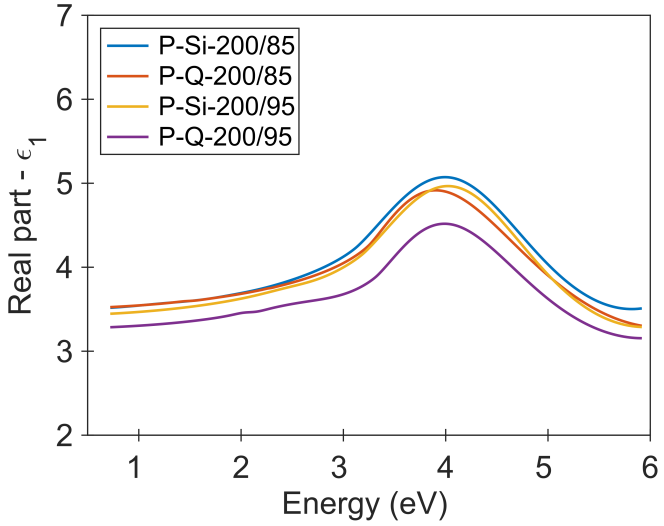

(c)

Figure 6.21: (a) The real part of the DF, ϵ_1, for the PLD LT-series for the first run. (b) Is a zoom of (a). (c) As (b), but for the second run.

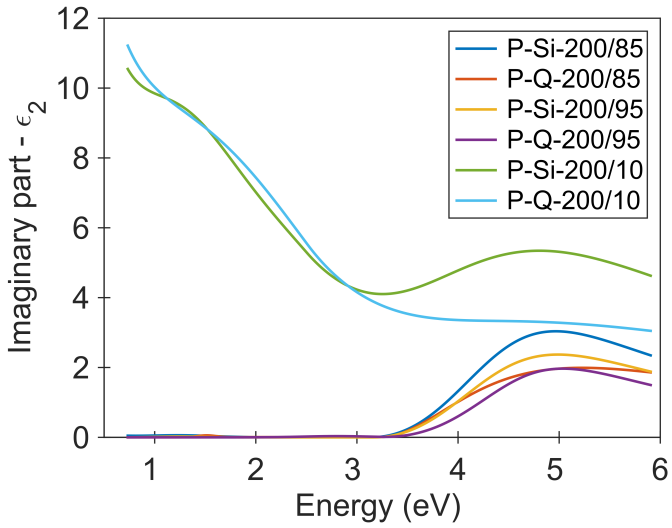

(a)

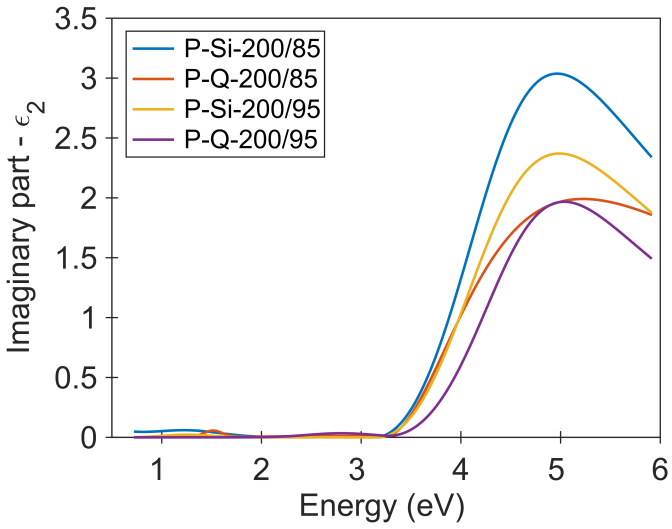

(b)

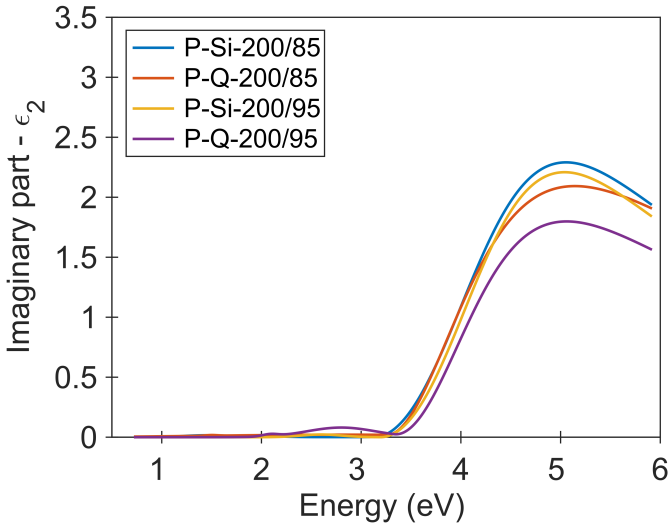

(c)

Figure 6.22: (a) The imaginary part of the DF, ϵ_2, for the PLD LT-series for the first run. (b) Is a zoom of (a). (c) As (b), but for the second run.

Same trends are observed for ϵ_2 in Figure 6.22. P-Q-200/10 and P-Si-200/10 differs from the other, and have large contributions from the Gaussians oscillators and the free carrier contribution as the function continues to rise towards lower photon energies. Both samples have $E_g = 2.5$ eV as seen in Table 6.5. Sample P-Si-200/85, P-Q-200/85, P-Si-200/95 and P-Q-200/95 have ϵ_2 close to zero below the band gap, i.e. they are transparent for all energies below the band gap, with a few exceptions. There are some small contributions from the Gaussians, but they have small amplitudes and large widths. The maximum for ϵ_2 for the samples are around 5.0 eV for the first and second run. The band gap energies for the same samples are in the range 3.1 eV to 3.3 eV and does not change significantly between the two runs, as Table 6.5 and 6.6 shows. The thicknesses are also approximately the same for both runs. The MSE values are acceptable, where all are below 10, except for sample P-Si-200/85 which are 19 in both cases. As for ϵ_1, samples grown on silicon have larger magnitude than the samples grown on quartz. The magnitude also increases with the decrease of the available oxygen under the deposition, i.e. the most reduced samples.

The transmittance for the samples grown on quartz is shown in Figure 6.23, where the solid lines is the measured transmittance and the dashed lines is the transmittance generated from the model. There are oscillations for low energies, both in the model and the measured transmittance. The model fails around the band gap energies, but are in good agreement for low and high energies and the transmittance has better agreement than Figure 6.17. Still, there is bad agreement for P-Q-200/10, and sample P-Q-200/95 had better agreement in the first run, meaning the model is not perfect yet.

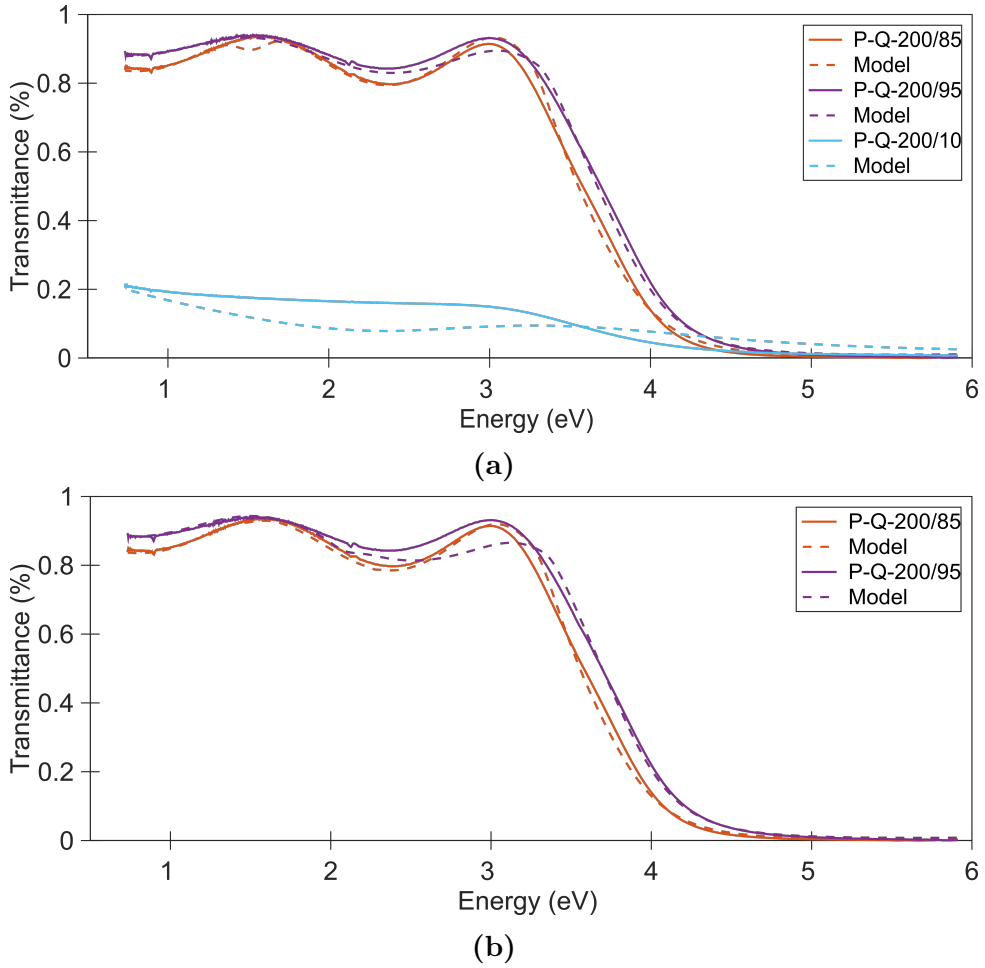

Figure 6.23: (a) The measured (lines) and generated (dashed) transmittance for the PLD LT-series for the first run. (b) As (a), but for the second run for the two least reduced samples deposited on quartz in the PLD LT-series.

Discussion

The band gap energies E_g, listed in Table 6.5 and 6.6 are in good agreement with other observed values which are in the range 2.76-3.70 eV [53, 101, 102, 103]. Several values for E_g for α-MoO_3 are reported, but the typically value for E_g is 3.1 eV [53]. This is in good agreement for E_g for the least reduced samples, as seen in the tables. There was no XRD information available for these samples, but it was shown the high growth temperature series had orthorhombic phase, i.e. α-MoO_3. Since the band gap energies are close to the stated value for α-MoO_3, it could indicate these samples consists of α-MoO_3, especially since β-MoO_3 tends to be at lower values, such as $E_g = 2.9$ eV [53].

Boukhachem et. al. [104] showed in their work that ϵ_1 and ϵ_2 for MoO_3 can be in the range of 3.0 to 4.0 and 0 to 1.3, respectively. Other ϵ_1 and ϵ_2 values from the literature for MoO_{3-x} are shown in Figure 6.24. (a) is for ϵ_1 values where the blue circles are value obtained from May et. al. [102], red circles from Szekeres et. al. [101], yellow circles from Mohamed et. al. [105], purple circles are from Sian et. al. [54] and the green circles are from Arfaoui et. al. [74]. (b) As (a), but for ϵ_2. To extract values from the literature, a program ("Datathief III") was used [106]. The values in the literature were

originally given as the refractive index n and the extinction coefficient k, i.e. the values of ϵ_1 and ϵ_2 in the figure are calculated with equation (4.4.5) and plotted with functions in MATLAB. As seen in the figure, there are large variations between the DFs from the various references. This is probably due to different deposition techniques are used and constitutes of different phases of molybdenum oxide are present. The values for ϵ_1 and ϵ_2 in Figure 6.21 and 6.22 are in good agreement with values from literature. Numerous other studies have also observed absorption below the band gap for energies in the range 0.75 eV to 2.5 eV, for instance [53, 101, 107].

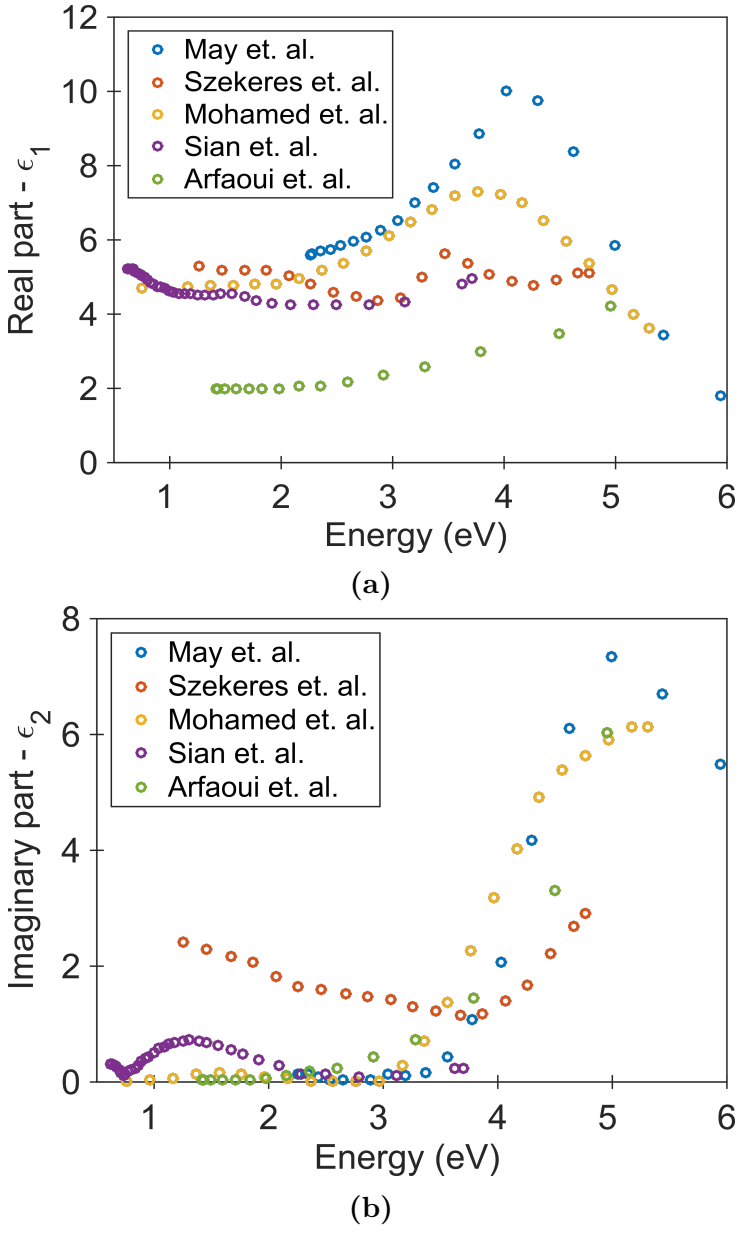

Figure 6.24: (a) ϵ_1 from literature where the blue circles are from May et. al. [102], red circles from Szekeres et. al. [101], yellow circles from Mohamed et. al. [105], purple circles are from Sian et. al. [54] and the green circles are from Arfaoui et. al. [74]. (b) As (a), but for ϵ_2. To extract values from the literature, a program ("Datathief III") was used [106]. The values in the literature were originally given as the refractive index n and the extinction coefficient k, i.e. the values of ϵ_1 and ϵ_2 in the figure are calculated with equation (4.4.5) and plotted with functions in MATLAB.

For the PLD LT-series, there was not determined any E_g from a Tauc-plot, but from the high growth temperature series it was found from a Tauc-plot that P-Si-500/70 had a band gap at 3.2 eV, and mainly consisted of MoO_3, as presented in section 4.2.3. Tauc-plots uses information from transmittance measurements to extract an approximate value for the band gap, and has often large uncertainty. The supplied value is approximately the same energy, as listed in Table 6.5 and 6.6, for the least reduced samples.

As seen in Figure 6.21 and 6.22, there was not a large difference between the first and second run. The largest difference is that for the second run, the ϵ_1 and ϵ_2 are almost overlapping, which could indicate a better model as the DF is not dependent on the thickness. The most reduced samples still have the largest ϵ_1 and ϵ_2 in both runs. As seen from Table 6.5 and 6.6 the RLs and total thicknesses did have approximately the same values for both runs and are in good agreement with the thicknesses presented in Table 4.3. As the thickness did not change significantly could indicate the model suit the thicker samples best.

Looking at ϵ_2, it is possible to attempt to say something about the contents of the samples. As mentioned in section 4.1, Mo_4O_{11} have absorption bands at 1.3 eV, 2.13 eV and 2.42 eV while MoO_2 has a band gap at 2.48 eV [72]. The band gap of MoO_3 is in the range 2.76-3.70 eV [53, 101, 102, 103]. If the fitted E_g values are inside the range of band gaps for MoO_3 and have a transparent region below the band gap the sample will probably mainly consists of MoO_3. As mentioned in section 4.1, MoO_2 has a metallic nature, meaning that samples where Drude contribution is non-zero, probably contain MoO_2. If the band gap energy is closer to the reported values for MoO_2 in addition, one can assume the sample mainly consists of MoO_2, or has large contributions from MoO_2 phases. Finally, if there are peaks around the absorption energies for Mo_4O_{11}, this could indicate contributions from this phase of the molybdenum oxides, or some of the other more rare oxides such as Mo_9O_{26} and $Mo_{18}O_{52}$.

From Figure 6.22, one can see that the four least reduced samples, i.e. P-Si-200/85, P-Q-200/85, P-Si-200/95 and P-Q-200/95 are almost transparent below the band gap, which is in the range 3.1 eV to 3.3 eV. Using the arguments presented above, this indicates presence of MoO_3, with possible a few defects in the band gap as there are small contributions from the Gaussians below the band gap. The two last samples have large contributions from free carriers and the Gaussians below the band gap. These two samples also have $E_g = 2.5$ eV which indicates that the sample contain mainly MoO_2 with contributions from Mo_4O_{11}, or one of the other intermediate phases. This is reasonable as the oxygen available during the deposition was much lower for these two samples (P-Q-200/10 and P-Si-200/10) than the other samples that had a oxygen flow during the fabrication of either 85, or 90 sccm.

As seen from the SEM pictures in Figure 4.7, both the proportion of void and the surface roughness of the samples increased when the flow of oxygen increased, i.e. the films got more porous. The most homogeneous and continuous sample is P-Si-200/10 while sample P-Si-200/95 has more void present. This matches the numerical values obtained for the fraction of void (in %) and the thickness of the roughness layer (RL), in Table 6.5 and 6.6 above. From the tables one also see that the sum of the RL and EMA thickness increases with the increase of the oxygen flow. The percentages of void in the EMA layer is also fitted during the fitting procedure, and is shown in the tables. As seen, the percentage increase with the increase of available oxygen resulting in more porous samples, as seen in the SEM pictures. The exceptions for this behavior is for the least reduced samples,

but in these samples the roughness layers are so thin that the EMA layer somewhat also model the roughness at the surface. Comparing the thicknesses in the same tables as above with the thicknesses in table 4.3, one can see they are larger than seen from the SEM pictures. The SEM pictures are taken from the side of the substrate, while the SE measurements performed in the middle. As presented in section 4.2.1, one problem with PLD is that the plume is small and not uniform, and hence the thickness in the middle could be larger than at the sides. A larger plume during the deposition would resulted in a more homogeneous thickness. This could also be seen as the color of the films were different. Another thing to point out is the thicknesses of the samples grown on quartz have a larger thickness than the samples grown on silicon, except for the samples at lowest oxygen flows. It indicates the choice of substrate affects the material deposited on it.

As mentioned, it was observed large difference between the color on the samples. One side of the sample could be very light and blue, while on the other side the samples where red. This could be due to interference in the transparent substrates, but could maybe also be due to different thickness of the thin films on the substrate. The blue and light areas could indicate MoO_3 since it is transparent, while the darker side could indicate the metallic nature of MoO_2. The most reduced samples, P-Q-200/10 and P-Si-200/10, had a very shiny surface which could indicate a metallic nature. A fit parameter for the free carriers in the Drude oscillator is the resistivity, and was fitted to be $\rho = 0.0013$ Ωm for both P-Q-200/10 and P-Si-200/10 which are close to the stated value in Table 4.3. As seen from Figure 6.23 (a), the generated transmittance for P-Q-200/10 is in bad agreement with the measured. A reason for this could be the ρ is fitted to a lower value than the measured. The transmittance lowers for lower ρ as the material becomes more conductive, which could indicate the model is not very good for the most reduced samples from PLD.

In Figure 6.23 (a), there is a dip in the generated transmittance for P-Q-200/85 around 1.5 eV, which coincides with the same energy as one of the Gaussians. This indicates that it should not be any contributions from this oscillator, and should have been closer zero in amplitude, or larger in width instead. Another important thing to note with the transmittance is that the generated transmittance for sample P-Q-200/95 underestimated the transmittance in the energy range from 2 eV to 3 eV, as seen in Figure 6.23 (a). The reason can be found in Figure 6.22 (c), where there is a Gaussian contribution just before the band gap. Hence, this Gaussian should actually be set closer to zero, as in Figure 6.22 (b) where there are good agreement with the transmittance measurements as shown in Figure 6.23 (a). There are no transmittance measurements on the samples grown on silicon due to silicon would absorb the remaining light which did not get absorbed in the molybdenum oxide layer. In addition, there are no conductivity measurements for samples grown on silicon, as silicon is not an insulator as quartz.

6.5.2 PLD HT-Series

Results

Figure 6.25 shows the pseudo DF for sample P-Si-500/55 (a), P-Si-500/70 (b) and P-Si-570/55 (c). As can be seen from the figure, the match between the measured and simulated pseudo DF is poor for all of the samples, except for sample P-Si-570/55. The

MSE values obtained were very large, indicating that the model that has been developed is not suitable for the PLD HT-series. Due to limited time available for this thesis work, we did not develop a better model for the PLD HT-series, and therefore there are no results for the DFs for these samples.

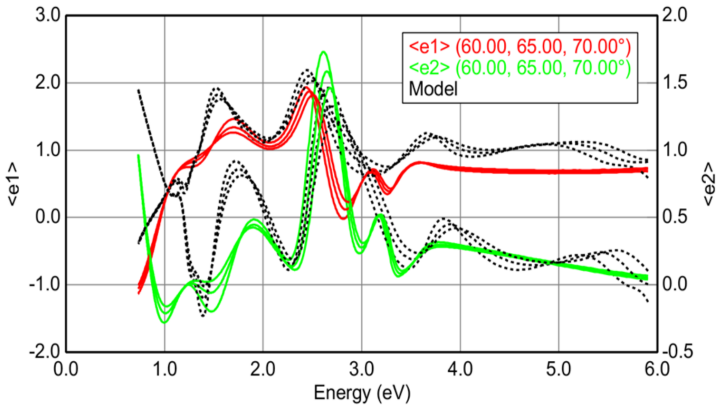

(a)

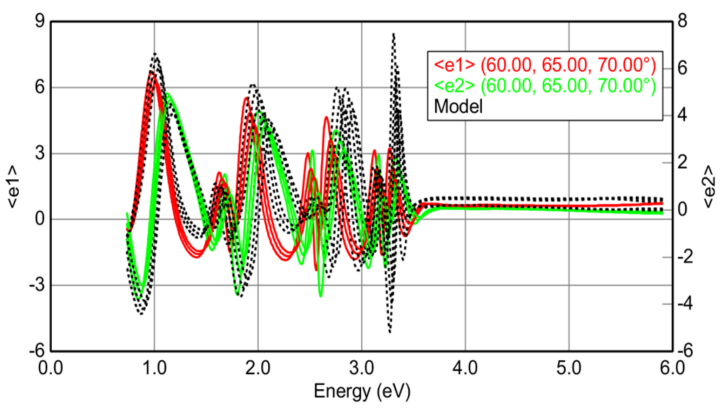

(b)

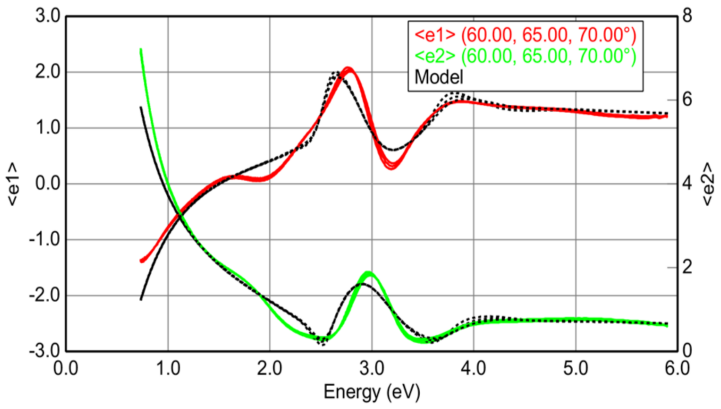

(c)

Figure 6.25: (a) Pseudo-dielectric function for P-Si-500/55 for angles of incidence of 60°, 65° and 70° for ϵ_1 (red), ϵ_2 (green) and the generated pseudo DF from the oscillator layer (dashed). (b) As (a), but for P-Si-500/70. (c) As (a), but for P-Si-570/55.

Discussion

There could be several reasons why the model did not work well for the PLD HT-series. One reason could be the complicated structure of both the materials and the roughness layer. As Figure 4.8 (b) shows (in section 4.2.3), the morphology has large structures, which could be several tens of nm. One of the limitations for use of the EMA layer is that the morphology must be sufficiently larger than the atom sizes and smaller than $\lambda/10$, as presented in section 5.2.4. The latter requirements fails for the low wavelengths, especially for P-Si-500/55, and probably P-Si-500/70. Therefore, a better model for the structure needs to be developed to be able to extract the DF from SE measurements for these more complicated structures.

Another reason for why the model failed on sample P-Si-500/70 could be that from the SEM picture, in Figure 4.8 (c), one can see that there are no continuous layer in the bottom, and this is difficult to model with only an EMA layer. In the model presented in section 6.4, it was assumed the different phases of molybdenum oxide were mixed, but for these samples we know from XRD and XPS that this is probably not the case. As presented in section 4.2.3, it was assumed that the different phases of the molybdenum oxides were present in different layers, which again complicates the model significantly. Each layer will require different oscillator layers. For instance, a layer with a band gap and a free carrier contribution for MoO_2 and three Gaussians at the absorption bands for Mo_4O_{11}. Such models will become complicated and the fit parameters may correlate more.

Firstly, there were a huge difference between color over the samples. On one side, the color could be blue, or yellow, while on the other side it was red and dark. It could be that the light areas consisted of mainly MoO_3 since it is transparent, while the darker areas consists of MoO_2 since it has metallic nature. Even though focus probes were used to focus the beam at the different areas, it was not possible to obtain a good results with use of the oscillator model presented in section 6.4. The color differences could also be due to interference in the transparent samples.

From the SEM pictures in Figure 4.8 and as stated in section 4.2.3, there are large columnar grains and hence there could be different DFs for parallel and perpendicular direction to the columnar grains. If this is the case, an uniaxial layer could have been used instead, where the refractive index is different in z, compared with y and x, for instance. This was used in Beydaghyan et. al. [36] where it was observed different refractive indices in the x and z direction. Using this type of layer would require more fit parameters, and a much more complicated model. To reduce the correlation between the fit parameters, the model should be as easy as possible.

Another way to obtain a good model for such structures is to get a better model for the surface roughness. In Akagawas et. al. [108], they compared the results between a conventional model (a) (used in this thesis with layers stacked on each other), with EMA multilayer model (b) and surface area model (c) as shown in Figure 6.26. The results were significantly better with the complicated model (c), than the conventional model (a). The problem is that one can not use CompleteEASE software for such roughness layers, so one need to make own scripts in MATLAB or Python, for instance. Another way is to use information of the statistics from AFM measurements, proposed by Lehmann et. al. [109]. They also proposed an empirical formula where one could directly use the root

mean square roughness to determine the thickness of the roughness layer for a 50/50 mixture of material and void.

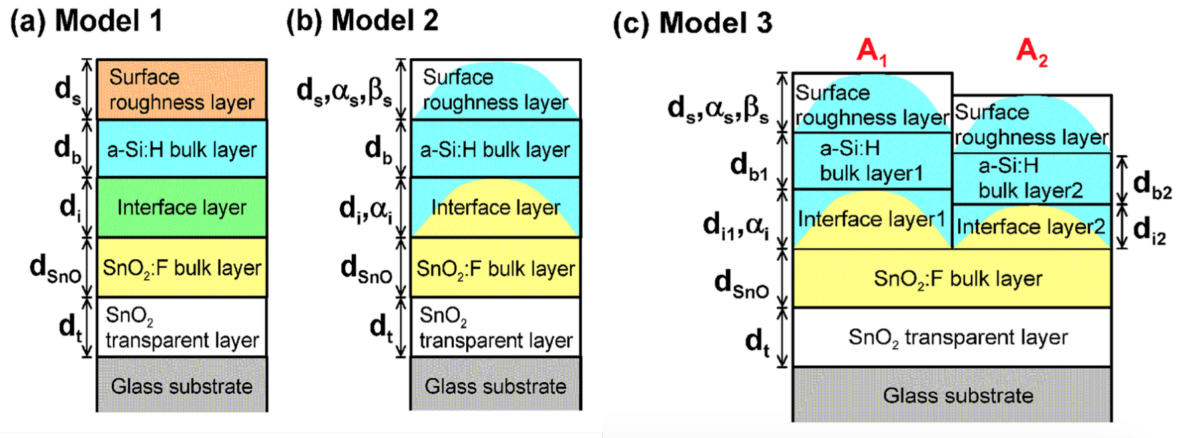

Figure 6.26: Alternative models for modeling high surface roughness. (a) Conventional model. (b) EMA multilayer model. (c) EMA multilayer model with surface area model. Figure is taken from Ref. [108].

6.6 Results and Discussion - Spin Coating Series

From AFM images, it was seen that the sample from the SC-series had less surface roughness than the PLD series. Best fits were obtained if the EMA layer (see Figure 6.18 (b)) was omitted from the model. First, the results for the SC-C05 series will be presented and discussed, followed by the SC-C01 series. As for the PLD series, two runs were performed for these samples too.

6.6.1 SC-C05 Series

Results

The pseudo DF for the SC-C05 series are shown in Figure 6.27 for samples SC-C05-NT (a), SC-C05-400 (b) and SC-C05-450 (c) for the second run where the thicknesses were held fixed. As one can see there is a somewhat good agreement for samples SC-C05-NT and SC-C05-400 at low and high energies. The largest deviations are around the band gap for all three samples, but the shape of the functions are in good agreement. Some small peaks are missing in the simulated function, for instance the double peak around 4.2 eV. It is important to notice that this is neither a physical representation for the DF, as ϵ_2 is negative in some regions. As mentioned earlier, the graphs only indicates how the model can match the experimental values.

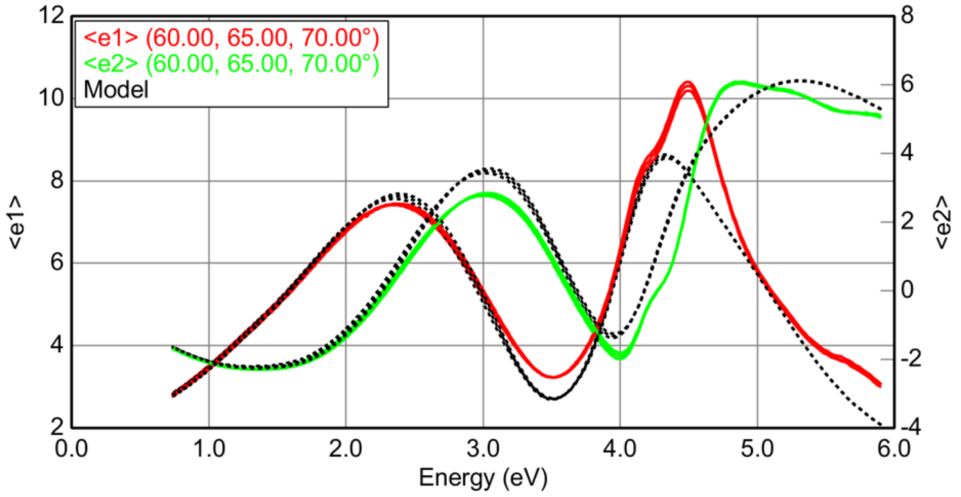

(a)

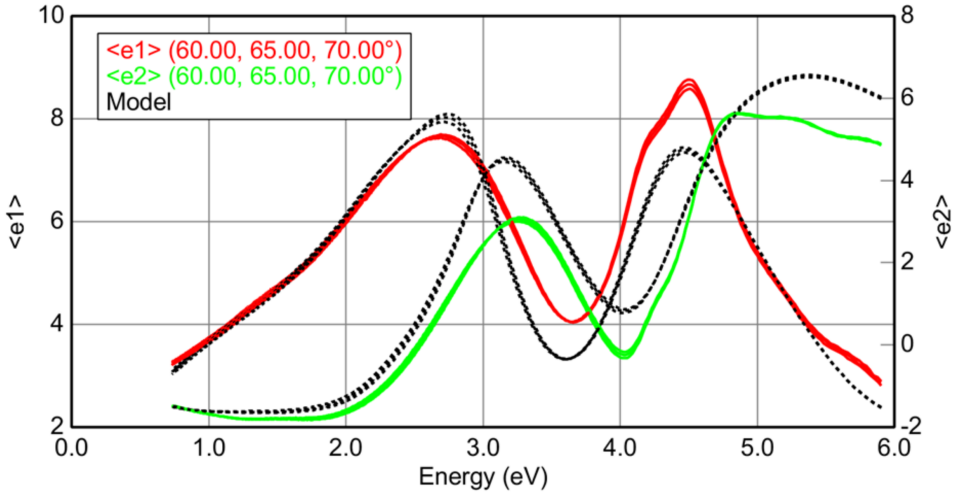

(b)

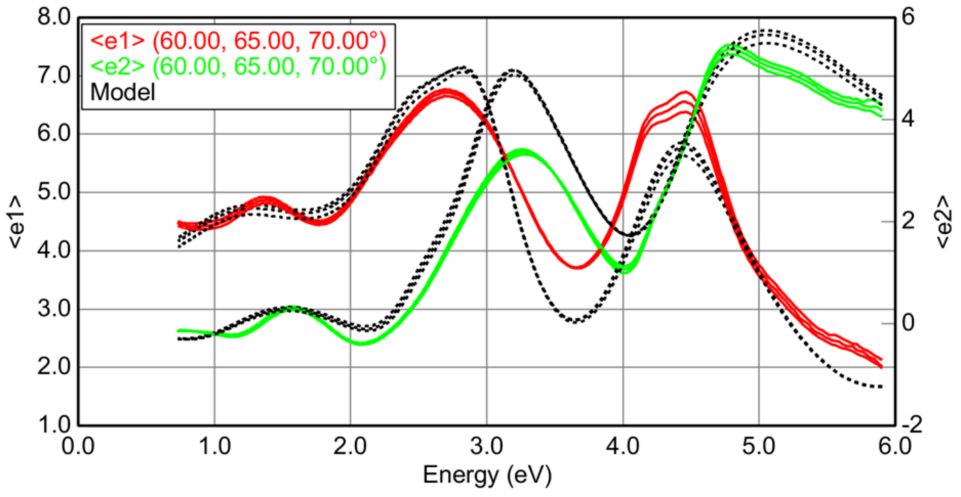

(c)

Figure 6.27: (a) Pseudo-dielectric function for SC-C05-NT for angles of incidence at 60°, 65° and 70° for ϵ_1 (red), ϵ_2 (green) and the generated function from the oscillator layer (dashed). (b) As (a), but for SC-C05-400 . (c) As (a), but for SC-C05-450.

The results from the first run for the final oscillator layer is shown in Figure 6.28, where (a) is the real part of the DF, ϵ_1. (b) As (a), but for the imaginary part of the DF, ϵ_2. In Table 6.7, the fitted values of the most important fit parameters are listed.

Table 6.7: Some of the fit parameters for the SC-C05 series with sample name, total thickness as a sum of the two layers in the model, RL thickness (a part of the total thickness) in nm, band gap energy E_g, the placement of the oscillators E_i, $\quad i = 0, 1, 2, 3$, and the mean square error (MSE).

Sample	Total (nm)	RL (nm)	E_g (eV)	E_0 (eV)	E_1 (eV)	E_2 (eV)	E_3 (eV)	MSE
SC-C05-NT	75	0	3.1	5.0	-	-	-	21
SC-C05-200	67	0	3.0	5.0	-	-	-	15
SC-C05-300	71	0	3.0	5.0	1.3	-	-	15
SC-C05-350	70	0	3.0	5.0	-	-	-	14
SC-C05-400	69	0	3.0	4.9	1.0	1.7	-	16
SC-C05-450	62	0	2.5	4.9	1.4	-	2.6	10

As one can see from Figure 6.28, ϵ_1 have the same behavior as the PLD LT-series, and to the values from the literature, especially May. et al. [102] and Mohamed et. al. [105]. A trend is that ϵ_1 for the different post-treatment temperatures has a similar shape, but decreases in magnitude for higher post-treatment temperatures. One exception from the described behavior is SC-C05-450. For low energies, some kind of oscillation is observed and ϵ_1 has a maximum at 4 eV. ϵ_2 behaves very similar for SC-C05-NT - SC-C05-350 with a transparent region up to the band gap E_g, i.e. no sub-band gap absorption. Above E_g, ϵ_2 starts to grow up to a maximum around 5 eV and then declines. For sample SC-C05-400 there are some contributions from the Gaussians at low energies, while SC-C05-450 both has large contributions from the Gaussians and the free carriers (large contribution from the Drude oscillator). The latter is indicated by the increase of ϵ_2 towards low photon energies. ϵ_2 has the same shape for all samples except for the one reduced at the highest temperature, but the magnitude lowers as function of post-treatment temperature. As Table 6.7 shows, E_g are around 3 eV for all the samples in this series, except for SC-C05-450 which is 2.5 eV and E_0 are approximately the same. The mean square errors (MSE) are in acceptable range between 10 to 21 for all samples in this series.

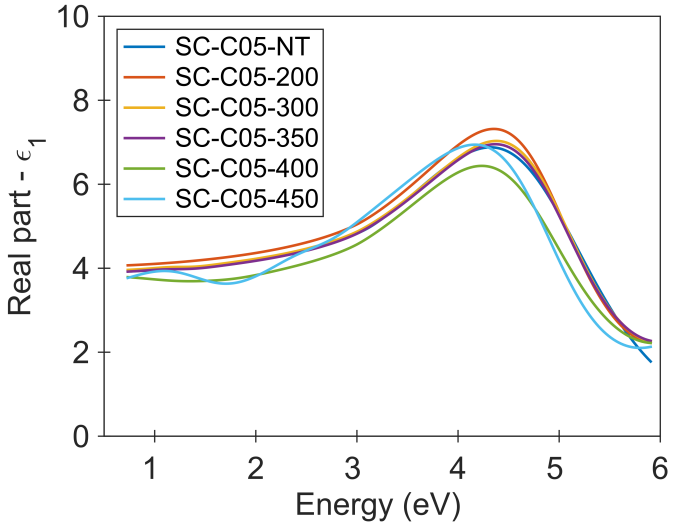

(a)

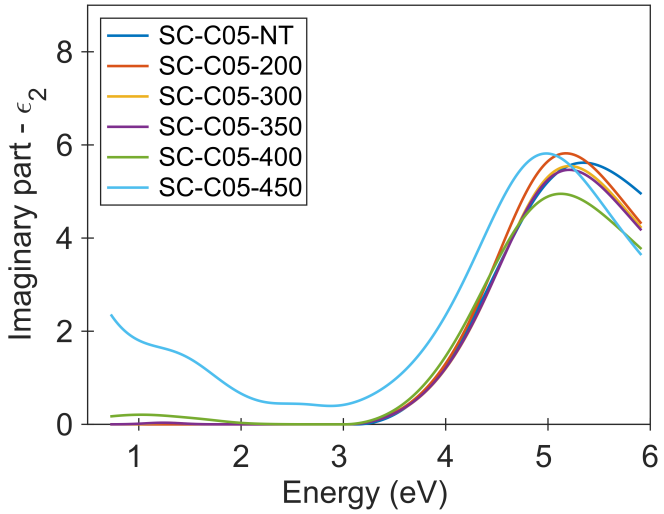

(b)

Figure 6.28: (a) The real part of the DF, ϵ_1, for the SC-C05 series for the first run. (b) As (a), but for the imaginary part of the DF, ϵ_2, for the same samples.

As presented in section 4.3.2, the samples were supposed to be around 60 ± 5 nm from profilometry. As seen from Table 6.7, the thicknesses were significantly larger. As for the PLD series, a second run was performed for this series too. The fitted values of the most important fit parameters are listed in Table 6.8 and the new results for the DF are shown in Figure 6.29. E_g values are around 3.1 eV, close to the first run, except SC-05-400 and SC-05-450 with E_g at 2.8 eV and 2.6 eV, respectively. The new results showed a trend that both ϵ_1 and ϵ_2 increased with the increase of post-treatment temperature.

Table 6.8: Some of the fit parameters for the SC-C05 series where the thicknesses were obtained from the transparent region with a Cauchy layer. The table contains the total thickness as a sum of the two layers, RL thickness (a part of the total thickness) in nm, band gap energy E_g, the placement of the oscillators E_i, $\quad i = 0, 1, 2, 3$, and the mean square error (MSE).

Sample	Total (nm)	RL (nm)	E_g (eV)	E_0 (eV)	E_1 (eV)	E_2 (eV)	E_3 (eV)	MSE
SC-C05-NT	72	0	3.1	5.0	1.3	1.9	-	22
SC-C05-200	66	1.3	3.1	5.0	1.3	2.3	2.4	23
SC-C05-300	68	5.0	3.1	5.0	1.3	2.1	2.4	53
SC-C05-350	67	2.3	3.1	5.3	1.3	2.1	2.4	32
SC-C05-400	65	6.1	2.8	5.3	0.90	1.8	2.4	30
SC-C05-450	61	5.11	2.6	5.2	1.2	-	2.6	34

The measured (solid lines) and model generated (dashed lines) transmittance for sample SC-C05-NT, SC-C05-200 and SC-C05-300 (a), and for sample SC-C05-350, SC-C05-400 and SC-C05-450 (b), for the first run, is shown in Figure 6.30. As seen from the figure, the transmittance measurements have a small dip around 2.1 eV, before the transmittance decreases significantly after E_g. The model generated transmittance have the same shape as the measured, but looks to have a systematically error as it has a higher value before the absorption edge. For the most reduced sample, is is bad agreement between the measured and generated. Also the transmittance decreases slowly with higher post-treatment temperature. (c) and (d) shows the same as (a) and (b), but for the second run. As seen in (c) and (d) is that the generated transmittance did change somewhat to a better match to the measured in the second run. Especially SC-C05-350 and SC-C05-400 are closer to the measured transmittance, but the generated transmittance fails around the band gap for SC-C05-400. For SC-C05-450 the generated actually got a worse match to the measured.

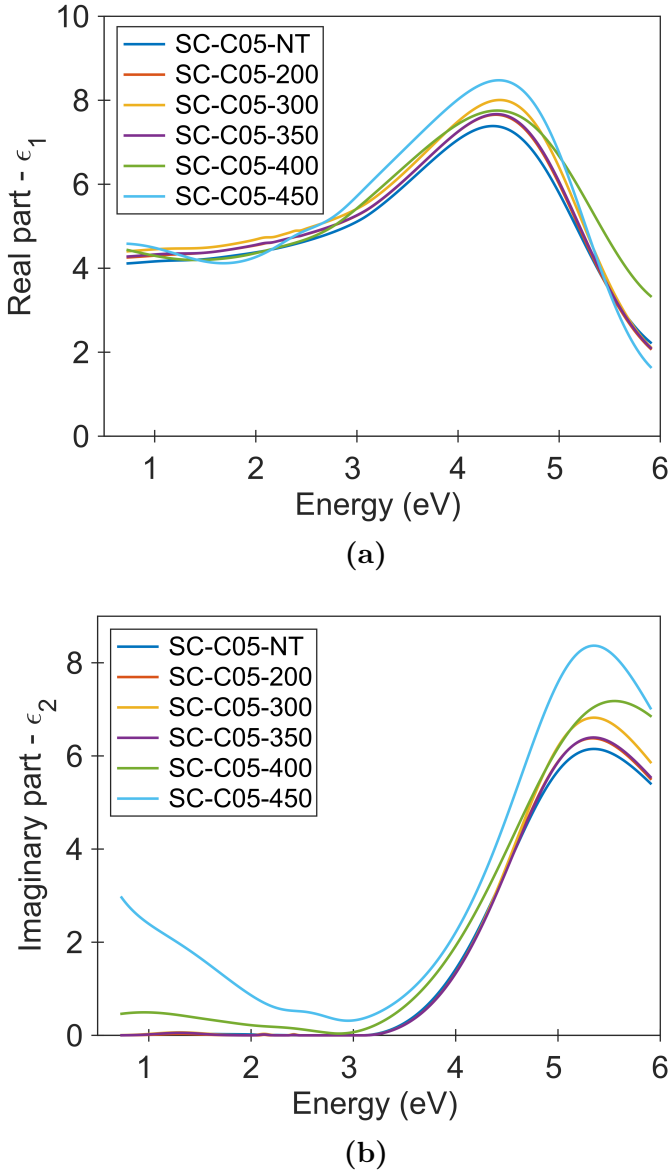

Figure 6.29: (a) The real part of the DF, ϵ_1, for the SC-C05 series for the second run. (b) As (a), but for the imaginary part of the DF, ϵ_2, for the same samples.

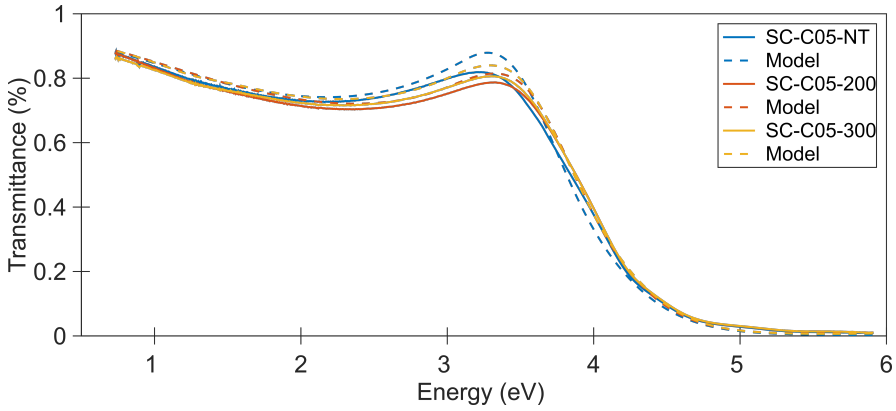

(a)

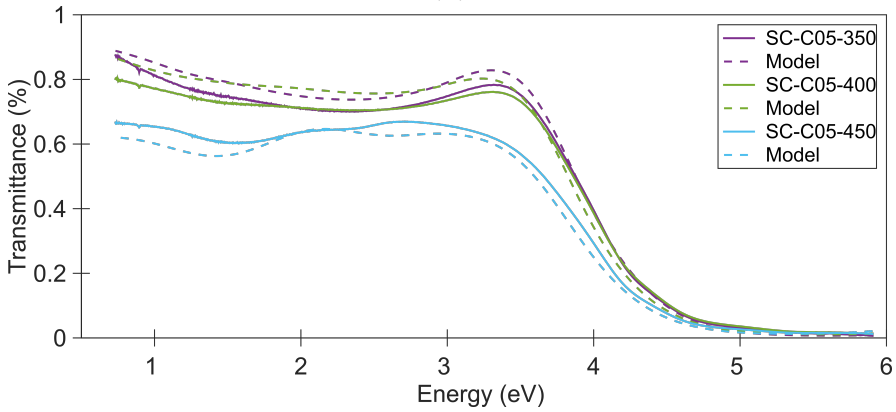

(b)

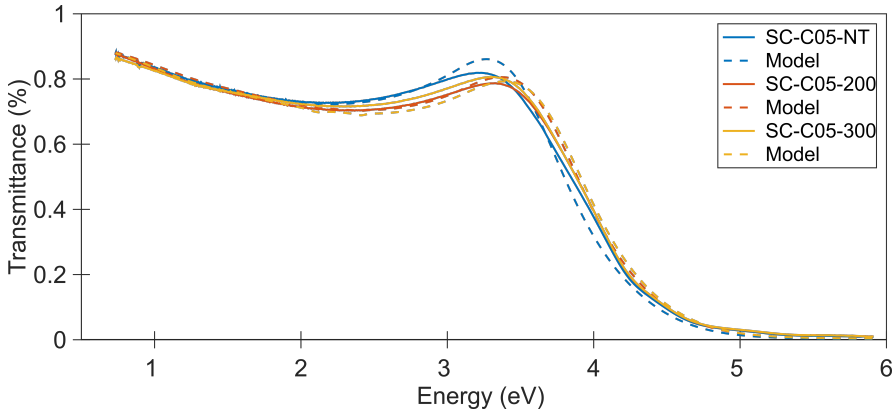

(c)

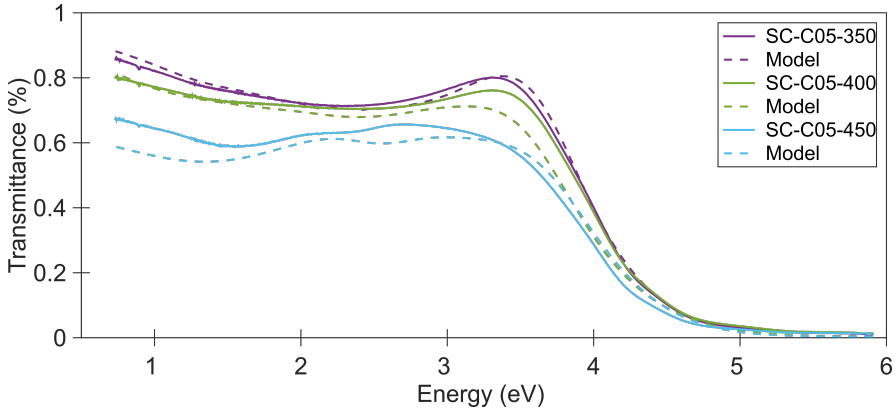

(d)

Figure 6.30: (a) The measured (solid lines) and model generated (dashed lines) transmittance for sample SC-C05-NT, SC-C05-200 and SC-C05-300 for the first run. (b) The measured (solid lines) and model generated (dashed lines) transmittance for sample SC-C05-350, SC-C05-400 and SC-C05-450 for the first run. (c) As (a), but for the second run. (d) As (b), but for second run.

Discussion

The band gap energies E_g, given in Table 6.7 and 6.8, are in good agreement with other observed values which are in the range 2.76-3.70 eV [53, 101, 102, 103]. As for the PLD series, it was concluded the samples contained mainly α-MoO_3 that has a band gap at 3.1 eV [53]. This is in good agreement for E_g from the tables for the least reduced samples. From XRD, it was also assumed that the samples were crystalline, and a typically value for crystalline MoO_3 is 2.9 eV [110]. This is a lower value than obtained in the oscillator layer above, but is not too far away. The results of ϵ_1 and ϵ_2 are also in good agreement with the references from the literature in Figure 6.24, especially with May et. al. [102] and Mohamed et. al [105]. For the two most reduced samples, peaks in ϵ_2 are observed for low energies as in [53, 101, 107].

Using the same argumentation as for the PLD LT-series, it is seen from Figure 6.28 and 6.29 that sample from SC-C05-NT to SC-C05-350 consists of mainly MoO_3, with a few oxygen vacancies as there are only very small contributions from the Gaussians. Sample SC-C05-400 have some sub-band gap contributions mainly from the Gaussian at 0.9 eV. This is close to one of the absorption bands in Mo_4O_{11}. It could indicate that the sample contains Mo_4O_{11}, or one of the other intermediate phases. These results are in good agreement with the observed results from XRD and XPS presented in section 4.3.2. The last sample SC-C05-450 has large contribution from the free carrier oscillator and $E_g = 2.5$ eV. These values indicates MoO_2 is present in the sample, while the large contribution from the Gaussians indicates intermediate phases.

Even though the results from the first run gave the best MSE, the roughness layer was set to zero, i.e. the total thickness in Table 6.7 comes only from the oscillator layer. In section 4.3.2, it was mentioned that the most reduced samples had inhomogeneous and rough surface, so no roughness layer did not seem physical. Therefore, the second run were performed where the roughness layer increased with the increase of post-treatment, i.e. more reduced, as can be confirmed in Table 6.8. More reduced films, obtains a larger ϵ_2 in the results in Figure 6.29, in accordance with other observations [105]. Therefore, the results from the second run are more reliable, even though the MSE value were higher for the series. However, as one can see from the results for sample SC-C05-450, there is no transparent region, and hence using the Cauchy layer for this model is possibly wrong. Most probably, the RL thickness is too thin compared with the R_q and R_a in Table 4.5. Here, R_q and R_a are significantly larger than for the other samples in the series, which is not the case for the RL value in Table 6.8.

Another thing that substantiates the second run gives more reliable results, is from Figure 6.28 and 6.29. Here, the generated transmittance from the model fits better for the second run, especially for SC-C05-300 and SC-C05-350. It is good agreement between the measured values and the generated values from the model for low and high photon energies, but fails around the band gap. SE is good to use for high absorbing and transparent materials, but are not so sensitive for materials with low absorption coefficient α [111]. Therefore, this could be a reason for why the SE model fails around the band gap. An improvement could be to use other transmittance measurements than from SE, which retains good sensitive for low α, to determine the DF around the band gap, while using SE measurements for transparent region and high photon energies where α takes higher values.

6.6.2 SC-C01 Series

Results

The pseudo DF is shown in Figure 6.31 for sample SC-C01-NT (a), SC-C01-400 (b) and SC-C01-450 (c) for the second run to see how well the model match the experimental values. The figure can be interpreted along the same lines as Figure 6.27. As one can see there is good agreement for all samples, especially energies below 4 eV. The shapes for both generated and measured functions are also in good agreement, except for above 5.5 eV. Above this energy, the measured values continues to increase, while the model starts to decrease after a maximum. There are some noise in the measured values at the highest energies since the curves are not smooth.

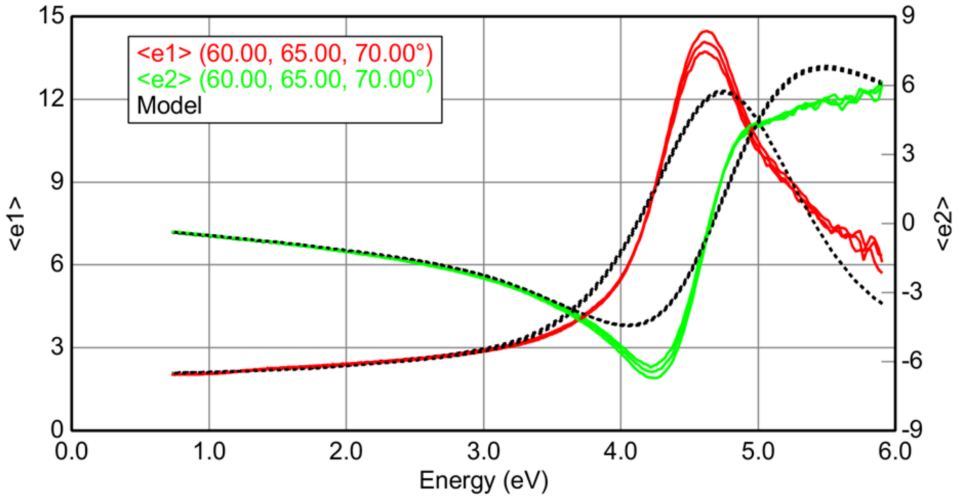

(a)

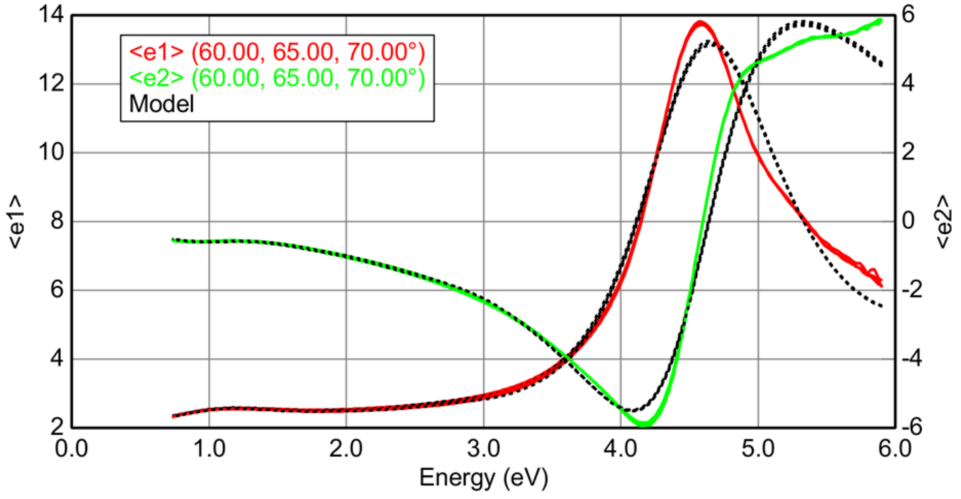

(b)

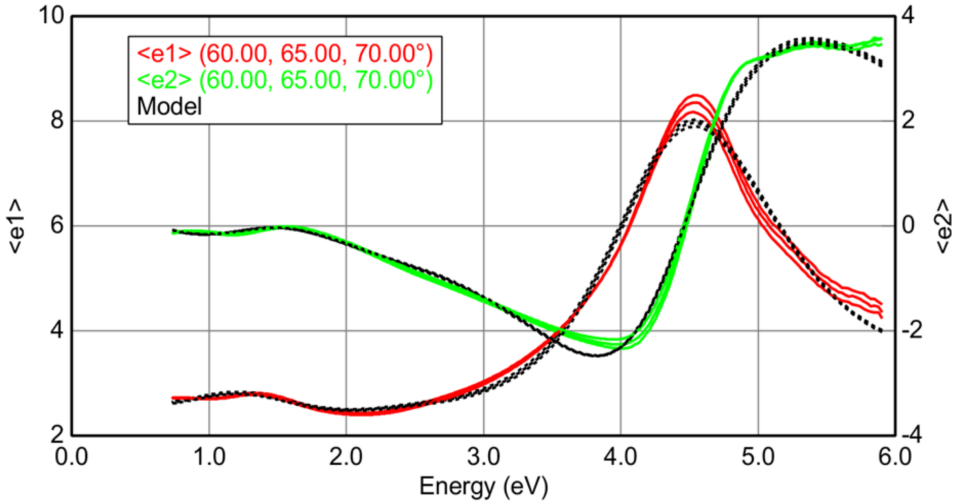

(c)

Figure 6.31: (a) Pseudo-dielectric function for SC-C01-NT for angles of incidence of 60°, 65° and 70° for ϵ_1 (red), ϵ_2 (green) and the generated pseudo DF from the oscillator layer (dashed). (b) As (a), but for SC-C01-400 . (c) As (a), but for SC-C01-450.

The results for ϵ_1 and ϵ_2 for the first run of the oscillator layer are shown in Figure 6.32, where (a) is the real part of the DF ϵ_1. (b) is the imaginary part of the DF ϵ_2. Table 6.9 lists the obtained values for the most important fit parameters from the first run, where the thicknesses were fitted simultaneously with the oscillator parameters for the whole spectral range.

Table 6.9: Some of the fit parameters for the SC-C01 series with sample name, total thickness as a sum of the two layers in the model, RL thickness (a part of the total thickness) in nm, band gap energy E_g, the placement of the oscillators E_i, $\quad i = 0, 1, 2, 3$, and the mean square error (MSE).

Sample	Total (nm)	RL (nm)	E_g (eV)	E_0 (eV)	E_1 (eV)	E_2 (eV)	E_3 (eV)	MSE
SC-C01-NT	16	1.4	3.8	4.6	-	1.7	-	9.1
SC-C01-200	15	0.66	3.8	4.5	-	1.6	-	6.9
SC-C01-300	15	1.9	3.7	4.4	0.89	1.5	-	7.5
SC-C01-350	15	1.5	3.8	4.9	0.76	1.3	-	7.3
SC-C01-400	16	6.4	3.7	4.6	0.91	1.7	-	5.3
SC-C01-450	15	9.1	2.4	4.8	1.3	-	2.6	9.0

As seen from the figure, ϵ_1 behaves in the same manner as for SC-C05 series, except for SC-C01-400 and SC-C01-450, which are much larger. The maximums are still situated around 4.5 eV for the lowest reduced samples. In addition, sample SC-C01-300 and SC-C01-350 slowly decrease for low photon energies before starting to increase towards the maximum. The trend here is that ϵ_1 decreases with post-treatment temperature, except for the two samples which are most reduced. For ϵ_2, only SC-C01-NT and SC-C01-200 have transparent nature for low photon energies, while all samples are transparent between 2.8 eV up to the band gap between 3.7 eV to 3.8 eV. The exception for this behavior is SC-C01-450, which is never transparent for any part of the measured spectral region and has a band gap at 2.4 eV. This sample has large contributions both from the Gaussians and the free carriers below the band gap. Another thing to notice is that for sample SC-C01-300, SC-C01-350 and SC-C01-400 there are significant contributions from the Gaussians, both with and without free carriers contribution. As for ϵ_1, the magnitude decreases with increase in post-treatment temperature. As Table 6.9 shows, the E_g values are around 3.8 eV, except for SC-C01-450 which has $E_g = 2.4$ eV. The placement energy E_0 for the oscillators are approximately equal all samples. The mean square errors (MSE) are in an acceptable range, below 10, for all samples.

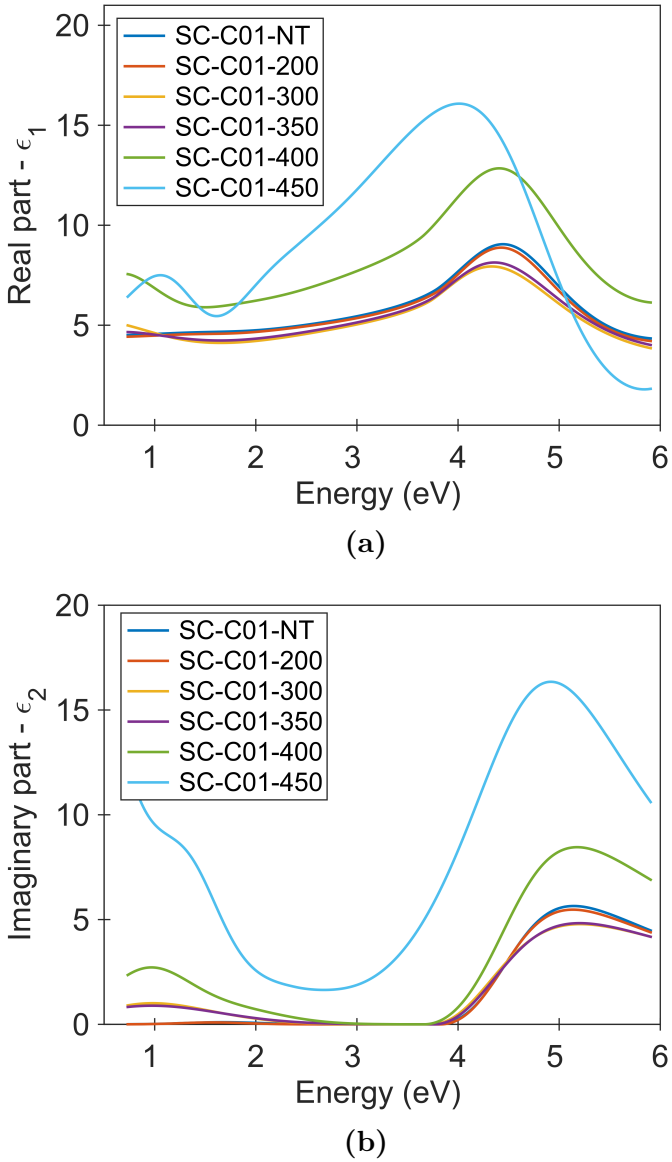

Figure 6.32: (a) The real part of the DF, ϵ_1, for the SC-C01 series, for the first run. (b) As (a), but for the imaginary part of the DF, ϵ_2, for the same samples.

Earlier thickness measurements (from profilometry) gave thicknesses around 10 nm, as mentioned in section 4.3.2. As seen from Table 6.9, all thicknesses found from the model were around 15 nm. In addition, the band gap energies were significantly larger than for the SC-C05 series. Therefore, a second run was also performed for this series with fixed thicknesses from a Cauchy layer in the same range as for the SC-C05 series. The results from this run is shown in Figure 6.33 with the corresponding values for the most important fit parameters in Table 6.10. Both the figure and the table have the same interpretation as earlier. As seen from the table, E_g were fitted to be between 3.0 eV to 3.3 eV for SC-C01-NT until SC-C01-400. SC-C01-450 had a band gap at 2.7 eV. Also here, ϵ_1 and ϵ_2 increased with the increase of the post-treatment temperature. In addition, E_0 starts to decrease from 5.2 eV to 4.6 eV with increase of post-treatment temperature.

Table 6.10: Some of the fit parameters for the SC-C01 series where the thicknesses were obtained from the transparent areas with a Cauchy layer. The table contains the total thickness as a sum of the two layers in the model, RL thickness (a part of the total thickness) in nm, band gap energy E_g, the placement of the oscillators E_i, $\quad i = 0, 1, 2, 3$, and the mean square error (MSE).

Sample	Total (nm)	RL (nm)	E_g (eV)	E_0 (eV)	E_1 (eV)	E_2 (eV)	E_3 (eV)	MSE
SC-C01-NT	15	2.6	3.1	5.2	1.5	2.1	2.4	18
SC-C01-200	13	3.6	3.0	5.2	1.5	2.0	2.5	17
SC-C01-300	9.5	3.1	3.0	4.8	1.2	1.9	2.3	10
SC-C01-350	10	4.5	3.3	4.6	1.3	-	-	8.8
SC-C01-400	9.9	4.9	3.0	4.7	0.99	1.8	2.6	7.2
SC-C01-450	9.5	4.9	2.7	4.6	1.1	-	2.6	11

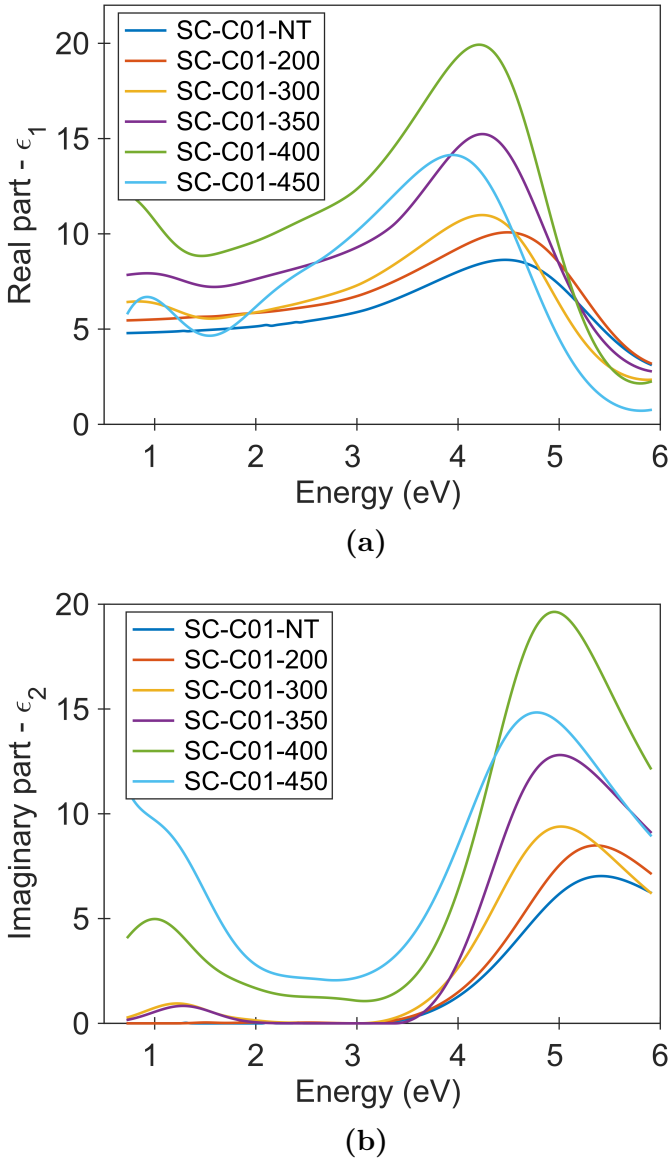

Figure 6.33: (a) The real part of the DF, ϵ_1, for the SC-C01 series, for the second run. (b) As (a), but for the imaginary part of the DF, ϵ_2, for the same samples.

The measured (solid lines) and model generated (dashed lines) transmittance for sample SC-C01-NT, SC-C01-200 and SC-C01-300 (a), and for sample SC-C01-350, SC-C01-400 and SC-C01-450 (b) for the first run is shown in Figure 6.34. The model generated transmittance is in good agreement with the measured, except for sample SC-C01-300 which are much larger than the measured. One thing to note about SC-C01-300 is that the transmittance measurements seems to has lower transmittance than the other samples for this series, also lower than the more reduced samples. This could indicate that the sample differ from the other in the series. As for the SC-C05 series, the generated transmittance fails around the band gap. The measured and generated transmittance for the second run is shown in Figure 6.34 (c) and (d), for SC-C01-NT, SC-C01-200 and SC-C01-300 and for sample SC-C01-350, SC-C01-400 and SC-C01-450, respectively. It seems that the generated transmittance got a slightly worse than for the first run, as the agreement for high and low photon energies got slightly worse. The match for sample SC-C01-300 is still very bad.

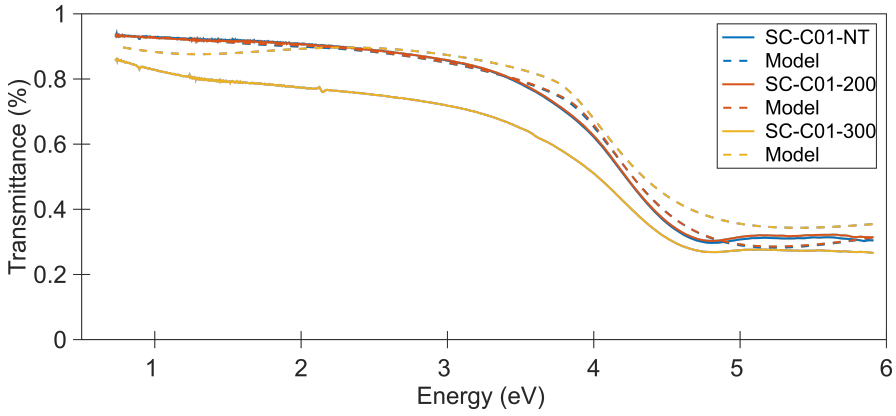

(a)

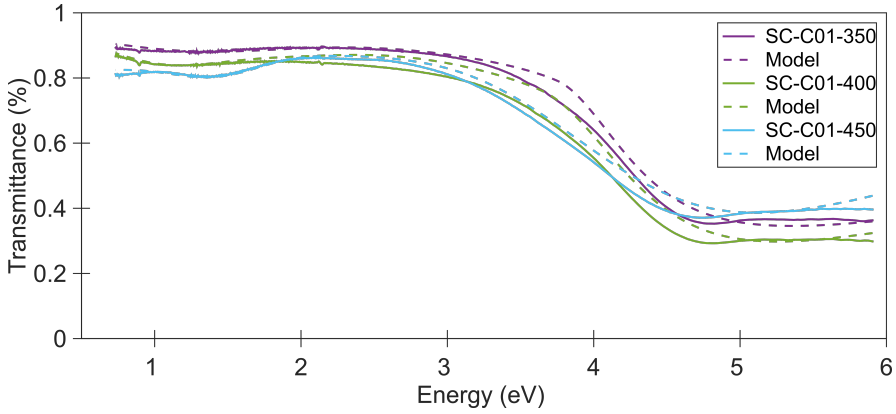

(b)

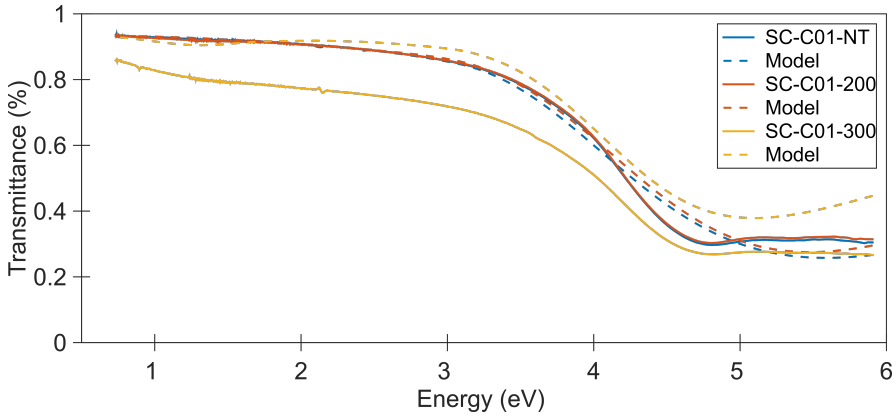

(c)

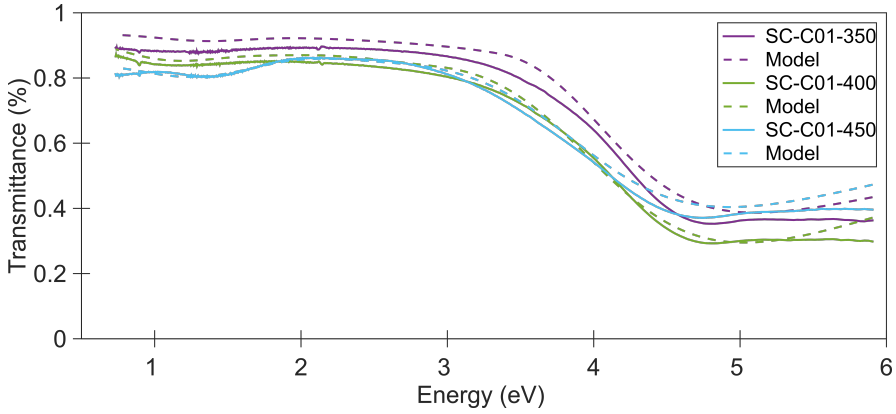

(d)

Figure 6.34: (a) The measured (solid lines) and model generated (dashed lines) transmittance for sample SC-C01-NT, SC-C01-200 and SC-C01-300 for the first run. (b) The measured (solid lines) and model generated (dashed lines) transmittance for sample SC-C01-350, SC-C01-400 and SC-C01-450 for the first run. (c) As (a), but for the second run. (d) As (b), but for second run.

Discussion

Since the first run gave wrong thicknesses and a much larger band gap than expected, was the reason for performing the second run for this series too. From the second run, the thicknesses got more correct around 10 nm as known from the information described in section 4.3.2. The thicknesses decreased with the increase of the post-treatment temperature, as for the SC-C05 series. The roughness layer thickness also increased, which are somewhat in accordance with the observed information from the R_q and R_a in Table 4.5. One would maybe think SC-C01-450 should have larger RL than SC-C01-400, as the samples got highly reduced while heating over 400 °C. From Table 4.5, one can clearly see the R_q and R_a values are much larger for this sample, than the other. As seen in Figure 6.33 (b), SC-C01-400 and SC-C01-450 and did not have any transparent region. Therefore, using the Cauchy layer to determine the thicknesses for these two samples maybe gave wrong thickness and then further lad to wrong parameter values in the fitting process.

The four least reduced samples are in good aggreement with observed values from the literature in Figure 6.24, while SC-C01-400 and SC-C01-450 are higher both for ϵ_1 and ϵ_2. The shape of SC-C01-450 is similar to the form of the reference from Szekeres et. al. [101] as there is no transparent region for the sample.

By using the same argumentation as for the other sample series, sample SC-C01-NT and SC-C01-200 contains mainly MoO_3 as the band gap energies are 3.1 eV and 3.0 eV respectively. None of them have significantly contributions from the Gaussians, only small amplitudes around 0.03-0.05. These could be due to a small amounts of defects in the band gap region. The next three samples indicates absorption at 1.2 eV, and band gap energies at 3.0 eV, 3.3 eV and 3.0 eV for SC-C01-300, SC-C01-350 and SC-C01-400. This could indicate mainly MoO_3 phases with significant contributions from Mo_4O_{11} phases, where SC-C01-400 contains more due to the higher amplitude. As for the SC-C05 series, the sample annealed at 450 °C is most reduced and have large contributions from the free carriers. With a band gap around 2.5 eV it indicates to be MoO_2, and the Gaussians contributions indicates some intermediate oxides. These are in good agreement with the results from XPS, which was found 30.9 % of Mo^{5+} and 7.6% of Mo^{4+}, i.e. from an intermediate phase and MoO_2, respectively, for SC-C01-400. Since the samples were reduced in an hydrogen environment, there could be some hydrogen in the samples which influences the optical properties of the samples. This may lead to more absorption at low energies and therefore leave the Gaussians with higher amplitudes.

One important thing to point out is that the transmittance does not reach zero for high photon energies. It stops around 0.2-0.4, as seen from the transmittance measurements in Figure 6.34. Similar result was obtained in [112] for 10 nm thin films of MoO_3 and other Mo oxides films, where the transmittance for high photon energies was above 0.5. The reason could be the thickness of the samples. They are only 10 nm, and therefore some of the light will not be absorbed even though the energy is larger than E_g. This was not a problem for the SC-C05-series where the transmittance was zero for high photon energies. It could indicate samples of 10 nm in thickness are too thin to absorb or reflect all incident light for high photon energies even though the photon energy is large enough.

6.7 Comparison Between the Sample Series

Figure 6.35 shows the results from the second run for the PLD LT-series (a), SC-C05 series (b), SC-C01 series (c) and a reference to literature where the extinction coefficient is plotted as function of energy [34] in (d). Note the slightly smaller photon energy range for the extinction coefficient. In the latter, stoichiometric MoO_3 films were grown in different gas environments as seen in the legend. Samples in O_2 and N_2 environments had no absorption below the band gap at 3.2 eV determined from a Tauc-plot, while H_2 and forming gas (FG) had clear absorption peaks below the band gap, but still a band gap at 3.2 eV existed [34]. The band gaps for the least reduced samples from SC-series and PLD LT-series, with very little absorption below the band gap, are in good agreement with the stoichiometric MoO_3 films in the reference, i.e. the films grown in O_2 and N_2 environments. The more reduced are in good agreement with the samples grown in H_2 and FG environments. Especially the shape of SC-C01-400 are in good agreement with the sample in FG.

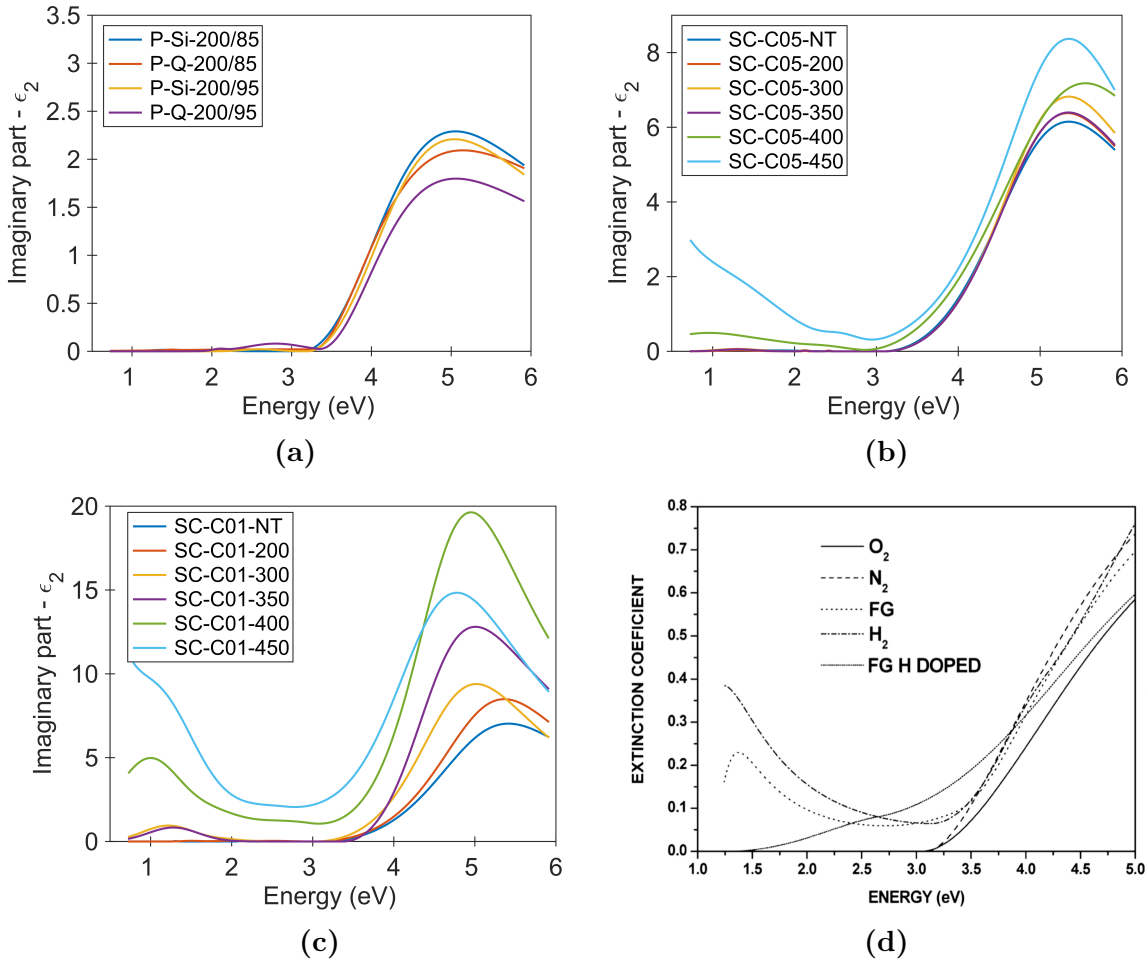

Figure 6.35: (a) ϵ_2 from the second run for the PLD LT-series. (b) As (a), but for SC-C05 series. (c) As (a), but SC-C01 series. (d) Reference from literature taken from Ref. [34].

A clear trend for all series presented above is that the phases of molybdenum oxide goes from MoO_3 to MoO_2 via intermediate phases such as Mo_4O_{11}, depending on the reduction. Samples in the PLD series with much oxygen available, i.e. flows at 70, 85 and 95 sccm, mainly consisted of MoO_3 while the rest had clear contributions from both the Gaussians

and the free carriers. For the SC-series, a similar behavior was observed. For higher post-treatment temperatures in the SC-series, the samples went from MoO_3 phases to MoO_2 via intermediate phases, with good agreement from XPS results presented in section 4.3.2. The same trend are observed in all series from the second run, where ϵ_2 increases as the samples are more reduced. A difference is that ϵ_2 has much larger values for SC-C01 series than SC-C05, while ϵ_2 from the PLD series are lowest. As mentioned in section 4.3.2, the thin samples from the SC-C01 series were more easier to reduce, and hence more defects may have been created. If ϵ_2 decreases for lower annealing temperatures and the band gap increases, it could indicate that the samples is less reduced and the amount of oxygen vacancies decrease in the band gap.

The largest difference between the series from the two different fabrication techniques was the magnitude of ϵ_2 after the band gap. As seen in the figures, maximum value for the least reduced samples was under 2 for the PLD LT-series, while the maximum value was around 6 and 7 for the SC-C05 and SC-C01 series, respectively. One can not distinguish the samples on the band gap energies, E_g, or the placement of the Tauc-Lorentz oscillator, E_0, as they all are in the same energy range. In the results, it was clearly seen that the SC-series were more sensitive to whether the thicknesses were found in the transparent areas or not, compared with the PLD series. One of the reason could be the extra layer with an EMA layer was omitted from the SC-series since they were much thinner than the PLD series. On the other side, it was fewer fit parameters while the thicknesses were held fixed, which could reduce the correlation between the parameters.

A reason why ϵ_2 are larger for SC-series than for the PLD LT-series could be due to that ϵ_1 are smaller for the PLD series compared with the SC-series. While the density of the films decreases and the porosity of the films increases, the refractive index n has been shown to lower, which make the samples more transparent [36, 105]. The porosity depends on the available oxygen during the deposition, especially for the PLD series. From the SEM pictures of the samples from PLD, they looks to have high porosity, especially for the least reduced samples. Hence, the refractive index could be smaller than for the SC-series, which are more dense. This is in good agreement with ϵ_2, as ϵ_2 decreases when there are mainly MoO_3 phases in the samples. Another thing to compare is the placement energy of the Tauc-Lorentz oscillator E_0. As expected, E_0 increase while the reduction of the sample decrease, i.e. E_0 is higher for samples which mainly consist of MoO_3 than for samples with intermediate phases and MoO_2. It is important to note that although the Gaussian at E_2 is present in many samples, the amplitudes are very low, especially for the least reduced samples. In the most reduced samples, there are significantly contributions also from this oscillator.

In the references from the literature for experimentally observed band gaps for MoO_3 (for instance [53, 101, 102, 103]), there are large differences at what energy E_g is situated. These large differences in E_g attributes to method of preparation, deposition conditions, post-deposition annealing, crystallinity, choice of band gap (direct/indirect) and model used to calculate the band gap [113]. As one can see from the band structure of MoO_3, in Figure 4.2, there are a lot of possible transitions and the indirect band gap complicate the transitions. So the band gap may vary, also in the literature depending if they use a direct or indirect band gap in the Tauc-plots. Tauc-plots could indeed been used in this thesis to confirm the band gaps, especially for the SC-series where no such information was available, but Tauc-plots may have large uncertainty.

The free carrier contributions in the final oscillator layer for the most reduced samples are probably a way too large. As seen in Figure 6.19, the free carrier (green dashed line) contributed almost as much as the Tauc-Lorentz oscillator for higher energies for P-Q-200/10, which do not seems physical. The same feature was also observed for sample SC-C05-450, SC-C01-450 and P-Si-200/10, not shown. In Table 6.11 the fit parameters from the free carriers contribution are shown. As one can see the scattering time τ, given in femto seconds (fs), are very small. τ is usually in the range of 10 fs [114], much higher than the obtained value from the fitting process. One of the reason are due to the scattering time τ [114] where $\epsilon_2^{\mathrm{FC}} \propto \tau/E(1+E\tau^2)$ for the free carrier (FC) contribution. I.e. for low τ, ϵ_2^{FC} has large contribution, also for higher energies.

Table 6.11: Overview of the fit parameters from the free carrier contribution ρ (Ω m) and τ in femto seconds (fs).

	P-Si-200/10	P-Q-200/10	SC-C05-450	SC-C01-450
ρ (Ω m)	0.0013	0.0013	0.0036	0.00056
τ (fs)	0.0030	0.027	0.64	1.2

To see how ϵ_2 changed with fixed τ, a new, final, fit was performed for P-Si-200/10, where the results are shown in Figure 6.36 with τ equal 0.1 fs in (a), 1 fs in (b) and 10 fs in (c), with the corresponding fit parameters given in Table 6.12. The light blue line is ϵ_2, while the dashed lines are contributions from the oscillators. As seen from figure, the shape of ϵ_2 changed when τ became higher, while the MSE values were close to each other, i.e. it is high uncertainty in the values for the most reduced samples. Another thing to notice is that while τ increased ρ decreased, i.e. the parameters correlated. Therefore, the free carrier contribution obtained in the most reduced samples in the SC-series and PLD LT-series could be too large in Figure 6.35, and the Gaussians contributions should be larger. As a result, ϵ_2 would be more similar to FG and H_2 in the reference in Figure 6.35 (d). It is important to note that this does not change the discussion about the present phases of molybdenum oxide in the samples, significantly. The only thing is that the models maybe underestimated the contributions from the intermediate phases for the most reduced samples, while the least reduced samples were not affected as the free carriers contributions were zero.

Table 6.12: Overview over important fit parameters for different values of τ, which was fixed during the fitting procedure.

Total (nm)	RL (nm)	EMA (nm)	E_g (eV)	E_1 (eV)	E_2 (eV)	E_3 (eV)	ρ (Ω m)	τ (fs)	MSE
85	2.0	15	2.5	1.3	2.3	-	0.0013	0.10	5.1
77	0.0	18	2.3	1.0	2.0	2.6	0.0011	1.0	5.3
88	1	18	2.3	0.90	1.8	2.6	0.00022	10	6.8

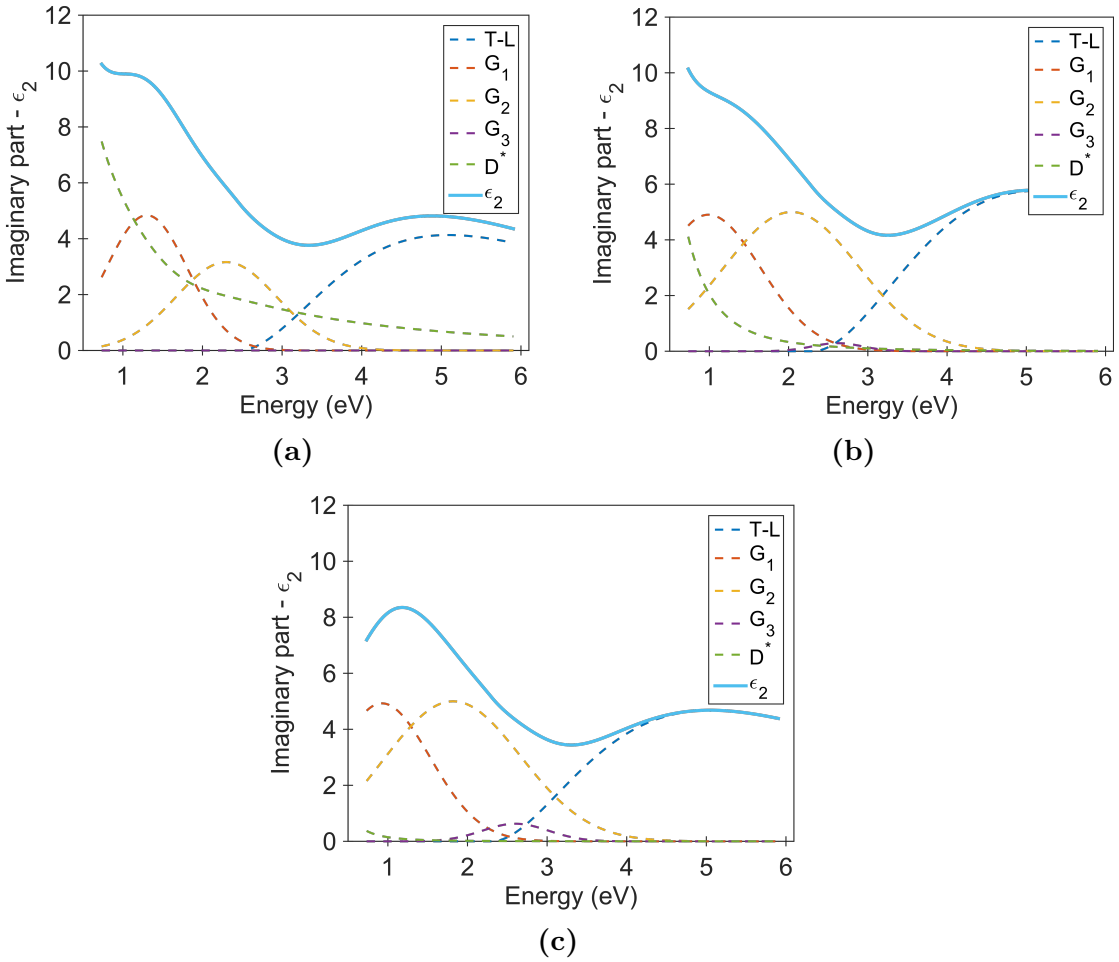

Figure 6.36: (a) ϵ_2 for P-Si-200/10 while the scattering time τ is held fixed at 0.1 femto seconds (fs). The contribution from each oscillator is plotted as dashed lines. (b) As (a), but $\tau = 1.0$ fs. (c) As (a), but $\tau = 10$ fs.

As pointed out in the discussion in section 6.5.2, Lehmann et. al. [109] proposed an empirical rule where the root mean square roughness R_q from AFM measurements could be used to determine the thickness of the roughness layer. This formula is given as $d_r = \frac{R_q}{0.135}$, where 0.135 gave the must successful results for different types of material. If one use this formula with the R_q given in Table 4.5, the roughness layer thickness from the oscillator layer would have bad agreement with d_r for the SC-series. A reason could be the limitation for using EMA, as the morphology cannot be larger than $\lambda/10$. Therefore, the most reduced samples in the SC-series and the PLD HT-series could have too large surface morphology so the layer fails in the modeling of the DF. This could be the reason why the PLD LT-series for highest oxygen flow got the best MSE and a reasonable physical model. As the SEM pictures in Figure 4.7 shows, these films have the least surface roughness, and therefore they have the most reliable results. For the SC-series, also the most reduced samples with no transparent region was attempted to be fitted with thicknesses given from a Cauchy layer. As one can see from the figures they definitely did not have any transparent regions, so these results could be wrong from the second run. There are not so large differences between the two runs for the most reduced samples, as seen in the Figure 6.29 and 6.33.

From the simulation where the thicknesses and percentages of void in the EMA layer were changed (Figure 6.12), it was shown ϵ_2 increased while the percentages of void increased, or the EMA thickness decreased. I.e. for higher thicknesses of the EMA layer, and the oscillator layer decrease, the resulting DF would be higher, since the layer need to absorb more. This could explain why the imaginary part of the DF is much larger for some samples than given in the literature. This is especially the case for the thin samples from the SC-C01 series with 350 °C, 400 °C and 450 °C as post-treatment temperatures. This results in more roughness and a thicker RL, as seen in Table 6.10, and therefore is maybe the cause to increase ϵ_2 of the oscillator layer.

In section 5.4, excitonic behavior was presented and was said could affect the DF. As one can see from the results above, there is no excitonic peak detected around the band gap in the figures. This is probably not surprising as excitonic effects are only seen for low temperature. These peaks broadens with the increase of temperatures. Probably room temperature are too high temperature to see excitonic behavior in data from SE measurements. Another behavior, in section 5.5, was discussed, polarons. The absorption below the band gap may have contributions from polarons since there has been observed polarons absorption around 1.4 eV in MoO_3 [105]. This is close to the E_1 values in the tables from the result parts for each series and could contribute to this peak, and not only be from intermediate phases as Mo_4O_{11}. That means one should see contributions from other than only E_1 to conclude that this is a Mo_4O_{11} phase, or one of the intermediate phases. Polarons have also been observed in WO_3 [115], which have many of the same properties as the molybdenum oxides.

The generated transmittance often failed to match the measured one in the band gap region, but matched the measured transmittance well for low and high energies. An effect which is not taken into account for in the final model presented in section 6.4 is the Urbach tail for absorption just below the band gap. For this effect, one could have used a Cody-Lorentz oscillator and this was done at early stages of the model development in this thesis work. However, during the work it was very difficult to control the tailing. One could have used a Gaussian as May et. al. [102] did in their work, but then it would be difficult to control where it would end up due to the large variation of band gap energy. Omitting to model the Urbach tail could be one reason why the generated transmittance failed around the band gap. As a result, the model could lose some defects just below the band gap in samples mainly consisting of MoO_3. The E_3 value in the listed tables above was set during the fitting to a maximum value of 2.8 eV, so it would not affect the absorption above the band gap significantly, if it was MoO_3. As one can see from the tables, some of the E_3 values were set to the maximum. Therefore, the fitting routine tried to fit the third oscillator to take into account the tailing and tried to get the Gaussian as close as possible to the band gap energy. Another problem with the Gaussian around 2.4 eV is that one of the absorption bands of Mo_4O_{11} (situated at 2.43 eV [72]) coincides with the band gap for MoO_2, i.e. some of the absorption for MoO_2 may be taken into account in the Gaussian, or vice versa.

For all series, the second run gave a higher MSE, but the results fitted better with the observed information from other sources as SEM pictures, AFM measurements, XRD and XPS experiments. Therefore, these are more reliable even though it was possible to obtain lower MSE. It is difficult to model new materials of samples without information about thickness, roughness, porosity and crystallinity phases, for instance. When a good model is obtained, SE is a quick and easy method to determine the optical properties of samples.

Another problem is the huge correlation between the parameters in the fit process. To reduce the correlation between the parameters one can perform a multi sample analysis instead, where some of the parameters are equal for all samples. On the other side, it is difficult to say which parameters should be fitted globally as all fit parameters in the tables varies greatly.

From the results obtained during this thesis, it is difficult to conclude if reduced molybdenum oxides is an suitable IB material. As observed in the results, oxygen flows of 85 and 95 sccm are too high to create sub-band gap states in the PLD series, while 10 sccm is too low to create single bands. For these samples, it was significantly sub-band gap absorption, but they did not exist as single bands. There could possible be an appropriate flow in between these values. For the SC-series it was shown that samples with thick films of molybdenum oxides were difficult to reduce, except for high annealing temperatures where some sub-band gap absorption were observed. The 10 nm films were showed to be easy to reduce, but could be too thin as much of the light is transmitted through. Therefore, the SC method has to be developed further if one wants to fabricate thin MoO_{3-x} films with IB. Therefore, further experimental work is needed to evaluate if MoO_{3-x} can be used as an IB material, or no, in the intermediate band solar cell.

Chapter 7

Conclusion and Suggestions for Further Work

7.1 Conclusion

During this master thesis, non-destructive spectroscopic ellipsometry (SE) measurements were performed on different series of reduced molybdenum oxide, MoO_{3-x}. The series were fabricated before this work started by Katherine Inzani and Mohammadreza Nematollahi, by two deposition methods. The first method was a spin coating (SC) process while the second method used pulsed laser deposition (PLD). The SC-series were reduced in an hydrogen environment with different post-treatment temperatures, while the reduction of MoO_{3-x} from the PLD series were determined by the available oxygen during the deposition. In the beginning, information mainly from the SE measurements, except thickness and surface roughness, were used and many models were created, but had a bad match with the experimental data.

The final model for the SC-series consisted of substrate/oscillator/roughness, while the PLD series had an extra EMA layer between the oscillator and roughness due to the porosity of the sample. The final models were created with information from AFM, XRD, XPS and SEM pictures, and not only SE data. The final oscillator layer consisted of a Tauc-Lorentz oscillator for describing the DF above the band gap, three Gaussians for absorption below the band gap and a Drude oscillator for free carriers contribution at low photon energies.

The final models were used to determine the dielectric function of the samples. With the DF extracted from the models, it was suggested that the least reduced samples for both series mainly consisted of MoO_3 phases with small contributions from the Gaussians, i.e. very small sub-band gap absorption. The most reduced samples had large contributions from free carriers and the Gaussians, i.e. significantly sub-band gap absorption. This indicated the samples consisted of the metallic component MoO_2 and the intermediate phases of molybdenum oxide, most probably Mo_4O_{11}. These results were in good agreement with results obtained from XPS and XRD elsewhere.

It was found that the band gap energy E_g decreased with the reduction of the samples, while ϵ_2 increased with the reduction. This was related to oxygen vacancies and defects in the band gap for the samples. E_g values for MoO_3 were found to be in the range 3.0

eV to 3.3 eV, while for MoO_2 in the range 2.5 eV to 2.6 eV, in good agreement with the literature. ϵ_1 and ϵ_2 values were also in agreement with the literature. ϵ_2 values were smaller for the PLD series than the SC-series due to the porosity of the samples. I.e. the DF depends on the deposition methods and the process temperatures and pressures. For the PLD HT-series, no good results were obtained due to the large and complicated structure of the samples, and the morphology could be too large for the EMA layer to work properly.

This thesis clearly shows that use of SE measurements alone for new materials is difficult without information from other experiments such as SEM, AFM, XPS, XRD and conductivity measurements. An advantage of SE measurements is that it is an easy and quick way to determine the DF of a thin film, but only when a good model is created. The peaks observed below the band gap for the samples could be too wide and small to be an suitable IB material for these deposition methods and parameters. It was concluded that oxygen flows of 85 and 95 sccm were too high to create an IB, while 10 sccm was too low for the PLD series. There could possible be an appropriate flow in between these values. The thinnest samples from SC were easy to reduce, but could be too thin as much of the incident light is not absorbed. The thicker samples were more promising, but were more difficult to reduce. Therefore, it would require more experimental work to conclude whether MoO_{3-x} suits to be an IB material, or not, in an IBSC. How the deposition parameters and method affects the material need more investigation, in addition.

7.2 Suggestions for Further Work

As seen in this thesis, it is very difficult to make a good model when the structure of the samples becomes very complicated, like the PLD HT-series. One of the suggestion for further work is to find a model that better suits for such samples, for instance the models proposed in [108] and [109]. If one want to use some of these models, one need to write own scripts in a programming language such as MATLAB or Python. This will results in more freedom and the number of different and more complicated models can be increased.

As seen from the SEM pictures for the PLD HT-series, one can see large grass like columnar grains. Due to these grains, the optical constants may have different properties in the x, y and z direction. If that is the case, one can use the uniaxial/anisotrpic layer, as in Beydaghyan et. al. [36], instead for the conventional models where the layers are isotropic.

Another improvement of the model is to take into account the Urbach tail with either a Gaussian as in May et. al. [102], or get a better understanding of the Cody-Lorentz oscillator so the model gets physical and do not obtains an unphysical behavior.

Other characterization techniques suggested that different phases of molybdenum oxides were present in different layers of the sample, for instance P-Si-500/70. To create a more realistic model, one could make one oscillator layer for each intermediate phase. For instance, one can develop a layer with a band gap and a free carrier contribution for MoO_2 layers, and another oscillator layer with three Gaussians at the absorption bands for Mo_4O_{11} to place above the MoO_2 layer. Such models will become complicated and the parameters could correlate more for high number of layers.

Phase information Δ is reported to be very sensitive to film thickness [116]. In this thesis work, the properties of how sensitive Δ is for different thicknesses has not been investigated. Therefore, one suggestion for further work is to investigate how Δ change with the thickness, and how it is affected by the complicated surface structure, especially for the PLD HT-series.

During the SE measurements one could also have used tape on the backside of the samples to prevent the backside reflections and reduce the number of fit parameters in the fitting process. Fit parameters can correlate significantly and affect the results. Therefore, fewer fit parameters is preferable.

To confirm the band gap energies, one can use Tauc-plots from transmittance measurements to find a starting value for the fit routine instead of only varying the fit parameter. Another way to improve the work is to use other SE instruments that can measure for a wider spectral range, both in the infrared and the UV.

Bibliography

[1] BP plc, "Statistical review of world energy 2015." http://www.bp.com/en/global/corporate/energy-economics/statistical-review-of-world-energy.html. [Online; accessed 01-May-2016].

[2] SolarPower Europe, "Global market outlook for solar power / 2015-2019." http://www.solarpowereurope.org/insights/global-market-outlook/. [Online; accessed 20-January-2016].

[3] European Photovoltaic Industry Association and Greenpeace International, "Solar photovoltaic electricity empowering the world 2011." http://www.greenpeace.org/international/en/publications/reports/Solar-Generation-6/. [Online; accessed 01-May-2016].

[4] D. M. Chapin, C. S. Fuller, and G. L. Pearson, "A new silicon p-n junction photocell for converting solar radiation into electrical power," *Journal of Applied Physics*, vol. 25, no. 5, pp. 676–677, 1954.

[5] M. Olsen, Copenhagen University, "Solspektret utenfor atmosfaeren, energiballancen." http://www.nbi.ku.dk/spoerg_om_fysik/geofysik_klima/solspektrum_energiballancen/. [Online; accessed 01-May-2016].

[6] J. Twidell and A. D. Weir, *Renewable energy resources*. London: Taylor and Francis, 2nd ed. ed., 2006.

[7] M. A. Green, K. Emery, Y. Hishikawa, W. Warta, and E. D. Dunlop, "Solar cell efficiency tables (version 47)," *Progress in Photovoltaics: Research and Applications*, vol. 24, no. 1, pp. 3–11, 2016.

[8] G. Conibeer, "Third-generation photovoltaics," *Materials Today*, vol. 10, no. 11, pp. 42–50, 2007.

[9] B. R. Hope, "Spectroscopic Ellipsometry Analysis of Cr:ZnS Thin Films for Intermediate Band Solar Cells," Master's thesis, Norwegian University of Science and Technology (NTNU), Trondheim, 2015.

[10] C. G. Granqvist, A. Azens, A. Hjelm, L. Kullman, G. A. Niklasson, D. Rönnow, M. Strømme Mattsson, M. Veszelei, and G. Vaivars, "Recent advances in electrochromics for smart windows applications," *Solar Energy*, vol. 63, no. 4, pp. 199–216, 1998.

[11] N. Miyata and S. Akiyoshi, "Preparation and electrochromic properties of rf sputtered molybdenum oxide films," *Journal of Applied Physics*, vol. 58, no. 4, pp. 1651–1655, 1985.

[12] A. Luque and S. Hegedus, *Handbook of photovoltaic science and engineering*. Chichester: Wiley, 2003.

[13] J. Nelson, *The physics of solar cells*. London: Imperial College Press, 2003.

[14] W. A. Badawy, "A review on solar cells from si-single crystals to porous materials and quantum dots," *Journal of Advanced Research*, vol. 6, no. 2, pp. 123–132, 2015.

[15] W. Shockley and H. J. Queisser, "Detailed balance limit of efficiency of p-n junction solar cells," *Journal of Applied Physics*, vol. 32, no. 3, pp. 510–519, 1961.

[16] O. Vigil-Galan, M. Courel, J. A. Andrade-Arvizu, Y. Sanchez, M. Espindola-Rodriguez, E. Saucedo, D. Seuret-Jimenez, and M. Titsworth, "Route towards low cost-high efficiency second generation solar cells: current status and perspectives," *Journal of Materials Science: Materials in Electronics*, vol. 26, no. 8, pp. 5562–5573, 2015.

[17] A. Martí and G. L. Araújo, "Limiting efficiencies for photovoltaic energy conversion in multigap systems," *Solar Energy Materials and Solar Cells*, vol. 43, no. 2, pp. 203–222, 1996.

[18] M. A. Green, "Third generation photovoltaics: solar cells for 2020 and beyond," *Physica E: Low-dimensional Systems and Nanostructures*, vol. 14, no. 1–2, pp. 65–70, 2002.

[19] S. Kolodinski, J. H. Werner, T. Wittchen, and H. J. Queisser, "Quantum efficiencies exceeding unity due to impact ionization in silicon solar cells," *Applied Physics Letters*, vol. 63, no. 17, pp. 2405–2407, 1993.

[20] A. Luque and A. Martí, "Increasing the efficiency of ideal solar cells by photon induced transitions at intermediate levels," *Physical Review Letters*, vol. 78, no. 26, pp. 5014–5017, 1997.

[21] I. Ramiro, A. Marti, E. Antolin, and A. Luque, "Review of experimental results related to the operation of intermediate band solar cells," *Photovoltaics, IEEE Journal of*, vol. 4, no. 2, pp. 736–748, 2014.

[22] A. Luque and A. Martí, "The intermediate band solar cell: Progress toward the realization of an attractive concept," *Advanced Materials*, vol. 22, no. 2, pp. 160–174, 2010.

[23] C. Tablero, "Electronic and magnetic properties of zns doped with cr," *Physical Review B*, vol. 74, no. 19, p. 195203, 2006. PRB.

[24] A. Marti, L. Cuadra, and A. Luque, "Quantum dot intermediate band solar cell," in *Photovoltaic Specialists Conference, 2000. Conference Record of the Twenty-Eighth IEEE*, pp. 940–943.

[25] S. Lee, O. L. Lazarenkova, P. Von Allmen, F. Oyafuso, and G. Klimeck, "Effect of wetting layers on the strain and electronic structure of inas self-assembled quantum dots," *Physical Review B - Condensed Matter and Materials Physics*, vol. 70, no. 12, pp. 125307–125307, 2004.

[26] H. I. Alexander, M. T. Susanna, H. Sjoerd, V. Oleksandr, Z. David, D. Ratan, L. Larissa, R. R. Lisa, H. C. Graham, F. Armin, W. K. Kyle, J. K. Illan, N. Zhijun,

J. L. André, C. Kang Wei, A. Aram, and H. S. Edward, "Hybrid passivated colloidal quantum dot solids," *Nature Nanotechnology*, vol. 7, no. 9, p. 577, 2012.

[27] M. C. Chia-Hao, R. B. Patrick, B. Vladimir, and G. B. Moungi, "Improved performance and stability in quantum dot solar cells through band alignment engineering," *Nature Materials*, 2014.

[28] J. W. Ager Iii, D. J. Friedman, J. F. Geisz, E. E. Haller, S. R. Kurtz, J. M. Olson, W. Shan, and W. Walukiewicz, "Band anticrossing in gainnas alloys," *Physical Review Letters*, vol. 82, no. 6, 1998. Journal Article.

[29] A. Marti and A. Luque, "Fundamentals of intermediate band solar cells," 2012.

[30] J. Wu, W. Shan, and W. Walukiewicz, "Band anticrossing in highly mismatched iii v semiconductor alloys," *Semiconductor Science and Technology*, vol. 17, no. 8, p. 860, 2002.

[31] K. Alberi, J. Wu, W. Walukiewicz, K. M. Yu, O. D. Dubon, S. P. Watkins, C. X. Wang, X. Liu, Y. Cho, and J. K. Furdyna, "Valence band anticrossing in mismatched iii v semiconductor alloys," *physica status solidi (c)*, vol. 4, no. 5, pp. 1711–1714, 2007.

[32] W. L. Sarney, S. P. Svensson, S. V. Novikov, K. M. Yu, W. Walukiewicz, M. Ting, and C. T. Foxon, "Exploration of the growth parameter space for mbe grown gan1 xsbx highly mismatched alloys," *Journal of Crystal Growth*, vol. 425, pp. 255–257, 2015.

[33] A. Luque, A. Martí, E. Antolín, and C. Tablero, "Intermediate bands versus levels in non-radiative recombination," *Physica B: Condensed Matter*, vol. 382, no. 1–2, pp. 320–327, 2006.

[34] N. Vourdas, G. Papadimitropoulos, A. Douvas, M. Vasilopoulou, N. Boukos, D. Davazoglou, and I. Kostis, "Effect of the oxygen sub-stoichiometry and of hydrogen insertion on the formation of intermediate bands within the gap of disordered molybdenum oxide films," *Journal of Physical Chemistry C*, vol. 117, no. 35, pp. 18013–18020, 2013.

[35] C. Z. Chen, Y. Li, and X. D. Tang, "Evidence of oxygen vacancy and possible intermediate gap state in layered [alpha]-moo.sub.3 single-crystal nanobelts," *Physica B: Physics of Condensed Matter*, vol. 481, p. 192, 2016.

[36] G. Beydaghyan, M. Boudreau, and P. V. Ashrit, "Optical properties and electrochromic response of nanostructured molybdenum trioxide films," *Journal of Materials Research*, vol. 26, no. 1, pp. 55–61, 2011.

[37] A. C. Dillon, A. H. Mahan, R. Deshpande, P. A. Parilla, K. M. Jones, and S. H. Lee, "Metal oxide nano-particles for improved electrochromic and lithium-ion battery technologies," *Thin Solid Films*, vol. 516, no. 5, pp. 794–797, 2008.

[38] C. Julien, A. Khelfa, J. P. Guesdon, and A. Gorenstein, "Lithium intercalation in moo3: A comparison between crystalline and disordered phases," *Applied Physics A*, vol. 59, no. 2, pp. 173–178.

[39] O. Hideaki and S. Yoji, "Characterization of moo 3- x thin films," *Japanese Journal of Applied Physics*, vol. 40, no. 7R, p. 4680, 2001.

[40] J. Scarminio, A. Lourenço, and A. Gorenstein, "Electrochromism and photochromism in amorphous molybdenum oxide films," *Thin Solid Films*, vol. 302, no. 1–2, pp. 66–70, 1997.

[41] T. Ohta, M. Takenaga, N. Akahira, and T. Yamashita, "Thermal changes of optical properties observed in some suboxide thin films," *Journal of Applied Physics*, vol. 53, no. 12, pp. 8497–8500, 1982.

[42] E. Kolawa, C. W. Nieh, F. C. T. So, and M. A. Nicolet, "Microstructure of reactively sputtered oxide diffusion barriers," *Journal of Electronic Materials*, vol. 17, no. 5, pp. 425–432.

[43] M. M. Y. A. Alsaif, M. R. Field, B. J. Murdoch, T. Daeneke, K. Latham, A. F. Chrimes, A. S. Zoolfakar, S. P. Russo, J. Z. Ou, and K. Kalantar-zadeh, "Substoichiometric two-dimensional molybdenum oxide flakes: a plasmonic gas sensing platform," *Nanoscale*, vol. 6, no. 21, pp. 12780–12791, 2014.

[44] S. S. Sunu, E. Prabhu, V. Jayaraman, K. I. Gnanasekar, T. K. Seshagiri, and T. Gnanasekaran, "Electrical conductivity and gas sensing properties of moo31," *Sensors and Actuators B: Chemical*, vol. 101, no. 1–2, pp. 161–174, 2004.

[45] T. Aoki, T. Matsushita, K. Mishiro, A. Suzuki, and M. Okuda, "Optical recording characteristics of molybdenum oxide films prepared by pulsed laser deposition method," *Thin Solid Films*, vol. 517, no. 4, pp. 1482–1486, 2008.

[46] M. Yoosuf Ameen, S. Pradhan, M. Remyth Suresh, and V. S. Reddy, "Moo3 anode buffer layer for efficient and stable small molecular organic solar cells," *Optical Materials*, vol. 39, pp. 134–139, 2015.

[47] W. Zhang, A. Desikan, and S. T. Oyama, "Effect of support in ethanol oxidation on molybdenum oxide," *The Journal of Physical Chemistry*, vol. 99, no. 39, pp. 14468–14476, 1995.

[48] K. Inzani, *Structure-Property Relations of Reduced MoO3*. PhD thesis, NTNU, 2016.

[49] P. Thakur, J. C. Cezar, N. B. Brookes, R. J. Choudhary, R. Prakash, D. M. Phase, K. H. Chae, and R. Kumar, "Direct observation of oxygen induced room temperature ferromagnetism in moo2 thin films by x-ray magnetic circular dichroism characterizations," *Applied Physics Letters*, vol. 94, no. 6, p. 062501, 2009.

[50] A. Taj and P. Ashrit, "Dry lithiation studies of nanostructured sputter deposited molybdenum oxide thin films," *Journal of Materials Science*, vol. 39, no. 10, pp. 3541–3544, 2004.

[51] N. R. Murphy, L. Sun, J. T. Grant, J. G. Jones, and R. Jakubiak, "Molybdenum oxides deposited by modulated pulse power magnetron sputtering: Stoichiometry as a function of process parameters," *Journal of Electronic Materials*, vol. 44, no. 10, pp. 3677–3686, 2015.

[52] R. Sivakumar, V. Vijayan, V. Ganesan, M. Jayachandran, and C. Sanjeeviraja, "Electron beam evaporated molybdenum oxide films: a study of elemental and surface morphological properties," *Smart Materials and Structures*, vol. 14, no. 6, pp. 1204–1209, 2005.

[53] T. Ivanova, A. Szekeres, M. Gartner, D. Gogova, and K. A. Gesheva, "Spectroscopic characterization of cvd-molybdenum oxide films," *Electrochimica Acta*, vol. 46, no. 13, pp. 2215–2219, 2001.

[54] T. S. Sian and G. B. Reddy, "Optical, structural and photoelectron spectroscopic studies on amorphous and crystalline molybdenum oxide thin films," *Solar Energy Materials and Solar Cells*, vol. 82, no. 3, pp. 375–386, 2004.

[55] Q. P. Ding, H. B. Huang, J. H. Duan, J. F. Gong, S. G. Yang, X. N. Zhao, and Y. W. Du, "Molybdenum trioxide nanostructures prepared by thermal oxidization of molybdenum," *Journal of Crystal Growth*, vol. 294, no. 2, pp. 304–308, 2006.

[56] M. Al-Kuhaili, S. Durrani, and I. Bakhtiari, "Pulsed laser deposition of molybdenum oxide thin films," *Materials Science and Processing*, vol. 98, no. 3, pp. 609–615, 2010.

[57] M. Rao, K. Ravindranadh, A. Kasturi, and M. Shekhawat, "Structural stoichiometry and phase transitions of moo3 thin films for solid state microbatteries," *Research Journal of Recent SciencesISSN*, vol. 2, no. 4, pp. 67–73, 2013.

[58] J. Song, X. Ni, D. Zhang, and H. Zheng, "Fabrication and photoluminescence properties of hexagonal moo3 rods," *Solid State Sciences*, vol. 8, no. 10, pp. 1164–1167, 2006.

[59] A. D. Sayede, T. Amriou, M. Pernisek, B. Khelifa, and C. Mathieu, "An ab initio lapw study of the alpha and beta phases of bulk molybdenum trioxide, moo3," *Chem. Phys.*, vol. 316, no. 1-3, pp. 72–82, 2005.

[60] D. O. Scanlon, G. W. Watson, G. W. Payne, G. W. Atkinson, G. W. Egdell, and G. W. Law, "Theoretical and experimental study of the electronic structures of moo 3 and moo 2," *Journal of Physical Chemistry C*, vol. 114, no. 10, pp. 4636–4645, 2010.

[61] Y. Liang, Z. Yi, S. Yang, L. Zhou, J. Sun, and Y. Zhou, "Hydrothermal synthesis and lithium-intercalation properties of moo2 nano-particles with different morphologies," *Solid State Ionics*, vol. 177, no. 5–6, pp. 501–505, 2006.

[62] Y.-R. Ma, C.-C. Tsai, S. F. Lee, K.-W. Cheng, Y. Liou, and Y. D. Yao, "Magnetic properties of large-area one-dimensional wo2 and moo2 nanorods," *Journal of Magnetism and Magnetic Materials*, vol. 304, no. 1, pp. e13–e15, 2006.

[63] X. Liu, Y. He, S. Wang, and Q. Zhang, "Preparation of moo2 sub-micro scale sheets and their optical properties," *Journal of Alloys and Compounds*, vol. 509, Supplement 1, pp. S408–S411, 2011.

[64] O. G. Marin Flores and S. Ha, "Activity and stability studies of moo2 catalyst for the partial oxidation of gasoline," *Applied Catalysis A: General*, vol. 352, no. 1–2, pp. 124–132, 2009.

[65] O. Marin-Flores, L. Scudiero, and S. Ha, "X-ray diffraction and photoelectron spectroscopy studies of moo2 as catalyst for the partial oxidation of isooctane," *Surface Science*, vol. 603, no. 15, pp. 2327–2332, 2009.

[66] R. Naouel, F. Touati, and N. Gharbi, "Low temperature crystallization of a stable phase of microspherical moo2," *Solid State Sciences*, vol. 12, no. 7, pp. 1098–1102, 2010.

[67] J. Zhou, N. S. Xu, S. Z. Deng, J. Chen, and J. C. She, "Synthesis of large-scaled moo2 nanowire arrays," *Chemical Physics Letters*, vol. 382, no. 3–4, pp. 443–446, 2003.

[68] J. Sloczynski, "Kinetics and mechanism of molybdenum (vi) oxide reduction," *Journal of Solid State Chemistry*, vol. 118, no. 1, pp. 84–92, 1995.

[69] V. Eyert, R. Horny, K. Hock, and S. Horn, "Embedded peierls instability and the electronic structure of moo2," *J. Phys.-Condes. Matter*, vol. 12, no. 23, pp. 4923–4946, 2000.

[70] N. Dukstiene and D. Sinkeviciute, "Photoelectrochemical properties of moo2 thin films," *Journal of Solid State Electrochemistry*, vol. 17, no. 4, pp. 1175–1184, 2013.

[71] R. S. Patil, M. D. Uplane, and P. S. Patil, "Structural and optical properties of electrodeposited molybdenum oxide thin films," *Applied Surface Science*, vol. 252, no. 23, pp. 8050–8056, 2006.

[72] V. R. Porter, W. B. White, and R. Roy, "Optical spectra of the intermediate oxides of titanium, vanadium, molybdenum, and tungsten," *Journal of Solid State Chemistry*, vol. 4, no. 2, pp. 250–254, 1972.

[73] M. Anwar and C. Hogarth, "The correlation of various properties of thin films of moo 3 and of the mixed oxide systems moo 3 -in 2 o 3 and moo 3 -sio," *Journal of Materials Science*, vol. 25, no. 11, pp. 4918–4928, 1990.

[74] A. Arfaoui, B. Ouni, S. Touihri, A. Mhamdi, A. Labidi, and T. Manoubi, "Effect of annealing in a various oxygen atmosphere on structural, optical, electrical and gas sensing properties of moxoy thin films," *Optical Materials*, vol. 45, pp. 109–120, 2015.

[75] D. Bäuerle, *Laser Processing and Chemistry*. Berlin, Heidelberg: Springer Berlin Heidelberg: Berlin, Heidelberg, 2011.

[76] D. Bauerle, R. Rossler, J. Pedarnig, S. Yun, R. Dinu, and N. Arnold, "Pulsed laser deposition," *Applied Physics A*, vol. 69, no. 1, pp. S45–S48.

[77] R. W. Eason, R. Eason, and D. B. Chrisey, *Pulsed laser deposition of thin films : applications-led growth of functional materials*. Hoboken, N.J: Wiley-Interscience, [2nd ed.]. ed., 2007.

[78] The Brownfields and Land Revitalization Technology Support Center, "Glossary." `https://brownfieldstsc.org/index.cfm`. [Online; accessed 04-June-2016].

[79] V. Senez, V. Thomy, and R. Dufour, *Nanotechnologies for Synthetic Super Non-wetting Surfaces*. Nanotechnologies for Synthetic Super Non Wetting Surfaces, Hoboken: Wiley, 2014.

[80] American pink. `http://america.pink/spin-coating_4124958.html`. [Online; accessed 25-April-2016].

[81] I. J. A. Woollam Co., "Guide to using wvase32," 2008.

[82] H. Fujiwara, "Spectroscopic ellipsometry; principles and applications," *Scitech Book News*, vol. 31, no. 2, 2007.

[83] H. Tompkins, E. A. Irene, and H. Tompkins, *Handbook of Ellipsometry*. Burlington: Elsevier Science, 2005.

[84] L. M. S. Aas, *Mueller Matrix Imaging and Spectroscopy*. PhD thesis, NTNU, 2013.

[85] I. J. A. Woollam Co., "Rc2 spectroscopic ellipsometer - hardware manual (vertical sample moint goniometer)," October 2011.

[86] J.A. Woollam. `https://www.jawoollam.com/products/rc2-ellipsometer`. [Online; accessed 25-April-2016].

[87] I. J. A. Woollam Co., "Completeease data analysis manual," 2011.

[88] P. Y. Yu and M. Cardona, *Fundamentals of Semiconductors: Physics and Materials Properties*. Physics and Materials Properties, Berlin, Heidelberg: Springer Berlin Heidelberg, Berlin, Heidelberg, 2010.

[89] G. E. Jellison and F. A. Modine, "Parameterization of the optical functions of amorphous materials in the interband region," *Applied Physics Letters*, vol. 69, no. 3, pp. 371–373, 1996.

[90] A. S. Ferlauto, G. M. Ferreira, J. M. Pearce, C. R. Wronski, R. W. Collins, X. Deng, and G. Ganguly, "Analytical model for the optical functions of amorphous semiconductors from the near-infrared to ultraviolet: Applications in thin film photovoltaics," *Journal of Applied Physics*, vol. 92, no. 5, pp. 2424–2436, 2002.

[91] F. Urbach, "The long-wavelength edge of photographic sensitivity and of the electronic absorption of solids," *Physical Review*, vol. 92, no. 5, pp. 1324–1324, 1953. PR.

[92] C. Q. Hu, F. F. Meng, M. Wen, Z. Q. Gu, J. Y. Wang, X. F. Fan, and W. T. Zheng, "Relationship between dielectric coefficient and urbach tail width of hydrogenated amorphous germanium carbon alloy films," *Applied Physics Letters*, vol. 101, p. 042109, 2012.

[93] S. John, C. Soukoulis, M. H. Cohen, and E. N. Economou, "Theory of electron band tails and the urbach optical-absorption edge," *Physical Review Letters*, vol. 57, no. 14, pp. 1777–1780, 1986. PRL.

[94] D. DimovaMalinovska, H. Nichev, and O. Angelov, "Correlation between the stress in zno thin films and the urbach band tail width," *physica status solidi (c)*, vol. 5, no. 10, pp. 3353–3357, 2008.

[95] W. Y. Liang, "Excitons," *Physics Education*, vol. 5, no. 4, p. 226, 1970.

[96] S. W. Koch, M. Kira, G. Khitrova, and H. M. Gibbs, "Semiconductor excitons in new light," *Nature Materials*, vol. 5, no. 7, p. 523, 2006.

[97] I. G. Austin and N. F. Mott, "Polarons in crystalline and non-crystalline materials," *Advances in Physics*, vol. 50, no. 7, pp. 757–812, 2001.

[98] L. Landau *Physikalische zeitschrift der Sowjetunion*, vol. 3, p. 644, 1933.

[99] A. S. Alexandrov, *Polarons in Advanced Materials*, vol. v.103 of *Materials Science, Volume 103*. Dordrecht: Springer, 2008.

[100] J. Ranninger, "Introduction to polaron physics: Basic concepts and models," 2006.

[101] A. Szekeres, T. Ivanova, and K. Gesheva, "Spectroscopic ellipsometry study of cvd molybdenum oxide films: effect of temperature," *Journal of Solid State Electrochemistry*, vol. 7, no. 1, pp. 17–20, 2002.

[102] R. A. May, L. Kondrachova, B. P. Hahn, and K. J. Stevenson, "Optical constants of electrodeposited mixed molybdenum-tungsten oxide films determined by variable-angle spectroscopic ellipsometry," *Journal of Physical Chemistry C*, vol. 111, no. 49, pp. 18351–18357, 2007.

[103] M. Yahaya, M. M. Salleh, and I. Talib, "Optical properties of moo3 thin films for electrochromic windows," *Solid State Ion.*, vol. 115, pp. 421–423, 1998.

[104] A. Boukhachem, O. Kamoun, C. Mrabet, C. Mannai, N. Zouaghi, A. Yumak, K. Boubaker, and M. Amlouk, "Structural, optical, vibrational and photoluminescence studies of sn-doped moo3 sprayed thin films," *Materials Research Bulletin*, vol. 72, pp. 252–263, 2015.

[105] S. H. Mohamed, O. Kappertz, J. M. Ngaruiya, T. P. Leervad Pedersen, R. Drese, and M. Wuttig, "Correlation between structure, stress and optical properties in direct current sputtered molybdenum oxide films," *Thin Solid Films*, vol. 429, no. 1, pp. 135–143, 2003.

[106] B. Tummers, "Datathief iii. 2006." `http://datathief.org/`. [Online; accessed 22-April-2016].

[107] F. Hamelmann, A. Brechling, A. Aschentrup, U. Heinzmann, P. Jutzi, J. Sandrock, U. Siemeling, T. Ivanova, A. Szekeres, and K. Gesheva, "Thin molybdenum oxide films produced by molybdenum pentacarbonyl 1-methylbutylisonitrile with plasma-assisted chemical vapor deposition," *Thin Solid Films*, vol. 446, no. 2, pp. 167–171, 2004.

[108] M. Akagawa and H. Fujiwara, "High-precision characterization of textured a-si:h/sno2:f structures by spectroscopic ellipsometry," *Journal of Applied Physics*, vol. 110, no. 7, p. 073518, 2011.

[109] D. Lehmann, F. Seidel, and D. R. T. Zahn, "Thin films with high surface roughness: thickness and dielectric function analysis using spectroscopic ellipsometry," *SpringerPlus*, vol. 3, 2014.

[110] K. Gesheva, A. Cziraki, T. Ivanova, and A. Szekeres, "Structure and composition of thermally annealed mo- and w-based cvd metal oxide thin films," *Thin Solid Films*, vol. 492, no. 1, pp. 322–326, 2005.

[111] K. Ghimire, H. F. Haneef, R. W. Collins, and N. J. Podraza, "Optical properties of single crystal gd 3 ga 5 o 12 from the infrared to ultraviolet," *physica status solidi b*, vol. 252, no. 10, pp. 2191–2198, 2015.

[112] M. Vasilopoulou, A. M. Douvas, D. G. Georgiadou, L. C. Palilis, S. Kennou, L. Sygellou, A. Soultati, I. Kostis, G. Papadimitropoulos, D. Davazoglou, and P. Argitis, "The influence of hydrogenation and oxygen vacancies on molybdenum oxides work function and gap states for application in organic optoelectronics," *Journal of the American Chemical Society*, vol. 134, no. 39, p. 16178, 2012.

[113] M. F. Al-Kuhaili, S. M. A. Durrani, I. A. Bakhtiari, and A. M. Al-Shukri, "Optical constants and thermocoloration of pulsed laser deposited molybdenum oxide thin films," *Optics Communications*, vol. 283, no. 14, pp. 2857–2862, 2010.

[114] M. Fox, *Oxford Master Series in Physics, Volume 3 : Optical Properties of Solids (2nd Edition)*. Oxford: Oxford, GBR: OUP Oxford, 2010.

[115] M. B. Johansson, G. Baldissera, I. Valyukh, C. Persson, H. Arwin, G. A. Niklasson, and L. Österlund, "Electronic and optical properties of nanocrystalline wo 3 thin films studied by optical spectroscopy and density functional calculations," *Journal of Physics: Condensed Matter*, vol. 25, no. 20, p. 205502, 2013.

[116] J.A. Woollam Co., "Thin film thickness." `https://www.jawoollam.com/resources/ellipsometry-tutorial/thin-film-thickness`. [Online; accessed 13-June-2016].